Controlling Indentation-induced Phases of Silicon

By

Sherman Wong

Thesis

A Thesis Submitted for the
Degree of Doctor of Philosophy
of The Australian National University

Certificate

This thesis, except where explicitly referenced in the text, solely contains original research done by the author.

Sherman Wong

Acknowledgments

First and foremost, I would like to thank my supervisor A. Prof. Jodie Bradby for her guidance and support throughout the process of my PhD. I would also like to thank my supervisory panel, Prof. Jim Williams and Dr. Bianca Haberl for their help and advice though my research.

I acknowledge Dr Malcolm Guthrie for his assistance in XRD data collection and analysis. Without his expertise, the XRD results would not have been possible. I acknowledge Wenjie Yang for her assistance in spectrophotometery and for helping me analyse the results even when they made no sense to me. I acknowledge Dr. Brett Johnson for his assistance in *in situ* Raman measurements. Without his prompting, I would not have realised how much more there is to learn about annealing bc8/r8. I acknowledge Prof. Andres Mujica for providing the theoretical calculations for this thesis. I wish I could have included more of his calculations, but unfortunately so many of his interesting predictions fell outside the scope of this work.

I acknowledge the Advanced Photon Source at Argonne National Labs. In particular I would like to thank the staff of HP-CAT that have always been so helpful and always made us feel so welcome. I acknowledge the ACT node of the Australian National Fabrication Facility for access to the FIB system. I acknowledge the Centre for Advanced Microscopy for access to the TEM. I would like to thank Felipe Kremer for sharing his expertise in electron microscopy.

I acknowledge the Australian Research Council and the Discovery Project scheme which provided the funding for this work.

I would like to thank Tom, Larissa, and Lachlan for reading though my thesis drafts. I would like to thank the rest of my colleagues at EME both past and present. You all have made my time here an enjoyable one.

I would like to thank my family, especially my wife Queenie who has been a huge support during this period in my life.

Finally, I would like to thank God, through whom all this is possible.

Controlling Indentation-induced Phases of Silicon

Sherman Wong

Department of Electronic Materials Engineering
The Australian National University
Canberra,ACT
2017

ABSTRACT

Silicon (Si) is the backbone of the semiconductor industry. The widespread use of Si is largely due to the useful electrical and optical properties of the material in its standard, diamond cubic (dc) crystal structure. However, in recent years, there has been an increasing interest in the properties of Si with different crystal structures (phases). In particular, the metastable phases formed through pressure application have been the topic of much study due to their promising properties. For example, the body-centred cubic phase (bc8-Si) has been reported to have an ultra-narrow band-gap whereas the rhombohedral phase (r8-Si) has been predicted to have an improved absorption coefficient across the solar spectrum. A mixture of these two exotic phases can be formed directly from a standard dc-Si semiconductor wafer using the application of pressure through point loading via indentation. This thesis addresses several challenges regarding the formation, stability, and properties of this bc8/r8 structure.

The process involving the nucleation of the bc8/r8 phase via indentation was investigated in detail. Specifically, the interplay between the nucleation of the bc8/r8 phase with other plastic deformation processes within the surrounding crystalline lattice (labelled collectively as "crystalline defects" within this work) that occur is studied. It was shown that both phase transformation and the formation of crystalline defects are nucleation limited. Thus, holding a volume of Si at high pressure for a duration increases the likelyhood that th material will plastically deform. It is also shown that these two forms of plastic deformation act as competing mechanisms, with the mode of incipient plasticity playing a dominant role in the shape and volume of the final phase transformed region. Indentations in which phase trans-

formation occur before crystalline defects occur result in larger, more uniform regions of phase transformed material.

The phase fraction of r8-Si within the mixed structure is determined using Rietveld analysis of x-ray diffraction (XRD) data. The mixed structure was found to be predominantly r8-Si, with this phase comprising 60 to 80 percent of the structure. These results also show that there is residual stress within the bc8/r8 structure that causes an elongation of the unit cell along the axis of indentation. The optical absorption from a thin film of the bc8/r8 structure is measured using spectrophotometry. There is a clear increase in absorption due to the presence of the bc8/r8 structure. As the optical properties of bc8-Si are known from the literature, an estimate for the r8-Si absorption coefficient is calculated from this absorption increase.

The stability of the bc8/r8 mixed structure under thermal annealing is explored. A transformation from r8-Si to a novel phase with an, as yet, unknown crystal structure (Si-XIII) is reported after annealing to 100 degrees C. Si-XIII further transforms to a hexagonal structure (hd-Si) at 240 degrees C, and then transforms back to dc-Si (in a nanocrystalline form) at 750 degrees C. A transformation from bc8-Si to hd-Si is also proposed at a temperature below 240 degrees C. Therefore, there is a temperature range where hd-Si is both stable and the sole crystalline phase present within the transformed region. Laser-induced annealing results were also presented, and a similar transformation pathway was reported.

Thus, the formation, stability, and technologically interesting properties of the bc8/r8 structure is presented. This forms a framework for future studies into the scalability of this structure to technologically relevant sizes.

Table of Contents

List of Figures

List of Tables

Chapter 1

Introduction

A large part of our modern society is built on the foundation of the semiconductor industry. This industry is largely built on the foundation of one material, silicon (Si) [1]. Due to the abundance, affordability, and electronic properties of Si, it forms the basis for many modern day semiconductor devices such as transistors [2, 3] and solar cells [4–6]. To continuously advance technological capabilities, there is a constant demand for new semiconducting materials with improved performance. Despite the ubiquitous nature of Si in this industry, its indirect band-gap generates limitations, such as a significantly reduced ability to produce or process light [7–9]. Attempts to overcome this limitation have been made by using other semiconducting materials with a direct band gap, for example using III-V semiconductors such as GaAs, InP, GaN etc. [10–14]. However, none of these other materials can match Si's abundance, affordability, and non-toxicity. Nor do these III-V materials take full advantage of the multi-billion dollar industry that has been built around the fabrication of Si [15, 16].

One approach to increasing the range of Si-based applications that is currently attracting significant interest is the use of different crystal structures of Si [17]. That is, using elemental Si with crystalline phases that vary from the standard diamond cubic structure (dc-Si). Such phases maintain many of the advantages of Si while potentially possessing a range of different properties that are useful for a variety of specialised applications. A recent review by Haberl *et al.* highlights the fact that thousands of energetically plausible crystal structures have been theoretically predicted [18]. Although only a subset of these phases are thought to be physically feasible and stable, within that subset some may be formed using currently available techniques, be metastable in ambient conditions, and also have promising properties [19–23]. Thus, there is considerable interest in moving beyond the standard structure of Si by forming these predicted phases and characterising their properties.

Many Si phases have been formed under high pressure using diamond anvil cells (DACs) [24–28]. That is, the sample is held between two diamonds with opposing flat surfaces (anvils) that are pressed together to apply pressure [29]. Through pressure application, several exotic phases of Si have been formed. Two such phases of particular interest are shown to be metastable after complete pressure unloading (bc8-Si and r8-Si) [30], with bc8-Si being the predominant phase [31]. Another exotic phase of interest (hd-Si) can also be formed by annealing the metastable bc8-Si phase [32]. However, no more new phases have been reported in DAC

experiments since 1994. Thus, different techniques have been explored by researchers. Three such techniques that have been of particular interest are the use of Si-rich chemical precursors [33]; using fs-lasers to produce subsurface explosions in Si [34]; and uniaxial point loading via indentation [35–37]. The final synthesis pathway, indentation, is the focus of this thesis.

Indentation has the following advantages as a tool for the formation of exotic phases of Si via applied pressure. Firstly, whilst bc8-Si is the predominant metastable crystalline structure recoverable after experiencing high pressure in a DAC, indentation-induced phase transformation results in a substantial amount of r8-Si being found to be present alongside bc8-Si [38–40]. This increased presence of the phase, r8-Si, has been attributed to the residual stress that is present in indents [41, 42]. The presence of significant amounts of both bc8-Si and r8-Si has been confirmed using a number of measurement techniques, although the exact ratio of the two phases remains unknown [38, 39, 43]. Annealing this mixed structure forms an additional phase, called Si-XIII, that is yet unreported to form using DACs. The crystal structure of Si-XIII remains unknown [41, 44, 45]. A further difference in the phases that can be formed via indentation occurs with fast pressure removal. Upon fast removal, an amorphous Si (a-Si) structure is commonly reported [46]. This indentation-induced a-Si is structurally unique relative to a-Si formed via other methods (e.g. ion implantation) [47, 48]. Thus, there are three known metastable structures (r8-Si, Si-XIII, indentation-induced a-Si) that are readily recovered after indentation that have not been reported in significant amounts in DAC experiments.

A further advantage of indentation is the unique pressure distribution within the sample. For indentation, the pressure distribution is primarily dependent on the shape and size of the indenter tip. This plays an important role in determining the nature of the plastic deformation that samples undergo [39, 49–51]. A significant amount of shear stress is also introduced by the tip geometry which can act as a catalyst to lower the critical pressure for transformation [52–54]. Further, the recovered phases after indentation are often observed alongside significant damage to the surrounding material [39, 46, 50]. Although, this is not always the case as we have shown [55]. It is currently unknown how the presence of this damage is connected with the transformation process.

There is also the possibility to tailor the shape and volume of the exotic phases formed via indentation. Ruffell *et al.* showed that overlapping indentation can be used to effectively write lines of these phases onto a Si surface [56]. That is, industrially relevant volumes of these exotic phases can be readily "written" onto existing standard Si samples via lines of overlapping indents. Ruffell *et al.* further suggested that, with a greater understanding of the pressure distribution required for forming these phases, larger indenter stamps with customised shapes could be produced to create technologically applicable regions of these metastable phases.

It is important to highlight the fact that significant zones of the technologically interesting

r8-Si can be recovered after indentation. However, from a practical sense there are still unanswered questions and barriers regarding this metastable phase that must be addressed before such a process could be integrated into a commercial device. Such issues are the following: What fraction of the recovered bc8/r8 mixed structure is r8-Si? What are the optical and electrical properties of this mixed structure? How is the phase transformation process impacted by deformation that causes damage in the surrounding material? How can the phase transformation zone be maximised and the surrounding damage minimised? What is the thermal stability of these metastable phases? More broadly, how can our understanding of such processes in Si help inform our understanding of its sister materials Ge and C?

This thesis aims to address these questions. Further, it aims to better understand the response of this important group IV semiconductor under indentation-applied pressure in the hope that a more complete framework can be produced that can be used to support the production of similar phases in other group IV materials (i.e. Ge, C).

1.1 Thesis structure

- Chapter 2 - Outlines the literature regarding the exotic phases of Si, with a focus on those formed via pressure application.
- Chapter 3 - Gives a description of the experimental techniques used in this thesis to form and characterise the exotic phases of Si.
- Chapter 4 - Presents two important properties of the bc8/r8 structure recovered from indentation. These are the phase ratio and the optical response of this mixed structure. The structure is found to be predominantly r8-Si, and the absorption coefficient of the structure is shown to be higher than that of dc-Si.
- Chapter 5 - Presents the use of a hold duration at maximum indentation load to better explore the time dependence of both the dc-Si to β-Sn transformation and the alternative deformation by defect propagation. Phase transformation is shown to be promoted by longer hold durations and the shape of the transformed region is found to be dependent on the pressure distribution.
- Chapter 6 - Presents an investigation of the transformation pathways the bc8/r8 mixed structure takes upon annealing to ultimately return to dc-Si, as well as a method to definitively differentiate hd-Si from dc-Si. The bc8/r8 structure is found to anneal to dc-Si via the intermediate phases of Si-XIII and hd-Si. the latter is shown to have a far higher thermal stability then previously reported.
- Chapter 7 - Contains concluding remarks and future directions.

Chapter 2

Literature Review

This chapter presents the literature regarding the exotic phases of Si with a focus on those formed via indentation. This literature is presented as part of the wider context of phases that have also been formed via other methods, primarily using diamond anvil cells (DACs). The phases forming upon annealing of the metastable structure and the properties of these phases are also covered. Due to this work covering several different aspects of Si, some specific topics within literature are only relevant for a single chapter. In these cases, those topics are not reviewed in great detail here. Instead, a more specific, detailed review is presented at the start of the relevant chapter. Where this has occurred are indicated in the text with a reference to the more detailed review. As there has been a wide range of naming conventions used for the different phases within the literature, an overview of the naming conventions is presented first.

2.1 Nomenclature

The phases of Si were initially numbered in order of their discovery. For example, diamond cubic Si (dc-Si) was designated Si-I, while the first new phase discovered was named Si-II. This naming convention can be seen in older studies such as in Ref. [27] and the references contained within. Such a naming convention does not convey any information regarding the crystal structure of the phase and further, identical structures in other related elemental systems (such as Ge) have been given different numerical designations. For example, the hexagonal diamond structure of Si is called Si-IV but the same structure in Ge is referred to as Ge-V. Hence, this nomenclature is non-ideal. Some studies have named the structures after the space group (e.g. Ref. [26]), the Pearson symbols (e.g. Ref. [18]), or a name based on the unit cell structure and atomic basis (e.g. Ref. [30]) of the various phases. Many theoretical studies predicted phases that have zeolite structures. Thus, the codes used by the International Zeolite Association and developed by O'Keeffe *et al.* [57] have also been used to designate the newly predicted phases in some studies. Crystallographic notation is clearly the most scientifically desirable as it reduces possible ambiguity, although this could lead to long and difficult-to-read discussions of the phase transformation processes presented in this thesis.

In this thesis, the common name based on the structure and unit cell (e.g. bc8-Si) is predominantly used where available. Not all phases have a designation under all the naming conventions. When unavailable, the Pearson symbol (generally for experimentally verified phases, such as hP2-Si) or the zeolite code (generally for theoretically predicted phases, such as mep-Si) will be used. Only if no structural information is present will the numerical naming convention be used (such as Si-XIII, where no structure has been determined). The experimentally formed phases with their various naming conventions are presented in Table 2.1.

Common Name	Space Group	Pearson Symbol	Zeolite Code	Numerical
dc-Si	F d -3 m	cF8	dia	Si-I
(β-Sn)-Si	I 4_1/a m d	tI4		Si-II
bc8-Si	I a -3	cI16	gsi	Si-III
hd-Si	P 6/3 m c	hP4	lon	Si-IV
sh-Si	P 6/m m m	hP1		Si-V
Cmca-Si	C m c a	oC16		Si-VI
hcp-Si	P 6_3/m m m	hP2		Si-VII
				Si-VIII
				Si-IX
fcc-Si	F m -3 m	cF4		Si-X
Imma-Si	I m m a	oI6		Si-XI
r8-Si	r -3	hR24		Si-XII
				Si-XIII
st12-Si	P 4_1 2_1 2	tP12		
bt8-Si	I 4_1/a	tI16		
allo-Si			TON	
Si_{136}			mep	
Si_{24}			cas	

Table 2.1: A table of the experimentally observed phases of Si. The names in bold will be used to designate the phase within this thesis.

2.2 Phases of Si formed via DAC

There are a number unique crystalline phases of Si that have been formed via pressure application within a DAC. A schematic showing the series of DAC-induced phase transformations in dc-Si is presented in Fig. 2.1(a). In these experiments, dc-Si is held between two diamonds that are brought together to apply pressure to the sample. At a pressure of ∼11 GPa a semiconductor to metallic transition occurs and (β-Sn)-Si is formed [24]. The β-Sn structure is a body centred tetragonal phase with sixfold coordination and is 22% more dense than dc-Si [58]. One very interesting feature of this transformation is that it has been reported to be sluggish [32, 59]. That is, the transformation does not occur immediately after the critical pressure is reached. Instead, it is reported to occur over a period of several minutes [60, 61]. Further pressure increase causes a series of metal-to-metal transformations. Imma-Si is formed at ∼13 GPa [26]. This is followed by a transformation to sh-Si at ∼15 GPa [25]. Further transformation to Cmca-Si occurs at ∼38 GPa [28] which transforms to hcp-Si at ∼42 GPa [28]. Above ∼79 GPa, a final transformation to fcc-Si occurs. This phase is found to be stable up to 248 GPa, the highest pressure tested for Si in a DAC [62]. These high pressure metal-to-metal transformations are generally reported to be reversible upon pressure release. However, the (β-Sn)-Si transformation is not reversible due to the extremely large volume collapse compared to dc-Si [58]. Upon decompression to ∼9 GPa, (β-Sn)-Si transforms to r8-Si, which is a rhombohedral phase with 8 atoms in its unit cell [63]. This phase usually further transforms to bc8-Si at ∼2 GPa, a body-centred cubic phase with 8 atoms in its unit cell. This phase remains stable even after complete pressure removal [32].

Two other tetragonal phases have been reported upon rapid unloading in a DAC. The phase called Si-VIII appeared to form via rapid unloading from 14.8 GPa while Si-IX appeared to form via rapid unloading from 12 GPa [64]. The structures of these two possible phases are unknown. Note that larger devices created for pressure application (such as Paris-Edinburg cells [65] and multi-anvil presses [66]) have also been used to induce phase transformation in dc-Si and a similar set of transformations has been observed with these devices.

Annealing of bc8-Si results in a transformation to the hexagonal diamond phase (hd-Si) at 200°C [32]. Further annealing does not result in any new stable phase. Rather, Brazhkin *et al.* found that the structure returns to the energetically favoured dc phase at 750°C [67]. The recoverable phases of Si mentioned above are considered metastable phases as they exist in a temperature and pressure regime in which dc-Si is the energetically favourable phase. Thus, it is necessary to consider the mechanism of transformation from (β-Sn)-Si that result in these metastable phases. Not much has been published regarding Si-VIII and Si-IX outside of their initial discovery, so the mechanism for their formation has not been reported. However, for the β-Sn to r8 to bc8 to hd to dc pathway it has been proposed that a high kinetic barrier exists

between the β-Sn phase and the energetically stable dc phase [67]. Conversely, the transition between (β-Sn)-Si and r8-Si has been experimentally observed to have only a small hysteresis between the forward and reverse transformation, suggesting only a small amount of strain is required to drive the transition [63]. Indeed, a subsequent study comparing the relative atomic positions within the unit cell of these two phases noted that only a 2% strain was required to transform the unit cell from [30]. In that same study, Piltz *et al.* also reported the structural similarities between r8-Si and bc8-Si. In contrast, annealing of r8-Si held at 10 GPa have observed an abrupt transition to dc-Si which suggests a strong kinetic barrier between the two phases [45]. Similarly, the direct transformation from bc8-Si to dc-Si has been proposed to be kinetically hindered, resulting in the kinetically favourable intermediate hd-Si structure being formed upon annealing [67].

It is worthwhile noting that variations in the experimental set-up (such as using a-Si as the precursor material [68–70] or lowering the experimental temperature [71]) may result in slight variations in the transformation pathways (e.g. changing the critical pressure for transformation). No new crystalline phases are observed in these studies.

2.3 Phases of Si formed via Indentation

Indentation involves pressing a hard indenter tip (typically made from diamond) into a sample material. This technique was developed as a method for measuring the hardness of materials [72, 73]. In studies of the phases of Si, however, this technique can also be used as an alternate pressure-application system [36–39]. The pressure from indentation is applied only along the axis of indentation (i.e. uniaxial loading), and pressures up to the phase transformation threshold (11 GPa) can be routinely achieved in dc-Si [74–77]. This technique leads to slight differences in the phase transformations observed in indentation studies compared to those in the previously mentioned DAC studies. A schematic showing the transformations via indentation-induced pressure is presented in Fig. 2.1(b).

An indentation-induced transformation in Si was first reported in 1972 when a large decrease in electrical resistance was observed during loading [78]. It was further noted that the hardness of dc-Si was very similar to the critical pressure ($\sim$11 GPa) required for the transformation to the metallic phase in DAC studies [78–81]. Further *in situ* electrical resistance measurements during indentation studies supported the suggestion that the observed transformation is a dc-Si to metallic transition. That is, the indentation process was shown to be plastic after transformation to a metallic phase. Such studies indicate a transformation to a more dense phase [61, 74] and also the metallic-like flow of the deformed material out from under the indenter tip [36]. These studies motivated the proposal that the critical pressure for the metallic transition does in fact correlate with the indentation hardness, concluding that indentation

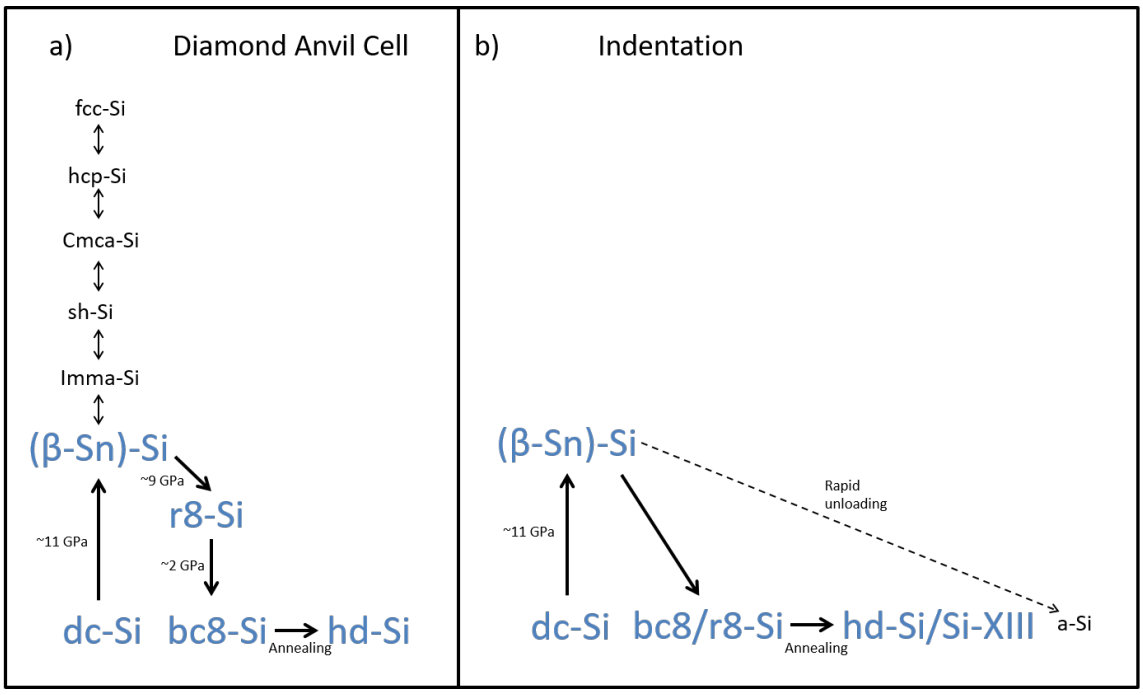

Fig. 2.1: A schematic showing the phase transformations induced in dc-Si via pressure application (a) in a DAC and (b) during indentation. The phases that feature prominently within this thesis have been emphasised (blue and large) and the pressures at which these transformations occur have been labelled (for the well-reported transformations).

may provide an experimental tool for observing pressure-induced phase transformations [82]. It has commonly been assumed that a dc-Si to (β-Sn)-Si transformation occurs in a manner similar to the transformations that occur in DAC experiments [39, 83–85]. However, theoretical studies have also predicted the formation of a metallic body centred tetragonal phase with fivefold coordination (bct5) under indentation-induced pressure [86–90]. Whereas the transformation to (β-Sn)-Si has been reported via *in situ* Raman microspectroscopy studies [43], such *in situ* studies have also suggested the possible presence of bct5-Si [91]. Most importantly for this thesis (which focuses on the metastable phases of Si) is that, in indentation, the dc-Si to metallic phase transition is also non-reversible. That is, exotic phases are formed rather than a return to dc-Si.

Interestingly, upon fast pressure release, a transformation to a-Si occurs [46, 75, 92]. The a-Si formed is structurally unique from a-Si formed via other methods of solid-state amorphisation such as ion-implantation [47]. Upon slow pressure release, a mixed structure comprised of both bc8-Si and r8-Si is recovered [37, 38, 46, 50, 76, 93]. The Raman peaks associated with both phases are reported to appear at the same point of unloading at a contact pressure of 5.7 GPa [91]. This differs from the transformation in DAC experiments where a two step process has been found (i.e. a transformation to r8-Si at ~9 GPa occurs first which is followed by a

transformation to bc8-Si under further pressure release to ∼2 GPa). It has been suggested that the presence of r8-Si after complete pressure removal is due to residual stress remaining within the sample [41, 44, 93, 94].

Annealing of the bc8/r8 mixed structure leads to further transformation to hd-Si (which was also observed after annealing of bc8-Si recovered from a DAC), as well as a new phase with an, as yet, unknown structure designated as Si-XIII [41, 45, 95]. The exact pathways and temperatures of these transformations remain a topic of discussion and the literature on this topic will be covered in more detail in section 2.5.

The ability to form extra metastable structures (such as r8-Si, Si-XIII, and pressure induced a-Si) are a key difference between indentation-induced phase transformations in Si and those occurring in DACs. There are several other differences between the two methods, which are discussed below.

2.3.1 Observed Differences between Indentation and DACs

Indentation experiments also typically result in a damaged region of non-phase transformed material being observed surrounding the phase transformed region after pressure removal. A BF TEM image of a transformed region cross-section is shown in Fig. 2.2. Significant crystalline damage is typically observed within this surrounding material [39–41, 55, 92, 93, 96]. This damaged region can take several forms, such as slip bands [39, 40], dislocations [96], and cracking [97, 98]. Within this thesis, the formation of slip bands and dislocations within the surrounding material will be collectively referred to as the nucleation and propagation of crystalline defects which, as will be shown, is a deformation process that competes with phase transformation. Most studies have observed significant crystalline defects alongside the phase transformed region formed via indentation. However, a recent study has reported the presence of phase transformation as the sole form of plastic deformation under certain loading conditions [55]. When the maximum load is increased above these loading conditions, both phase transformation and crystalline defects are once again observed together. Surprisingly, the volume of phase transformed material formed at this higher load was smaller than that at the lower load where phase transformation was the sole mode of plastic deformation. The underlying mechanism that causes this counter-intuitive observation is explored in detail in Chapter 5.

The two primary stresses induced under indentation-induced pressure are hydrostatic pressure and shear stress [50, 99, 100]. It has been proposed that nucleation and propagation of crystalline defects is primarily shear stress driven [39, 101] while phase transformation is thought to be primarily driven by hydrostatic pressure [54]. Thus, the relative distribution of these two stress fields plays an important role in the formation of the desired phase transformed

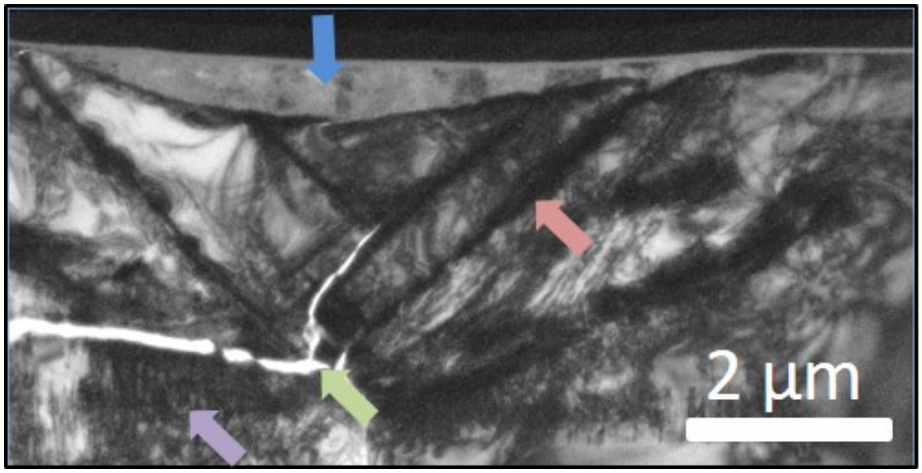

Fig. 2.2: A cross-sectional BF TEM image of the area under a residual impression after indentation loaded from the top of the image. A phase transformed region near the sample surface is indicated by the blue arrow. Crystalline defects such as slip (red arrow), cracks (green arrow), and possibly dislocations (purple arrow) are also indicated. Adapted from Ref. [55]

material.

The distribution of these two stress fields in indentation point loading is predominantly dependent on the tip shape. A variety of tips are commonly used for indentation, from spherical tips of varying diameter [73], to 3- and 4- sided pyramidal shapes (i.e. Berkovich and Vickers respectively) [72], and flat punches [102]. Regardless of the shape, the maximum of hydrostatic stress lies at the centre point of contact between the indenter and the sample [99, 100]. The pressure gradient surrounding this point differs significantly with respect to indenter shape, with spherical tips producing the most uniform and slowly varying pressure-gradient distribution [49–51, 55].

The effect of shear stress on the dc-Si to (β-Sn)-Si transformation is a topic where the literature lacks a consensus. It has been reported that the critical pressure for transformation is sensitive to the shear component in DAC experiments [24, 32, 52]. This is supported by theoretical modelling [50,53,99,100,103] and has also been proposed to be significant in indentation studies [54, 104]. Han *et al.* predict that, under the right hydrostatic pressure/shear stress conditions, the transformation may be possible at as low as ∼6 GPa [103]. and attempts (with varying success) have been made to experimentally verify this prediction [43, 59]. Due to the tip-dependent, non-uniform distribution of pressure, calculations of the pressure experienced by the sample is non-trivial. Such calculations depend critically on a knowledge of the exact tip shape (including tip surface roughness) and contact with the sample. Therefore, experimentally reported values for the critical pressure of phase transformation must be considered within the context of the experimental set-up. For example, Gerbig *et al.* report a transforma-

tion occurring during loading at a mean contact pressure of 5.2 GPa with a spherical tip [43]. However, transformation is dependent on maximum (not mean) pressure. Thus, maximum pressure at the point of phase transformation is necessarily higher than the reported value.

Accurate measurement of the relationship between the shear stress and critical hydrostatic stress for phase transformation is further complicated by the sluggish nature of the transformation from dc-Si to (β-Sn)-Si [60, 61]. That is, the sample may experience pressure/stress conditions sufficient for the transformation to (β-Sn)-Si but does not transform due to sluggish nucleation and insufficient time under these conditions. Therefore, the possibility of phase transformation initiating at hydrostatic pressures significantly above ~11 GPa should be considered. Experiments to investigate the sluggish phase transformation is presented in Chapter 5.

Indentation also differs from DAC experiments due to the volume and shape of the phase transformed regions recovered. Indentation can only form phase transformed regions on the near-surface of a sample. Each individual indent transforms a region with a depth in the order of tenths of a μm and a surface area in the order of μm^2, largely subject to tip size and shape [55, 85, 105]. This volume is smaller than that achievable from a DAC that typically produces samples in the order of 10^{-3} mm^3 (10^6 μm^3) [18] and much smaller than the volumes achievable from the larger Paris-Edinburgh cell [65] or multi-anvil cell [66] which can be up to several cubic millimetres. The advantage of indentation-induced phase transformed regions is the ability to accurately place such regions directly onto bulk device grade semiconductor wafers and overlap multiple indents to create larger patterns that are readily integrated into the surrounding material [56, 106]. Further, the production of these overlapping transformed regions can be performed in an automated fashion. It is believed that, should sufficient technological interest for these phase transformed regions be present, the indenter tip's size and shape can be reasonably scaled up to enhance the technological exploitation of the exotic phases [18].

2.4 a-Si as a Precursor Material

Besides dc-Si, a-Si has also been studied as a precursor for indentation-induced phase transformations. The a-Si used is a pure, voidless form that is made via self-ion implantation of Si ions [93, 106, 107]. Ion-implantation induced a-Si samples are annealed at 450°C for 30 minutes, allowing for short-range reordering of the amorphous network (relaxation) to occur [47, 108–110]. Such a step is beneficial for the formation of exotic phases as a relaxed a-Si sample has been reported to more readily transform to (β-Sn)-Si than unrelaxed a-Si [111–113]. Indentation of relaxed a-Si results in the formation of the bc8/r8 mixed structure in a similar manner to indentation of dc-Si [93, 106, 107, 111–113]. In fact, the use of relaxed a-Si as a pre-

cursor was found to promote the transformation to the bc8/r8 mixed structure on unloading over transformation to pressure-induced a-Si when compared to indentation of dc-Si under the same indentation conditions [107].

2.5 Annealing of bc8/r8 Si

Annealing of bc8-Si recovered from a DAC at 200°C results in a transformation to hd-Si [32, 114, 115]. Further annealing at 750°C leads to a transformation to dc-Si [67].

The transformations observed in the bc8/r8 mixed structure formed via indentation are more complex. Kailer *et al.* first reported the transformation of the bc8/r8 mixed structure to hd-Si after thermal annealing at 200°C followed by subsequent transformation to dc-Si after further annealing at 500°C [38]. Domnich *et al.* reported the presence of unidentified Raman peaks alongside bc8-Si, r8-Si and hd-Si after annealing at temperatures between 150°C - 250°C [83]. As these peaks could not be attributed to any known phase of Si, the authors designated the source of these peaks to a new phase of Si. This phase was named Si-XIII as it was the 13th phase of Si to be reported. Several studies have attempted to understand the transformation pathways from the bc8/r8 mixed structure to the thermally stable dc-Si end phase under different indentation/annealing conditions. These conditions include sample thickness [44], residual indent size [93], the crystalline nature of the surrounding material [41], and the specific method of annealing [94] (see section 6.1 for more details on these studies). These studies report different transformation pathways and different transformation temperatures; some even report that the intermediate phases (hd-Si and Si-XIII) are not present. The only point all studies agree with is that the end phase is dc-Si after high temperature annealing.

2.5.1 DAC Pressure-Temperature relationship

The complexity of the transformations of the bc8/r8 structure formed via indentation under annealing motivated an *in situ* annealing DAC study of the bc8 and r8 phases [45]. Haberl *et al.* observed that bc8-Si held in a DAC at 3 GPa transformed directly to hd-Si in a manner similar to bc8-Si that has been completely recovered from a DAC. Further, it was observed that r8-Si held in a DAC at ∼10 GPa transformed directly to dc-Si with a critical temperature of 255°C. That is, Si-XIII was not produced via DAC pressurisation under the conditions presented in their study. Due to the open questions regarding the transformation pathways of the phases on annealing, this present work aims to address several of the issues regarding annealing of the bc8/r8 mixed structure in Chapter 6.

Potential Models for Si-XIII

As mentioned above, Si-XIII is a new phase of Si that has only been observed from annealing of the bc8/r8 mixed structure formed via indentation. Many theoretical studies have been published on the energetically plausible phases of Si (see Ref. [18] and the references within), of which two are particularly relevant in regards to the possible structure of Si-XIII. Zhao *et al.* modelled a tetragonal structure with 12 atoms in its unit cell (t12-Si, $P4_2/ncm$, **cdp**) [116]. The simulated Raman spectrum of t12-Si was found to have several peaks that matched those experimentally observed for Si-XIII. A second potential structure was reported by Mujica *et al.* who found a tetragonal structure with 20 atoms in its unit cell ($P4_12_12$, tP20) which they suggest is an even more likely candidate for the structure of Si-XIII than the t12-Si phase [23].

An attempt to characterise Si-XIII using synchrotron-based XRD data is presented in Appendix A. The agreement between the structures predicted and the XRD data is also briefly discussed.

2.6 Other Methods for Forming Exotic Phases in Si

While this work is primarily focussed on indentation as the method for forming exotic phases, it is important to acknowledge that (in addition to DAC- and indentation-induced pressure) there are two other methods to form these phases. The use of laser-induced pressure/temperature to phase transform dc-Si and the use of Si-rich chemical precursors are briefly covered below for completeness.

2.6.1 Laser-induced Phase Transformation of Si

Several studies have reported the formation of exotic Si phases after femtosecond pulsed-laser irradiation. Laser irradiation of the surface of a Si sample produced several observed laser-induced processes, one of which is phase transformation. In earlier studies, a-Si was reported within the phase transformed regions [117, 118]. More recent studies have also reported the presence of r8-Si [119, 120] as well as Si-VIII [121]. However, the other laser-induced processes (such as laser ablation and surface rippling [122]) interfered with the process of phase transformation.

By focussing the laser through a transparent capping layer to a point below the surface, subsurface micro-explosions could be induced using fs-laser pulses. Rapp *et al.* reported >TPa pressures and $>10^5$ K temperatures via these explosions [34]. This caused a transition from dc-Si to a dense plasma, which cooled and decompressed at an ultra-rapid rate after fs-laser pulsing. Under such extreme non-equilibrium conditions, two new exotic phases of Si

were observed within the recovered sample. The first is a simple tetragonal structure with 12 atoms in its unit cell (st12-Si) which has previously never been found experimentally for Si but is well known for the sister group IV element Ge [123]. The second is a body centred tetragonal structure with 8 atoms in its unit cell (bt8-Si). It was suggested that such phases could be formed via laser-induced subsurface micro-explosions due to the ultra-rapid decompression resulting in transformation directly from the denser, non-(β-Sn) metallic phases [34] (possibly similar to the reported formation of the tetragonal phases Si-VIII and Si-IX [64]).

2.6.2 The use of Chemical Precursors

Exotic phases of Si have also been synthesised from a Si-rich precursor material. One such method is to react Si-rich molecular materials (such as Li_3NaSi_6) with the appropriate catalysts to remove the Li and Na components [124]. Schenering *et al.* reported that the remaining Si chains combine while retaining much of their structure to form a phase known as allo-Si, which is considerably less dense than dc-Si.

A second method is to produce Si clathrates. A clathrate is a structure where molecules of another element are physically caged within a Si structure [125–128]. The non-Si element can be removed from the precursor which produces a pure Si phase that retains the clathrate shape [129]. Gryko *et al.* produced a structure with 136 atoms in its unit cell (Si_{136}) from a Na_xSi_{136} precursor [130]. Kim *et al.* formed a structure with 24 atoms in its unit cell (Si_{24}) from a Na_4Si_{24} precursor [33]. They further reported that Si_{24} is $\sim$7% less dense than dc-Si. This is in contrast to the phases formed via pressure application which are all denser than dc-Si.

2.7 Relevant Properties of the Exotic Phases of Si

2.7.1 The bc8 Phase

Electrical Properties

As the first metastable phase of Si to be recovered from a DAC, bc8-Si was initially observed to be "more metallic than ordinary [dc-]Si" [32]. More recent studies report that nanoparticles of bc8-Si may be useful for multiple exciton generation solar energy conversion [131] that may overcome the Shockley-Queisser limit [132].

Early theoretical studies have modelled bc8-Si as either a semiconductor [133] or as a semi-metal [134, 135]. Electrical measurements on the microcrystalline bc8-Si samples recovered from a DAC by Besson *et al.* reported the material to be semi-metallic with an indirect

overlap in the band structure of 0.3 eV [115]. More recently, the formation of bulk bc8-Si [136] has allowed for improved electrical measurements that show bc8-Si is a semiconductor with an ultra-narrow band gap (∼30 meV) and significantly reduced thermal conductivity relative to dc-Si [137].

Structural Properties

Bc8-Si is a body-centred cubic lattice with a *Ia-3* space group [30, 138]. Its atoms are located on the 16(c) sites (x, x, x) using Wyckoff notation. Thus, the body-centred cubic structure is defined using two structural parameters, unit cell length (a_c) and atomic location parameter (x_c). Furthermore, bc8-Si can also be equivalently described by a rhombohedral lattice with a *R-3* space group [30]. Piltz *et al.* used this unconventional space group to better compare bc8-Si with r8-Si (which has an *R -3* space group). Under this description, the atoms are located on the 2(c) (u, u, u) and 6(f) (x, y, z) sites. Therefore, the rhombohedral structure is defined using six structural parameters, unit cell length (a), unit cell angle (α), and atomic location parameters (u, x, y, z). The rhombohedral parameters are related to the conventional cubic parameters by $a = \frac{\sqrt{3}}{2}a_c, \alpha = 109.47°, u = 2x_c, x = 0.5, y = 0, z = 0.5 - 2x_c$. At ambient pressure, a_c = 6.636 Å and x_c = 0.1003° (based on former DAC studies).

2.7.2 The hd Phase

Electrical Properties

Besson *et al.* were the first to observe the semiconducting nature of hd-Si [115] for which they approximated a band gap of <1 eV which was in agreement with the theoretical studies of the time [133]. Further modelling of the phase concluded that the band gap is indirect [139, 140]. There has been renewed interest in the phase due to calculations that predict that high biaxial tensile strains of >4% can transform hd-Si into a direct band gap semiconductor [141].

Structural Properties

The structure of hd-Si is a hexagonal lattice with a *P6$_3$/mmc* space group [142]. The atoms are located on the 4(f) (1/3, 2/3, z) sites. Kasper *et al.* report that at ambient pressure the lattice parameters are a = 3.80 Å, c = 6.28 Å, z = 1/16. Interestingly, Wentorf *et al.* also report that the inter-atomic distance (2.35 Å) and the density (2.33 g/cm^3) are the same as dc-Si [32].

2.7.3 The r8 Phase

Electrical Properties

One of the reasons for the interest in recovering the r8 phase at ambient pressure is due to its predicted narrow band gap semiconducting behaviour and optical properties which are favourable for PV applications [143, 144]. The study of r8-Si has been conducted via density functional theory (DFT) using a local density approximation (LDA). Malone *et al.* predict that r8-Si is a narrow band-gap semiconductor with a band-gap of 0.24 eV with a far greater absorption than dc-Si across a significant portion of the solar spectrum [143] (as shown in Fig. 2.3). Further, it has also been predicted that r8-Si has a lower effective mass for charge carriers than dc-Si which allows for greater carrier mobility given identical crystal size/purity [144].

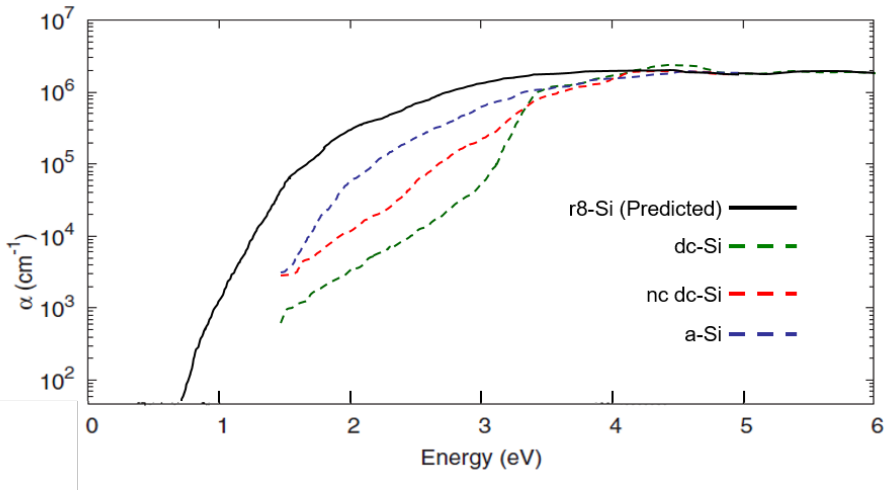

Fig. 2.3: The calculated optical absorption coefficient (α) for r8-Si is plotted in comparison with the coefficients for dc-Si, polycrystalline dc-Si, and a-Si. A solar absorption spectrum is also included for additional information. Adapted from Ref. [143]

Structural Properties

The structure of r8-Si is a rhombohedral lattice with a *R-3* space group [30, 63]. Similar to bc8-Si, the atoms are located on the 2(c) (u, u, u) and 6(f) (x, y, z) sites. Crain *et al.* report that, at 8.2 GPa within a DAC, a = 5.609 Å, α = 110.07°, u = 0.2921, x = 0.4580, y = -0.0369, z = 0.2645. A phase-pure sample of r8-Si has not yet been recovered at ambient, thus no structural parameters for ambient r8-Si exist in the literature.

2.7.4 The bc8/r8 Mixed Structure

Experiments have reported r8-Si is semiconducting by studying the electrical response of the bc8/r8 mixed structure to varied doping levels [77]. However, this study assumes the bc8-Si does not contribute due to its semimetallic nature [115]. More recent studies of the nature of bc8-Si [137] would suggest that this semiconducting nature would be better attributed to the bc8/r8 mixed structure as a whole. Further, the mixed structure has been shown to have comparable resistivity to dc-Si given similar crystal size [77].

Extracting the r8-Si contribution from the mixed structure is complicated by the fact that the ratio between the r8 and bc8 phase within the mix is not known. Attempts to calculate this phase fraction have been made previously. Using Raman microspectroscopy, Ruffell *et al.* compared the intensity of the r8-Si Raman peak at 355 cm^{-1} to the bc8-Si peak at 438 cm^{-1} and observed that the ratio between these two phases was always 4:1 in the favour of the 355 cm^{-1} peak independent of the size of the transformed region or the surrounding material. They interpreted this result to represent the bc8/r8 mixed structure as being 80% r8-Si and 20% bc8-Si. A comparison of these peaks has been previously employed in other studies, such as the initial observation that two phases are present [38], as a rough indicator of the predominance of a phase [44], or as a preliminary measurement of the transformation temperature of r8-Si [93]. However, there still exist factors that must be considered before making such a translation from peak intensity ratios to fractional volume. Most importantly, the intensity is not only dependent on scattering volume; it is also dependent on the Raman scattering cross-section, a value that differs between materials phases [145]. Secondly, there is also the assumption that the phases are homogeneously spread in the scattering volume despite the fact that the phases are reported to not be homogeneous within a residual impression [50]. Thus, an accurate ratio has yet to be reported.

This thesis aims to address this paucity of information regarding the phase ratios in Chapter 4. Some optical measurements on the mixed structure are also presented within that chapter.

Chapter 3

Experimental Methods

This chapter presents an overview of the experimental techniques used in this thesis. The technique used to induce pressure-induced phase transformations in Si within this work is indentation. The stress experienced by the sample during indentation was modelled by the simulation package Elastica [146]. The thermal stability of exotic Si phases was examined using both thermal and laser annealing. Residual indents were characterised using several methods to measure the phases present as well as other forms of plastic deformation. These methods include Raman microspectroscopy, X-ray diffraction (XRD), and cross-sectional transmission electron microscopy (XTEM). Samples measured by XTEM were thinned to electron transparency using focused ion beam (FIB) milling. The XRD results were radially integrated using the computer program Dioptas [147]. Rietveld refinement and peak fitting for these results was achieved using the computer program GSAS-II [148]. Finally, measurement of the optical properties of the residual indents was performed using optical spectrophotometry and photoluminescence microspectroscopy.

3.1 Indentation

Indentation was first developed as a method to measure hardness. Historically, a hard material (such as a steel or tungsten ball) was pressed into a material using a known force and the residual impression optically observed [149]. The hardness of the material could then be calculated by dividing the applied force by the optically measured size of the residual impression, commonly known as Meyer's hardness [150]. The use of optical microscopy to measure the residual impression created a physical lower limit for the size of the impressions that could be measured. In particular, this limitation prevented the hardness measurement of thin films as the indentation depth must generally be <10% of the film thickness to avoid interference from the substrate [151]. Hence very low loads leading to impressions below the optical limit were required to measure the hardness of thin films. Instrumented indentation, often referred to as nanoindentation, overcomes this limitation by introducing *in situ* measurement of the indenter tip's penetration depth [152]. That is, the applied force and the corresponding penetration depth are independently measured throughout force loading and unloading. By plotting the force and depth during loading and unloading (load/unload curve), the hardness of the ma-

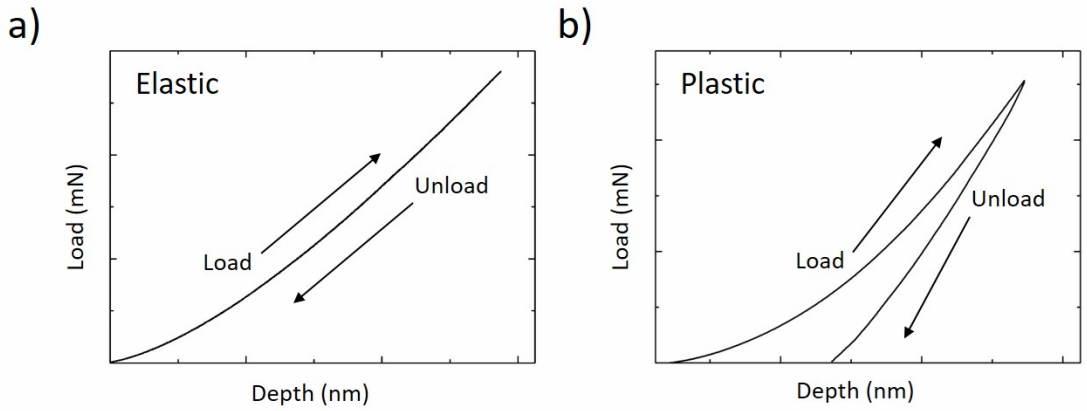

Fig. 3.1: Typical load/unload curves collected from indentation showing (a) elastic and (b) plastic behaviour.

terial can be extracted if the shape of the tip is known precisely [72, 73]. Interpreting these load/unload curves is covered in more detail below. Further differences from the early days of indentation include replacing the steel or tungsten ball with a much harder indenter tip, commonly made from diamond [149]. Such diamond tips are available in a variety of shapes, where shape affects the mechanical response of the sample by varying the pressure distribution [38, 51]. One key advantage of instrumented indentation that is exploited in this thesis is that the loading cycle can be controlled, and thus the tip may be held at a desired load for a set amount of time before further loading/unloading. The introduction of this hold duration results in an interesting variety of loading possibilities.

Two indentation load/unload curves are presented in Fig. 3.1. A curve from indentation that responded elastically is shown in Fig. 3.1(a). For indents that respond elastically, the loading and unloading curves overlap and there is no residual depth after complete pressure removal. Figure 3.1(b) shows an indent that has responded plastically. In this case, the unloading curve departs from the load curve and a residual depth remains even after complete pressure removal.

Load/unload curves can be used to determine a material's mechanical properties. A schematic of a load/unload curve with several important parameters indicated (from Ref. [153]) is presented in Fig. 3.2(a). The parameters are the maximum applied load (P_{max}), maximum penetration depth (h_{max}), final depth (h_f), and the contact stiffness from the upper section of the unload curve ($S = dP/dh$). A schematic of the unloading process showing parameters relating to the contact area geometry at maximum loading and complete unloading (from Ref. [153]) is presented in Fig. 3.2(b). The important parameters are the contact depth (h_c) and sink-in depth (h_s). For a given indenter geometry, the Oliver and Pharr method calculates the hardness (H) and elastic modulus (E) using these parameters [72]. A brief overview of this

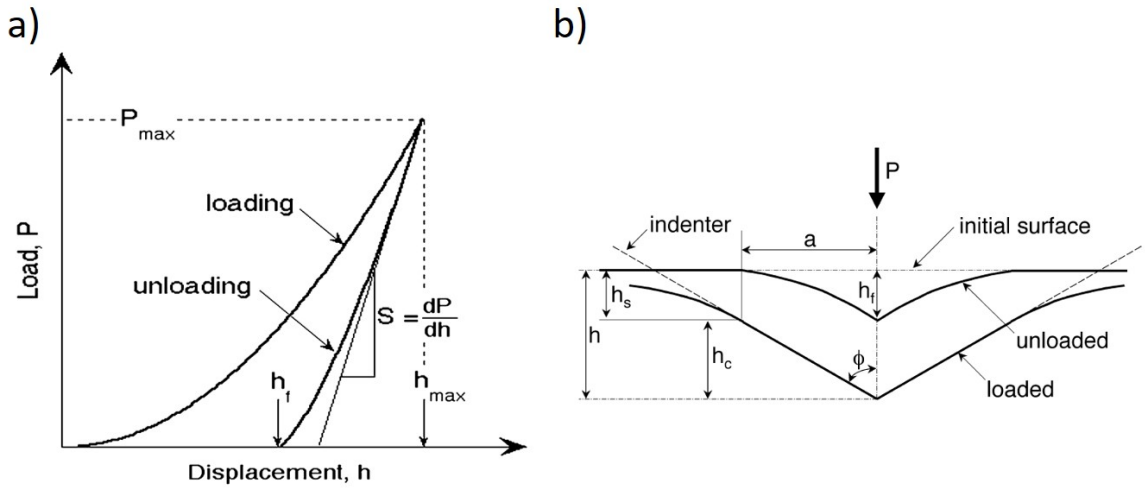

Fig. 3.2: From Ref. [153]: (a) Schematic of a load/unload curve showing important measured parameters. (b) Schematic of the unloading process showing important parameters regarding the contact geometry.

method is presented here. For further details, please refer to Ref. [72, 153].

This method begins with the relationship between the stiffness and the reduced modulus (E_r) as presented in Refs. [154–158]:

$$E_r = \frac{\sqrt{\pi}}{2}\frac{S}{\sqrt{A}} = \frac{1-v^2}{E} + \frac{1-v_i^2}{E_i} \tag{3.1}$$

where A is the projected contact area, v_i and E_i are the Poisson's ratio and elastic modulus for the indenter, and v and E are the same properties for the sample.

As the stiffness at initial unloading can be measured from the slope of the load/unload curve, the elastic modulus can be determined if the contact area at peak load is known. The contact area is related to the contact depth by a tip area function [i.e. $A = F(h_c)$]. This area function is unique to each indenter tip and is established for each tip by indentation into a material of known elastic modulus prior to indentation of the sample. In this work, the tip area function of the tips used were determined by indenting fused quartz (E = 69.9 GPa).

The contact depth can calculated from the maximum indentation depth by the equation:

$$h_c = h_{max} - \epsilon\frac{P_{max}}{S} \tag{3.2}$$

where ϵ is a constant that is dependent on tip geometry (for example $\epsilon = 0.72$ for a conical tip, while $\epsilon = 1$ for a flat punch) and $h_{max} = h_c + h_s$ [159]. Note that this calculation of the

contact depth does not account for the piling up of material outside of the contact area. That is, the impact of any material that flows out from under the tip during loading is assumed to be negligible.

Further, once the contact area is determined, the hardness (H) can be calculated from the known geometry of the indenter tip using:

$$H = \frac{P_{max}}{A} \tag{3.3}$$

3.1.1 Interpreting Si Load/Unload Curves

For many materials (such as Si), much information can be extracted from the load/unload curves. In particular, discontinuity events may be present within the curve that may be indicative of the sample deforming plastically in a specific manner [46, 92]. Figure 3.3 presents two typical load/unload curves collected from indentation in dc-Si using a spherical tip. The curve in Fig. 3.3(a) contains two pop-in event (indicated by the red arrows), which are discontinuities in the loading curve. These have previously been associated with a transformation to a denser metallic β-Sn phase [92] or alternatively to the nucleation and propagation of defects or cracking. As mentioned previously in Section 2.3.1, the term crystalline defects is used within this thesis to include defects such as dislocations [96] and slip [39, 40]. It should be noted that pop-in events due to transformation to the β-Sn phase has been observed to arise as a result of a sudden extrusion of the metallic phase from under the tip [39]. Multiple pop-in events can be observed within a single loading curve as phase transformation and defect nucleation may occur multiple times within the same indent.

The pop-out event observed in the curve shown in Fig. 3.3(b) (indicated by the blue arrow) is a discontinuity in the unloading curve. Pop-outs can be associated with the sudden density decease (i.e. volume increase) from the transformation of the high density (β-Sn)-Si to the less dense bc8/r8 mixed structure [46]. Thus, the presence of a pop-out discontinuity during unloading signifies a phase transformation has occurred during the unloading process, which requires a dc-Si to (β-Sn)-Si transformation to have occurred during loading. In this thesis, the discontinuities (pop-ins and pop-outs) were used as an early indicator as to what type of plastic deformation was present within the residual impression. Note that, while a pop-out event is definitely an indicator of the formation of a significant volume of the bc8/r8 structure under the indenter, it has been suggested that the initial load at which transformation from (β-Sn)-Si to the bc8/r8 structure first occurs does not necessarily correspond to the load at which a pop-out is observed [93, 160].

Figure 3.4 presents a typical load/unload curve that includes a hold interval at the maximum load. This curve differs slightly from those often presented in other studies [39, 51, 92, 161]

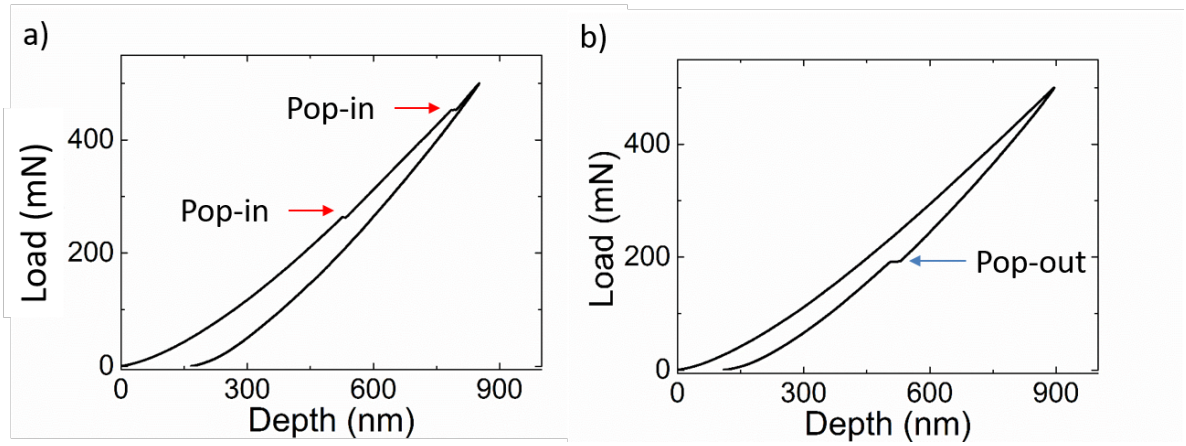

Fig. 3.3: Typical load/unload curves from dc-Si indentation showing (a) two pop-in events (red arrows) that indicates the nucleation and propagation of crystalline defects or formation of the metallic β-Sn phase and (b) a pop-out event (blue arrow) that indicates the transformation to the bc8/r8 phase from the denser metallic phase

due to the change in penetration depth at maximum load due to the hold duration. This displacement is due to either thermal drift during the hold period or to creep in the sample under load, the impact of which is discussed below in Section 3.1.1. It should be noted that a hold interval is used as a method of instrumental drift analysis in other studies although this is often during unloading [162]. However, in Hysitron indenters such as the ones used in this work, the drift analysis is performed before loading. This pre-load drift analysis is automatically accounted for in the final load/unload curve. The hold interval included in this work is not to calculate drift but solely for the purpose of promoting nucleation limited plastic behaviours.

Drift

As discussed above, the load/unload curve of indentation in Si may contain information regarding phase changes and other plastic deformation behaviours. Due to effects such as thermal drift, care must be taken to ensure the curve accurately represents the deformation of the sample and is not instead dominated by artefacts [163, 164]. Oliver *et al.* report that, even if the system is thermally buffered from the surrounding environment, small thermal fluctuations will still exist within the indentation system's components [72]. Due to such fluctuations in temperature between the indenter and the sample, heat transfer may occur upon contact which causes thermal drift [165]. This leads to changes in the measured depth that are independent of the sample's response to indentation. To minimise this effect, the instrument used here conducts a drift analysis prior to each indentation. This involves placing the tip in contact with the sample at a very low load (2 μN). Then, the drift is given time to stabilise

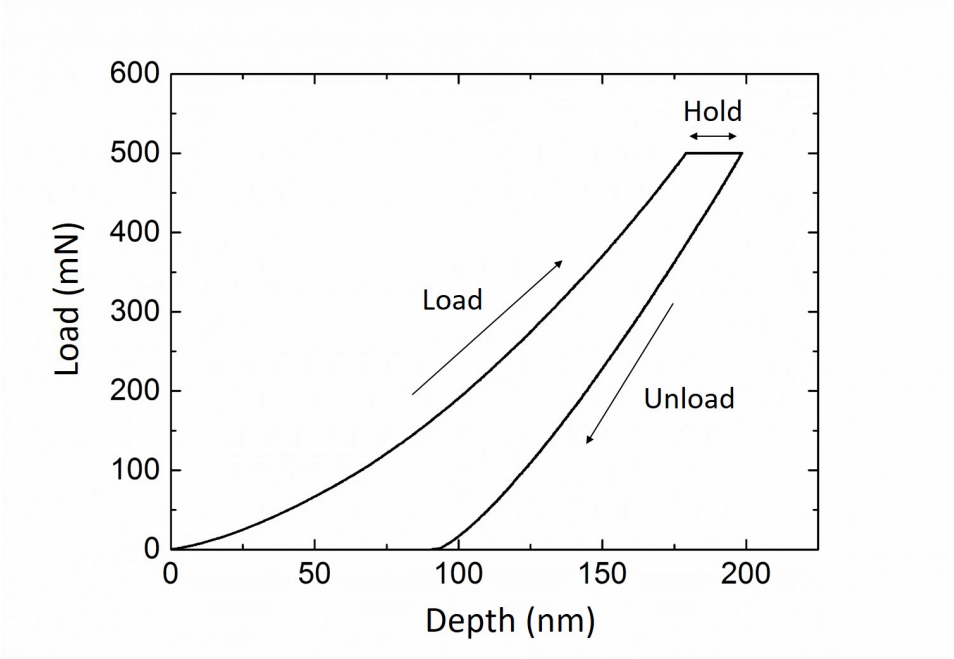

Fig. 3.4: A typical graph showing the measured depth versus load during indentation (load/unload curve). The segments associated with the loading, holding at maximum load and unloading are indicated. The factors contributing to the change in depth during the hold are discussed in Section 3.1.1.

(typically 20 s). After stabilising, the affect of drift on the depth is analysed (typically over 20 s). The final calculated drift value (in nm/s) is then subtracted from the measured depth in the load/unload curve. The corrected load/unload curve is then used to calculate estimated hardness as indicated earlier. In many of the measurements presented in this thesis, the tip is also held at maximum load for an extended period of time (up to 60 minutes). Due to such long time periods, the drift value calculated at the start of the indent may not be accurate, especially in the indents with longer hold durations. The error in the drift due to this difference can not easily be decoupled from change in depth due to other factors such as phase transformation from dc-Si to the denser β-Sn phase or even creep of the sample under load following phase transformation. The implications of this issue during hold time experiments conducted in this work is that the changes in depth during the hold period cannot be used to measure the rate at which the sample transforms between phases of differing density.

3.1.2 Indentation System Details

Two different indentation systems were used in this work to induce phase transformations. A Hysitron TI 950 capable of applying a maximum load of 10 N was used to perform the majority of the pressure-induced phase transformations [166]. An Ultra-Micro Indentation System

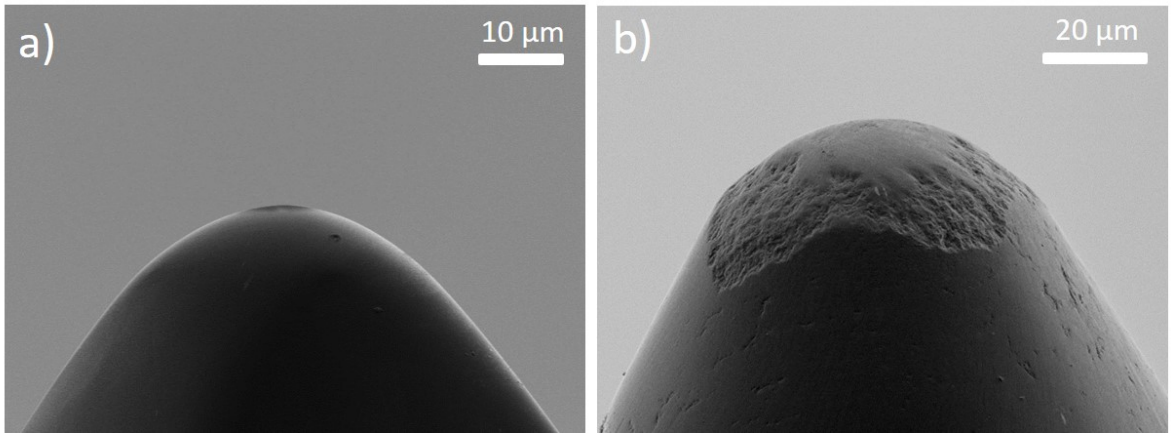

Fig. 3.5: SEM image of the (a) ∼22 μm diameter indenter tip and (b) ∼60 μm diameter indenter tip used in this work.

(UMIS-2000) was also used for this purpose to maintain consistency with previous studies. Spherical indenter tips where chosen for both of the indentation systems as they produce a lower pressure gradient in the material which is beneficial for phase transformation [55].

The TI 950 Hysitron Triboindenter fitted with a 3D Omniprobe^{TM} is capable of applying a maximum load of 10 N. This indenter was used to form pressure-induced phase transformation in dc-Si. Two spherical diamond indenter tips were used. One had a diameter of ∼22 μm, the other had a diameter of ∼60 μm [as shown in Fig. 3.5]. Features on the surface of the larger tip were previously reported to have a negative impact on phase transformation volume and shape within certain maximum load regimes [55]. That is, at lower loads the scarring on the tip would act as an indenter with significantly smaller radius and create phase transformed regions inconsistent with the expected size/shape of indenter tip. Thus, care was taken to only utilise this tip for high loads outside of these regimes. This indentation system is also capable of holding the sample at a specified force for prolonged periods of time. This is useful for probing nucleation limited behaviour. A UMIS-2000 capable of applying up to 1 N maximum load was also used to induce phase transformations. A spherical diamond indenter tip with a diameter of ∼40 μm was used (not shown).

3.1.3 Indentation Simulation Software: Elastica

Pressure distributions during indentation were simulated using the program Elastica® [146]. Elastica® calculates the hydrostatic and shear stress experienced by the material during indentation in the elastic regime. This is done by modelling the sample as an isotropic half-space with user-defined Young's modulus, Poisson's ratio, and density. Force is applied to the sample via a spherical or Berkovich shaped indenter tip made from diamond. Such calculations

Material	Young's Modulus	Poisson's Ratio	Density
Silicon	165 GPa	0.22	2.33 g.cm^{-3}
Diamond	1100 GPa	0.1	3.51 g.cm^{-3}

Table 3.1: The values used for the diamond tip and [001] dc-Si sample in Elastica® simulations on indentation pressure distribution before the onset of incipient plasticity. The values for diamond are included with the program while the values for Si are taken from Ref. [167].

can be used to consider the pressure distribution at the onset of incipient plasticity (i.e. the point at which plastic deformation first occurs). Importantly, the difference between the point of maximum shear stress (which is critical for the nucleation and propagation of crystalline defects) and the point of maximum hydrostatic stress (which is critical for phase transformation) at incipient plasticity can be obtained and such data are discussed in Chapter 5. The values used to simulate the tips and the samples are presented in Table 3.1.

3.2 Annealing

In this work, thermal annealing was used to promote physical changes in the sample structure including phase transformation or to relax a-Si. In particular, annealing was used to drive the transformation from the bc8/r8 mixed phase to other thermally-induced phases, with the thermally stable dc-Si phase the final state as detailed previously in Section 2.5. Three different methods of annealing were used in this work. Heat stage annealing, furnace annealing, and laser annealing. A THMS600 Linkam temperature stage was used for anneals up to 240°C. These anneals occurred in a flowing N_2 atmosphere. A Lindburg Blue furnace filled with an Ar_2 atmosphere was used for annealing between 240°C - 1000°C. Heat stage and furnace annealing will be collectively called "thermal annealing" in this thesis where appropriate, with the defining feature being that the entire sample is heated equally during such annealing in contrast to laser annealing.

Laser annealing was also performed as an alternate method of heating the sample. In contrast to thermal annealing, the heat from laser annealing is concentrated at the point at which the laser is absorbed [168, 169] and for fast scan rates the temperature of the sample is not uniform. Thus, the amount of energy/heat at a point within the sample is dependent on both the laser position as well as the absorption cross-section of the material to the incident laser. Note that different Si phases may have different laser absorption cross-sections. To achieve an anneal that was as homogeneous as possible at the sample surface, a 532 nm laser with a power of 400 kW.cm^{-2} was raster scanned across the sample at a rate of 1 μm/s. The laser annealing magnitude is reported in laser power flux (in kW.cm^{-2}) rather than temperature

in this thesis, as correlation between laser annealing conditions and equivalent temperature is dependent on the properties of the annealed material.

3.3 Raman Microspectroscopy

Raman microspectroscopy is an inelastic scattering technique that is sensitive to the local bonding environment and vibrational modes of neighbour atoms [145]. Thus, Raman microspectroscopy is a relatively quick, non-destructive method for measuring the presence of different crystal structures or bonding arrangements of the same element within the sample. This inelastic scattering is due photon-phonon interactions and excites the target from one vibrational state to another. This interaction slightly changes the energy of the interacting photon. The change between the wavelength of the incident and emitted photon is known as the Raman shift, which is measured in wavenumbers and has units of cm^{-1}. As the Raman shift is dependent on the vibrational states, this technique is sensitive to different phonon excitations. These excitations are dependent on the local bonding of the sample, but are independent of excitation wavelength. While the characteristic Raman peaks are associated with the local bonding of the material, other factors may also cause slight shifts in the vibrational energy states which may lead to shifting or broadening of the Raman peaks. These factors include (but are not limited to) residual stress, defects, temperature, crystallite size and crystal orientation [170]. Due to varying laser absorption cross-sections, the relative intensities of the peaks do not reflect the relative ratios of the corresponding material phases in the sample [145].

A Renishaw InVia Reflex Raman system equipped with a 532 nm laser (spot size $\sim$1 μm) was used in this thesis. This system was equipped with a 50x objective lens and a 2400 lines/mm diffraction grating. Figure 3.6 shows typical Raman spectra taken from a sample indented to form the bc8/r8 mixed phase. A dominant peak associated with dc-Si at 521 cm^{-1} is commonly observed in Raman spectra taken from residual indents presented in this work. This may be due to the surrounding or underlying dc-Si and will be discussed on a case-by-case basis within the results. The peaks at 385 cm^{-1} and 432 cm^{-1} are characteristic of the bc8 phase while the peaks at 170 cm^{-1}, 351 cm^{-1}, and 397 cm^{-1} are characteristic of the r8 phase [171,172]. The peaks associated with all the phases explored in this work are in Table 3.2 and the primary peak of each phase is highlighted. The phonon mode is also indicated where known.

3.4 Scanning Electron Microscopy

Scanning Electron Microscopy (SEM) rasters an incident beam of electrons across a sample and detects a selected type of emitted radiation (secondary electrons, back-scattered electrons, x-rays, light) to give information about the surface or near-surface of the material [175]. Within

Raman Shift (cm^{-1})	Phase	Phonon Mode	Reference
301.9	dc	2TA	[173]
520.3	**dc**	**TO**	**[173]**
182.4	bc8	T_g	[42]
373	bc8/r8		[42]
384.2	bc8	T_g	[42]
412	bc8		[42]
437.5	**bc8**	$\mathbf{E}_u$	**[42]**
463	bc8	E_g	[42]
496	hd	TO	[174]
514	**hd**	$\mathbf{A}_{1g}$	**[174]**
164.8	r8	A_g	[42]
170	r8	E_g	[42]
351.9	**r8**	$\mathbf{A}_g$	**[42]**
397.1	r8		[42]
200	Si-XIII		[44]
330	Si-XIII		[44]
475	Si-XIII		[44]
497	**Si-XIII**		**[44]**

Table 3.2: The Raman peaks associated with the dc, bc8, r8, hd and Si-XIII phases of Si. The primary peak of each phase is highlighted.

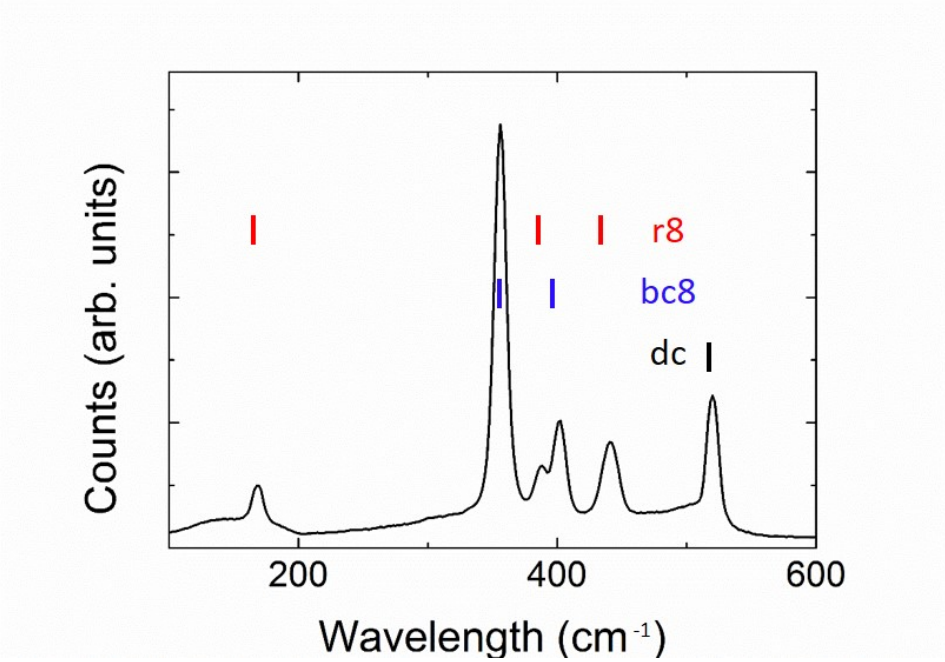

Fig. 3.6: Typical Raman spectra from an indent that has phase transformed to the bc8/r8 mixed structure. Characteristic peaks associated with both the bc8 and r8 phase have been indicated. The dc-Si peak is due to the surrounding and underlying dc-Si.

this thesis, only secondary electrons were used to form an image of the surface. Secondary electrons are low energy electrons that are emitted from the surface due to electron-electron interactions. As a result of their low energy, secondary electrons arise from near-surface interactions. Thus, detection of these secondary electrons can be used to create a topological map of the sample surface [176]. In this work, SEM imaging was used to measure the diameter of the circular phase transformed regions that were recovered after indentation. SEM was also used during focused ion beam (FIB) milling to help locate the region of interest as outlined below.

SEM images of the residual indents were taken using an FEI Helios 600 NanoLab dual-beam FIB system with an accelerating voltage of 3 kV.

3.5 Transmission Electron Microscopy

Transmission electron microscopy (TEM) involves directing a beam of highly energetic electrons through a sample [177]. The electrons interact with the sample in a variety of ways, producing signals that can be used for different measurements such as electron diffraction to give diffraction patterns or diffraction contrast for imaging. Other measurements include fluctuation electron microscopy [178] and electron-energy-loss spectroscopy [179] for monitoring

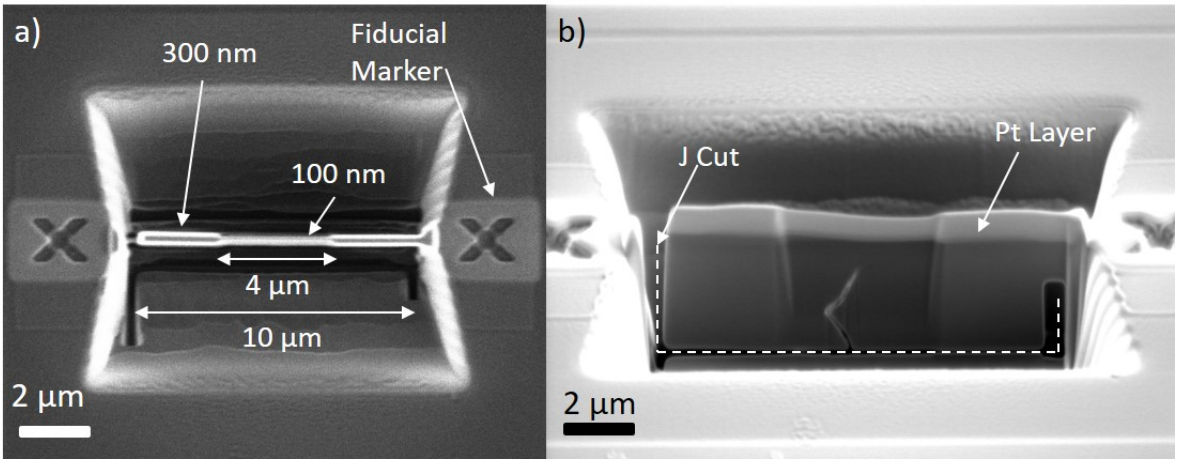

Fig. 3.7: SEM image of a FIB thinned lamella from (a) the top and (b) the side. The Si segment on the right is removed to disconnect the lamella from the underlying sample for pluck out.

amorphous structure and materials density, respectively, but these techniques are not used in this thesis. By using a sufficiently thinned sample, the dominant interaction will be elastic scattering/diffraction in accordance to Bragg's law. In this work, the samples will be measured by making use of the electrons scattered in this manner.

3.5.1 Sample Thinning: Focused Ion Beam

A FIB system was used to thin the cross-sections to electron transparency for XTEM imaging. A dual-beam FIB system, comprised of an electron beam column set at a 52° angle to a Ga^+ ion beam column, was used. Similar to SEM, the ion beam can be raster-scanned across the surface of the sample and the generated secondary electrons can be gathered to form an image of the surface. As the Ga^+ ions have far greater mass than incident electrons, they can deposit far more energy in collisions with atoms of the sample which gives rise to sputtering of the sample. Thus, a large amount of the sample can be milled away using the FIB system, leaving only a lamella thinned to electron transparency. That same interaction with atoms of the sample can also cause ion-implantation-induced damage to the surface of the sample. In Si, this can result in unwanted amorphisation of the surface [180]. To avoid this unwanted damage on the surface, a protective Pt layer is deposited over the region of interest before ion-beam milling. This is done by bombarding a Pt-filled precursor gas with ions to promote polymerisation of the Pt to form an adsorbed layer over the sample [181]. As the cross-section for polymerisation is dependent on the energy of the bombarding particle [182], a similar but slower process can also be performed using the electron beam.

Figure 3.7 shows a sample after undergoing the following FIB thinning process. First, the

residual indent is located using only the electron beam. Then, a 1 × 10 μm^2 thin layer of Pt is deposited onto the region of interest using the electron beam before any imaging with the ion beam is performed. With the surface protected, the system is tilted to 52° and the residual indent is located using the ion beam. A second, thicker protective layer of Pt is then deposited using the ion beam. This layer covers the same area as the first layer and is ∼1 μm in thickness. The sample on either side of the protected region is then milled away until only a 10 μm wide, 5 μm deep and 1 μm thick lamella remains. At this point, the sample is tilted to 7° (i.e. 45° relative to the ion beam) and a "J cut" is performed [as shown in Fig. 3.7(b)]. A J cut involves cutting the lamella free from the underlying sample along the bottom and partially free on the right. Thus, after the J cut, the lamella is attached to the surrounding sample only by a small region of material on the right. The sample is returned to a tilt of 52° and the lamella is further thinned to ∼300 nm thick. Due to the residual stress within the residual impression, final thinning was not done across the whole lamella to maintain stability. Instead, a smaller 4 μm window in the centre of the lamella was thinned until a final thickness of 100 - 200 nm was reached. This final thinning was done with an ion beam current of 93 pA which was found to produce minimal unwanted amorphisation of the sample surface. Any unwanted amorphisation that did exist did not cause any significant interference in the XTEM imaging. After thinning, the final connection to the underlying material is milled away to cut loose the lamella. The lamella is then lifted off the sample using a glass needle, attached to a micro-manipulator, and placed on a TEM grid in preparation for XTEM imaging. As several rough milling steps are automated, markers (fiducial) are present on either side of the lamella. These markers were used by the automated program to realign the sample after each milling step.

All the steps involved are presented in greater detail in Table 3.3. The dual-beam FIB used for this work was a FEI Helios 600 NanoLab dual-beam FIB system.

3.5.2 Sample Measurement: Cross-sectional TEM

Diffraction off the sample's crystal lattice results in a diffraction pattern characteristic of the sample. Figure 3.8(a) shows one such diffraction pattern taken from a dc-Si (large spots) with evidence of twinning (smaller spots in between). The central spot consists of the electrons that were not diffracted by the sample. Further, TEM is capable of producing high magnification images using individual spots taken from this diffraction pattern. A bright field (BF) image is created when only the central spot is used to form an image. The central spot consists primarily of undiffracted electrons. Thus, the contrast in the BF image is sensitive to changes in the diffraction cross-section across the sample and therefore changes in crystallite size, crystal structure, or orientation. In this work, cross-sectional TEM (XTEM) BF images of residual impressions recovered after indentation [such as that shown in Fig. 3.8(b)] were used to

Deposition	Area	Tilt	Current	Voltage	Thickness
Electron Beam Deposition	1 μm x 10 μm	52 °	1.2 nA	2 keV	~100 nm
Ion Beam Deposition	1 μm x 10 μm	N	0.46 pA	30 keV	1 μm
Milling	Area	Tilt	Current	Voltage	Depth
Distance from Pt	5 μm		9 nA		5 μm
	2 μm		2.8 nA		
	0 μm		0.93 nA		
J Cut	N/A	45 °	0.93 nA	30 keV	2 μm
Total Thickness	500 nm		0.48 nA		6 μm (inc. Pt)
	300 nm	±3 °	0.28 nA		
	100 nm		93 pA		

Table 3.3: The conditions for the steps involved in the preparation of XTEM samples. The tilt is given relative to the Ga^+ beam column.

image the depth of any phase transformed regions as well as give information on any crystalline defects that may be present in the surrounding material. In this image, the transformed region can be clearly differentiated from the surrounding dc-Si. Additionally, dark bands from bend contrast can also be observed in the surrounding dc-Si material. Residual stress present in the sample combined with reduced rigidity for a thinned sample can cause the sample to bend. Due to this bending, parts of the crystal across the sample can come into and out of satisfying the Bragg conditions. Thus, darker bands in the BF image are created. The bend contours are due to the interaction between the residual stress within the indents and do not represent any plastic deformation (such as crystalline defects) within the sample before thinning.

Secondly, an aperture may be inserted such that the diffraction pattern is formed from only a small, selected area admitted through said aperture. This selected-area diffraction pattern (SADP) is used to identify the crystal structure of the phases within the selected area. A SADP taken from the region circled in Fig. 3.8(b) is shown in Fig. 3.8(c). Unlike the diffraction pattern shown in Fig. 3.8(a), this SADP is dominated by reflections associated with the bc8/r8 structure found within the selected area. The distance between each reflection and the central, undiffracted beam is inversely proportional to the d-spacing of the crystal structure. Thus, the reflections form a unique signature that represent the presence of different crystalline structures. Diffuse rings can also be observed when the electron beam is diffracted through an amorphous structure.

Finally, an image may be formed using only a single diffracted reflection, which is known as a dark field (DF) image. In a DF image, only the structure from which the selected reflection

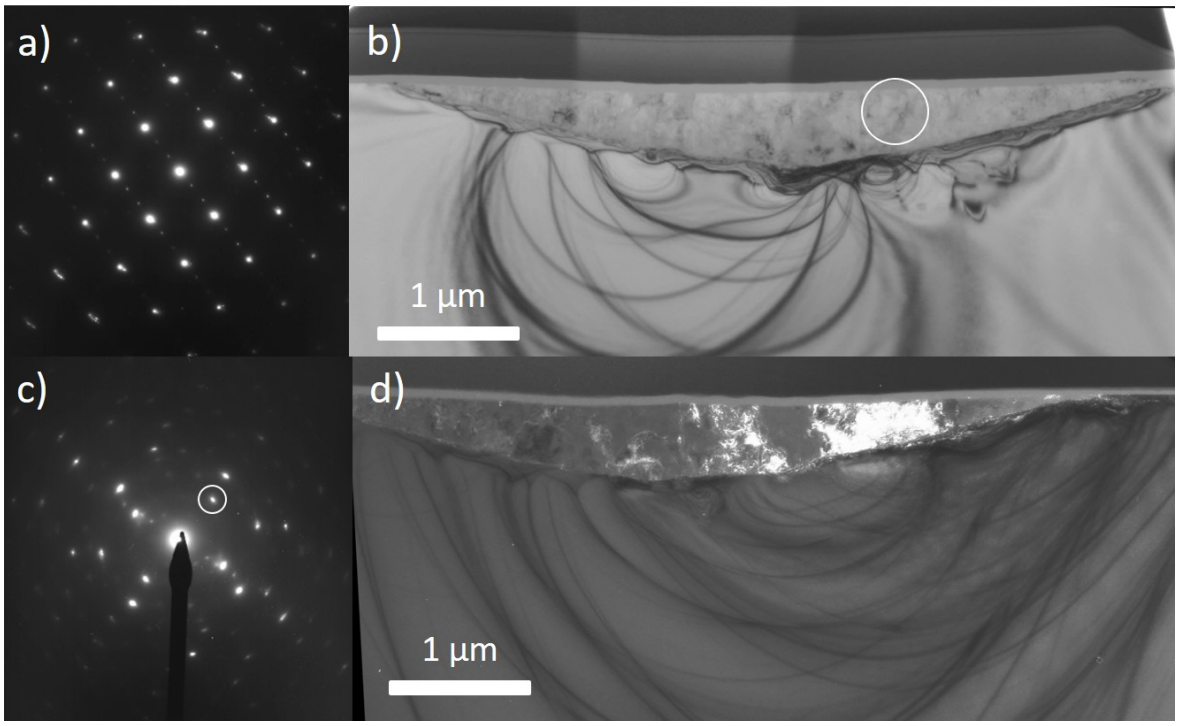

Fig. 3.8: (a) A diffraction pattern of dc-Si (with slight twinning) (b) A BF XTEM image of a phase transformed bc8/r8 region after indentation. (c) A SADP taken from the indicated region in (b) showing the presence of the bc8 and r8 phase. (d) DF XTEM taken from the reflection indicated in (c) showing the crystalline region from which the chosen reflection originates. The d-spacing of the selected reflection is 2.7 Å, which is associated with the [211] plane of bc8-Si. The dark bands observed below the phase transformed region in (b) and (d) are bend contours due to the sample bending under the residual stress present in the bc8/r8 mixed structure.

Phase	Space Group	Lattice Parameters	Atomic Position	Reference
dc-Si	*Fd-3m*	a = 5.4307 Å		[184]
bc8-Si	*Ia-3*	a = 6.636 Å	x = y = z = 0.1003	[32]
hd-Si	$P6_3/mmc$	a = 3.80 Å		[142]
		c = 6.28 Å		
r8-Si	*R-3:r*	a = 5.620 Å	x = 0.5, y = 0, z = 0.299	[30]
		γ = 110.07°	x = y = z = 0.25	

Table 3.4: The space groups and structural parameters of the Si phases present in this work.

originates is prominent within the image. Figure 3.8(d) shows a DF image taken using the bc8-Si spot circled in Fig. 3.8(c). Unlike the BF image, the majority of the DF image is dark with only the bc8-Si crystals that are associated with the selected reflection having a significant amount of intensity. DF XTEM images are useful for measuring the distribution of crystallites of a particular structure present in the SADP.

The reported space groups and structural parameters of the Si phases observed in this work are presented in Table 3.4. The *d*-spacing for the phases calculated, using these values, are presented in Table 3.5. The space group for r8-Si (*R-3*) can be defined using hexagonal parameters or rhombohedral parameters. In the literature, it has exclusively been defined using the rhombohedral parameters (*R-3:r*).

A Philips CM 300 running at 300 keV was used for all TEM images presented in this thesis. Standard DF and BF conditions were used [183].

3.6 X-ray Diffraction

X-ray diffraction (XRD) directs an incident beam of photons through a crystalline structure to produce a diffraction pattern that contains information about the crystal lattice properties [185]. While the electron-diffraction-based technique (SADP) is used as the primary method for sample characterisation within this thesis, XRD is also used within this work due to one key difference. Unlike in electron diffraction that measures only a selected area of a thinned sample, XRD can measure a larger representative volume. This is due to x-rays interacting more weakly with the sample than electrons (i.e. less energy loss), allowing them to penetrate through a bulk sample. Thinning is not required for the purposes of this particular technique. Therefore, XRD probes a much larger sample volume than electron diffraction, which is especially important for powder diffraction. The larger region probed ensures that many different orientations are

dc-Si		bc8-Si		hd-Si		r8-Si	
hkl	d-spacing (Å)	hkl	d-spacing (Å)	hkl	d-spacing (Å)	hkl	d-spacing
111	3.125	110	4.695	100	3.29	100	4.501
220	1.920	200	3.318	002	3.14	1-1-1	3.219
311	1.637	211	2.709	101	2.91	2-1-1	2.659
		220	2.346	102	2.27	20-1	2.638
		321	1.774	110	1.90	0-1-1	2.579
		400	1.659	103	1.77	2-1-2	2.050
				200	1.65	1-1-2	2.022
				112	1.63	3-2-1	1.741
						30-2	1.735
						3-10	1.718

Table 3.5: The d-spacing values of the Si phases, calculated using the values presented in Table 3.4.

measured, creating a more complete picture of the crystal lattice. Further, more reflections are also present in an XRD pattern compared to a SADP taken using TEM. Thus, the resulting intensities in XRD measurements can be used to determine values such as phase fraction of a particular phase within a mixed structure.

XRD images can be broadly categorised into two groups. These groups are single crystal samples and powdered samples. Diffraction from a crystal sample results in reflections that form a 2-dimensional lattice, while the reflections from a powdered sample forms rings. In this work, the bc8/r8 structure was treated as a powdered sample as the polycrystalline bc8/r8 mixed structure was better approximated as a powder than a single crystal. All XRD measurements were taken at the Advanced Photon Source (APS) at Argonne National Labs. The APS is a 3rd generation synchrotron x-ray source. A synchrotron is a particle accelerator that uses a magnetic field to guide electrons moving at close to the speed of light in a closed loop. As the electrons are accelerated (i.e. their direction is changed) by the magnetic field, photons are emitted tangentially with a relatively wide range of wavelengths. An insertion-device (ID), comprised of an array of alternating magnetic fields, is placed in the closed loop. Such devices guide the electron beam into a sinusoidal path which creates many tangential photon beams. These tangential beams positively interfere, producing a beam of monochromatic X-rays with a well-defined energy. It should also be noted that the produced beam is highly polarised in the plane of the closed loop.

Two different IDs were used for the XRD results presented. The HP-CAT 16-ID-B beamline

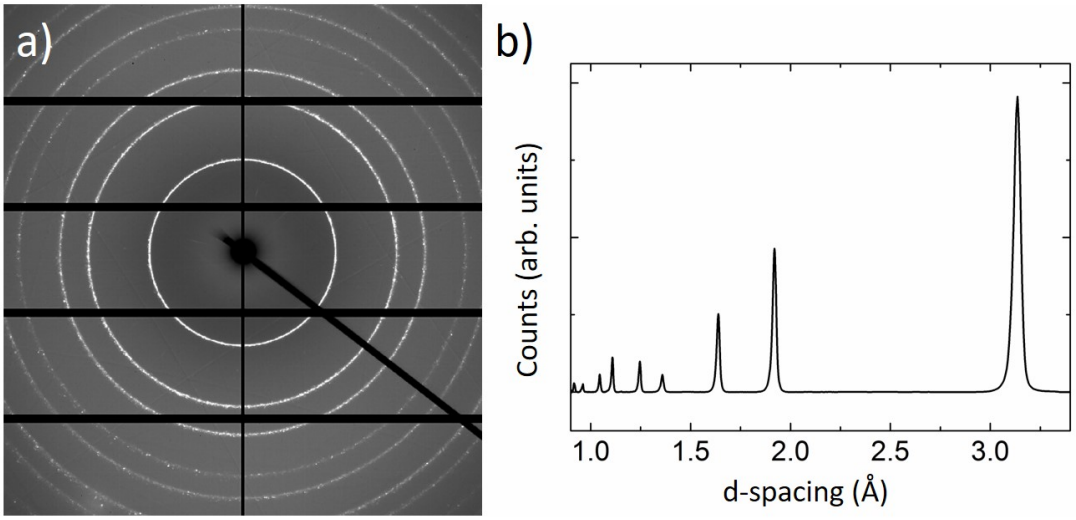

Fig. 3.9: XRD pattern taken from a powder dc-Si sample (a) before and (b) after integration via Dioptas [147]. The regions that are blanked on the detector and the beam stop are masked out and not included in the integration.

was used for the XRD data taken from the Si-XIII samples, and the 34-ID-E beamline was used to characterise the bc8/r8 structure. Figure. 3.9 shows an XRD pattern of powdered dc-Si and the same pattern after integration using the software package Dioptas [147]. The black lines present in Fig. 3.9(a) are due to the detector set-up and are masked before integration so that they do not interfere with the final result. These integrated patterns can be used for calculating the crystal structure of a phase or the ratio between two mixed phases via Rietveld refinement. Refinement was performed using the second version of Generalized Structure Analysis System (GSAS-II) [148].

3.6.1 Profile Fitting Software: GSAS-II

GSAS is a software package used for fitting crystal structures to integrated diffraction data to create XRD profiles such as the data shown in Fig. 3.9(b). The second edition of this program (GSAS-II) was used to perform Rietveld refinement in this work. Rietveld refinement is a technique developed for characterisation of powder diffraction data [186]. It uses a least squares refinement process to refine a calculated profile to an observed profile. The calculated profile is based on several parameters. Some parameters are related to experimental setup, while others are related to the crystal structure of the sample. The unit cell parameters required for this work are the space group, the unit cell, the atomic positions, and the phase fractions. Approximate values for these critical parameters are input into the program and refined to produce the best possible least squares fit to the observed data. A reduced χ^2 value (designated "goodness-of-fit" or GoF by the software) is used by GSAS-II to give a quantitative

measure of the fit between the observed and calculated profiles. For reference, the acceptable fits from the GSAS-II tutorials have GoF values between 3.44 and 5.63. Qualitative assessment of the fit is also heavily employed due to the unreliability of a single number encapsulating all the factors involved in a Rietveld refinement.

Rietveld refinement was used to calculate the phase fraction of the r8 phase in the bc8/r8 structure. It was further used to identify the peaks associated with the hd-Si phase in a hd-Si/Si-XIII mixed structure.

3.7 Spectrophotometry

A spectrophotometer measures the intensity of transmitted/reflected light as a function of wavelength. The transmitted/reflected intensity is commonly measured as a percentage of the incident light. The amount of incident light that is absorbed by the sample can also be measured by subtracting both the amount of reflected and transmitted light from the total incident light (i.e. A% = 1 - T% - R%).

There are three key components of the system used in this thesis that the incident light has to pass through. They are the lens, the integrating sphere (a sphere coated in a highly reflective material) and the detector. For transmission measurements, the sample is placed before the integrating sphere. The lens focuses the light onto the sample into a rectangular shape of $\sim$2 mm^2 area. For reflectance measurements, the sample is placed after the sphere and the lens focuses the light onto the sample into a circle also of $\sim$2 mm^2 area. The spectrophotometer was used to measure the absorption of the bc8/r8 mixed structure in this work. The regions of the bc8/r8 structure formed generally comprised of <10% of the $\sim$2 mm^2 spot size.

A PerkinElmer Lambda 1050 UV/Vis/NIR spectrophotometer equipped with an InGaAs detector was used.

Chapter 4

Properties of the bc8/r8 Mixed Structure

This chapter explores the nature of the bc8/r8 mixed structure. A process is presented that aims to quantify the respective phase fractions of bc8-Si and r8-Si in the indentation-induced mixed-phase structure. The ratio is calculated using X-ray diffraction (XRD) data that is analysed using Rietveld refinement. Using this ratio, the reflectance and transmission of the bc8/r8 structure is measured using a spectrophotometer, and the absorption coefficient is calculated.

4.1 Background

The r8-Si phase has been predicted to have desirable optical and electrical properties for photovoltaic (PV) applications [143, 144]. However, significant volumes of this phase have not been recovered after pressure removal within a diamond anvil cell (DAC). Thus, the presence of metastable r8-Si in the bc8/r8 mixed structure recovered after indentation is of significant technological interest. Further, the calculated properties reported by Malone *et al.* are for a phase-pure sample of r8-Si. This raises the question as to whether there is a sufficient amount of r8-Si within the mixed structure for these desirable properties to be both measurable and, if they are measurable, for the bc8/r8 mixed structure to be technologically viable.

The r8-Si Phase Fraction

A previous attempt to calculate the phase fraction of r8-Si within the bc8/r8 structure has been made using Raman microspectroscopy [41]. However, such Raman peak ratios are affected by differing scattering cross-sections between different phases [145] and the fact that the Raman cross-sections are not known for bc8-Si or r8-Si. An alternative technique that can be used to determine phase fractions is XRD, which is commonly used for characterisation of crystalline materials [187]. There are several reasons that such a measurement using XRD has not previously been reported. Most importantly, a significant volume of the bc8/r8 mixed structure is required in order to generate sufficient signal to allow for Rietveld refinement. The method used to overcome this issue in this work is presented below in Section 4.2.1. Even with sufficient signal, phase fraction refinement is non-trivial. This is due to the fact that XRD signals from

(nominally) phase-pure bc8-Si and phase-pure r8-Si are quite similar [30]. Moreover, the structural parameters for r8-Si at ambient pressure have not previously been reported. The following is a brief review of previous refinements of bc8-Si and r8-Si. It should be noted that the atom location parameters are the same for both bc8-Si and r8-Si (i.e. u, x, y, z) as established in Section 2.7.

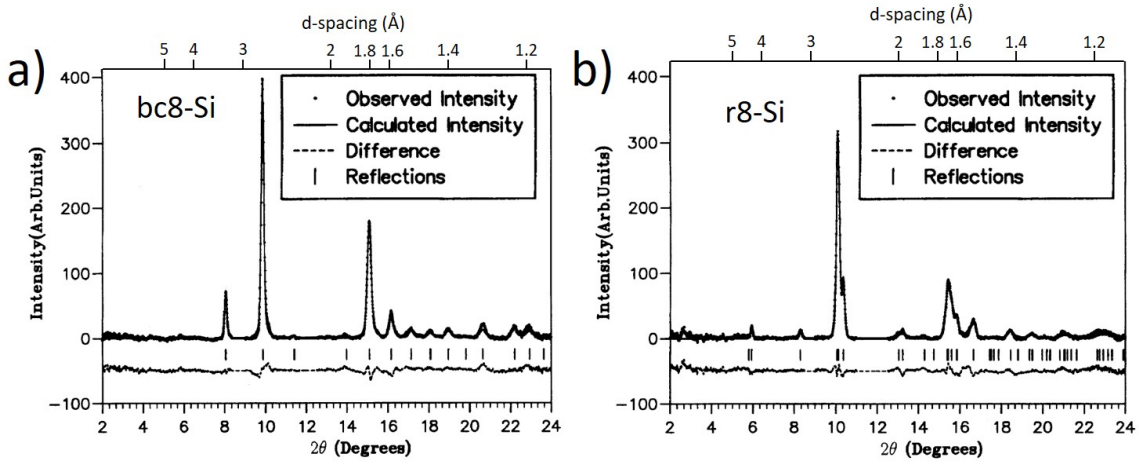

Fig. 4.1: Rietveld refinements of (a) bc8-Si at ambient and (b) r8-Si at 8.2 GPa. Figure adapted from Ref. [63]. The incident wavelength is 0.4652 Å. The *d*-spacings have been included above each plot to aid comparison.

Crain *et al.* were the first to report the presence of r8-Si during unloading within a DAC [63]. Figure 4.1 shows XRD profiles from bc8-Si and r8-Si adapted from Ref. [63]. The authors state that the profiles of bc8- and r8-Si are clearly related. In a further study, the same authors suggest that a prominent difference in the profiles is the splitting of the strong [211] and [321] bc8-Si peaks into doublets in the r8-Si profile with a 2:1 intensity ratio [30]. Piltz *et al.* further noted that, on top of the conventional *Ia-3* space group, bc8-Si can be described by the same *R-3* space group that is attributed to r8-Si (as mentioned in Section 2.7.1). That is, by converting the structural parameters of bc8-Si into this rhombohedral cell, a more direct comparison between bc8-Si and r8-Si was possible. The rhombohedral structure will be used for bc8-Si for the rest of this chapter to facilitate comparison between these two phases. The rhombohedral cell parameters at different pressures presented within Ref. [30, 63, 138] are shown in Table 4.1. There is a clear similarity between the reported values for bc8-Si (at ambient) in the first column, and the reported values for r8-Si (at 8.2 GPa) in the final column. Finally, Crain *et al.* noted that the unit cell parameters for both the bc8 and r8 phase were dependent on the applied pressure. From these trends the unit cell parameters at 2 GPa, the transition pressure at which bc8- and r8-Si are expected to be able to coexist, were extrapolated. (No such trends were reported for the atomic position parameters, hence the absence of extrapolated values for these parameters.) The unit cell parameter values of

Parameter	Kasper	Piltz	Piltz	Piltz	Piltz	Crain
Phase	bc8		bc8	r8	r8	
Pressure	Ambient		2 GPa	2 GPa	8.2 GPa	
a (Å)	5.747	5.748	**5.716**	**5.712**	5.620	5.609
α(°)	109.47	109.47	109.47	**109.99**	110.07	110.07
u	0.201	0.201			0.2922	0.2921
x	0.5	0.5			0.4597	0.4580
y	0	0			-0.0353	-0.0369
z	0.299	0.299			0.2645	0.2641

Table 4.1: The rhombohedral structural parameters of the bc8 and r8 phases from Ref. [30,63, 138]. The values for Kasper *et al.* have been converted from cubic parameters to rhombohedral parameters via the method presented in Ref. [30]. The values in bold are extrapolated by Piltz *et al.* using the Birch Murnaghan equation of state [188] with B_0 = 96 GPa for r8-Si, B_0 = 120 GPa for bc8-Si, and B_0' = 5 for both phases.

the two phases were in such close agreement that Piltz *et al.* concluded that the difference in cell volume is mostly due to the change in cell angle and not cell length. That is, the main difference between the bc8 and r8 phase at a pressure where both phases can coexist in a DAC is a change in unit cell angle of ∼0.5°. This explains the similarity in the XRD signal from bc8- and r8-Si.

The other reason for the absence of XRD studies reporting the phase fraction of r8-Si is the inability to recover phase-pure r8-Si at ambient pressure. Thus, no structural parameters have been reported for ambient pressure. Further, there is no consensus regarding the residual stress experienced by the bc8/r8 mixed structure. As a well-documented set of starting parameters for r8-Si at ambient is unavailable, the parameters for r8-Si have to be refined alongside the phase fractions, with initial parameters chosen from within the reported range shown in Table 4.1. In the current study, this was not found to affect the final result; the refined unit cell parameters for r8-Si were found to be independent of the initial parameters used.

Optical Properties of the bc8/r8 Mixed Structure

The electrical and optical properties of this bc8/r8 mixed structure have been the focus of limited studies. The bc8/r8 mix structure has been experimentally shown to have semiconducting properties [77]. THhe experimental study of electrical properties by Ruffell *et al.* was motivated by theoretical studies predicting that r8-Si may have useful properties for PV applications [143, 144, 189]. These properties include its smaller band-gap (relative to dc-Si) [189], greater absorption over the solar spectrum [143], and its usefulness in high-mobility appli-

cations [144]. In particular, r8-Si has been predicted to have an indirect band-gap of 0.24 eV [189]. This is in contrast to dc-Si which has an indirect band-gap of 1.12 eV. Thus, r8-Si can absorb photons in the 0.24 eV to 1.12 eV near to mid-infrared range that is not possible for dc-Si. Direct measurement of the optical properties of r8-Si is complicated by the presence of bc8-Si within the mixed structure. Thus, an experimental determination of the optical properties of r8-Si from the bc8/r8 mixed structure must first involve the subtraction of the contribution from bc8-Si. (It should be noted that such a subtraction is on interest for understanding the fundamental properties of r8-Si. However, from an technological applications perspective the optical properties of the bc8/r8 mixed structure may be of greater interest, as this structure is the one that has been formed experimentally.)

A recent study reports that bc8-Si is an ultra-narrow band-gap semiconductor with a band-gap of 30 meV [137]. Importantly, Zhang *et al.* present the optical transmittance and absorption coefficient (reported as one of the variables within a Tauc plot) of bc8-Si. Further, the optical absorption of a material of known thickness can be calculated given these two variables (transmittance and absorption coefficient) [190]. Thus, if a phase fraction of bc8-Si within the indent can be calculated in the first half of this chapter, the bc8-Si contribution to optical absorption of the bc8/r8 mixed structure can be determined. These calculations are discussed in greater detail in Section 4.3.3 below.

4.2 XRD Measurements to Determine the r8-Si Phase Fraction

4.2.1 Experimental Method

As was stated earlier (see Section 2.4), the bc8/r8 mixed structure formed using indentation is known to form in a similar manner from both a-Si and dc-Si starting materials. For the results in this present study, an a-Si precursor was chosen for the samples prepared for XRD measurements. This was done for two main reasons. Firstly, crystalline defects do not occur in a-Si, thus removing an added layer of complexity that may impact the final result. Secondly, the signal from the underlying substrate will also be collected in the XRD data set. An amorphous structure will appear as a broad ring while a crystalline structure will appear as discrete spots. This is important when a background image is removed to minimise the impact of the surrounding material. Removing an a-Si background image will not cause errors due to differences in rotation between the background and the image, as the broad rings from a-Si are rotationally homogeneous. This is an advantage that a crystalline substrate does not share. To form the a-Si precursor, a dc-Si sample was self-implanted with Si ions to form a 2 μm thick layer of a-Si, which was then relaxed by annealing at 450°C for 2 hours. This

step was performed as relaxed a-Si has been reported to phase transform more readily than as-implanted a-Si [113].

The relaxed a-Si was indented using a TI 950 Triboindenter fitted with a ~60 μm diameter spherical tip. A schematic of the sample is shown in Fig. 4.2 with the incident X-ray beam direction also indicated. Each indent was made to a maximum load of 750 mN, with a loading/unloading rate of 10 mN/s. These conditions have been previously reported to form the bc8/r8 mixed structure [55] and the presence of the mixed structure was confirmed using Raman microspectroscopy. Indents were made in an 80 x 10 array near the edge of the sample, with a 10 μm separation between each indent. As each residual impression was ~10 μm wide, this created a 800 μm x 100 μm area of the bc8/r8 structure that can be approximated as a "thin film" (which is indicated in blue in the schematic). As the a-Si phase transforms under indentation pressure in a manner similar to dc-Si, the thickness of the film can be approximated as ~500 nm [191]. The sample is then polished down along the edge perpendicular to the long edge of the bc8/r8 film (indicated in Fig. 4.2 as the polished edge). That is, from the perspective of the incident beam, the material behind the transformed film is removed to minimise the amount of a-Si within the measured region. The schematic also defines a co-ordinate system, with the x-axis running parallel to the beam direction and the z-axis running parallel to the indentation direction (out of the page in the top view).

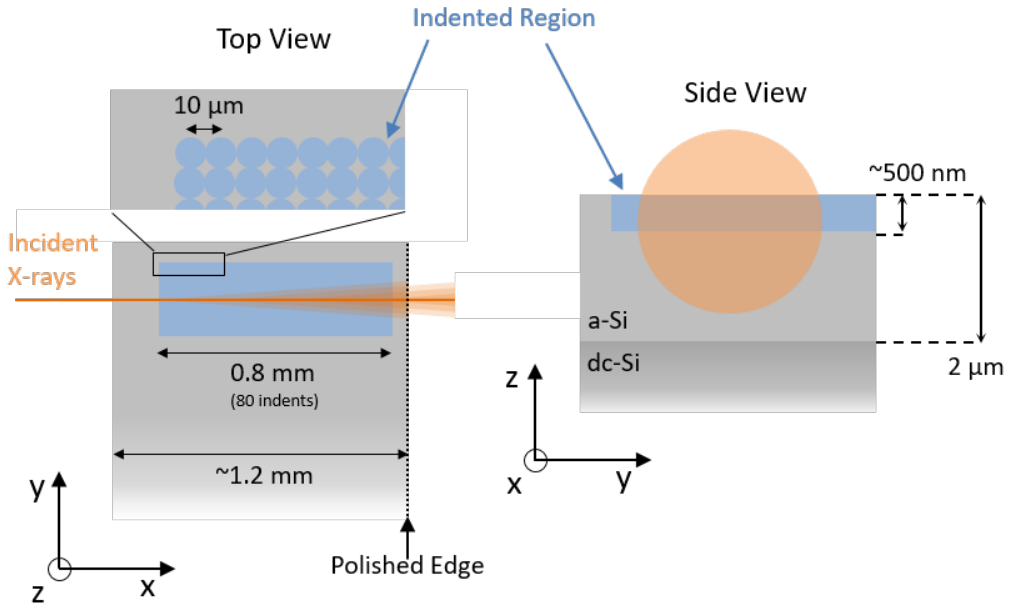

Fig. 4.2: A schematic of the bc8/r8 "thin film" samples used in this section for XRD measurements. The orange line/circle indicates the relative size of the X-ray beam, the blue region indicates the transformed bc8/r8 mixed structure, and the light grey region indicates the a-Si layer.

Figure 4.3(a) shows the load/unload curve from one the indents made into the a-Si. The presence of a pop-out event has been reported to be indicative of transformation to the bc8/r8 mixed structure. The pop-in events observed during loading are most likely due to plastic flow of the sample from under the indenter tip, as damage to the crystalline structure is not expected to occur due to the a-Si layer. Regardless of the cause of these pop-ins, they were not found to prevent phase transformation in subsequent indentations. The Raman spectra in Fig. 4.3(b) taken from the transformed region have prominent peaks associated to r8- and bc8-Si (such as the peaks at ~350 cm^{-1} and ~430 cm^{-1}), which confirms the presence of the bc8/r8 structure.

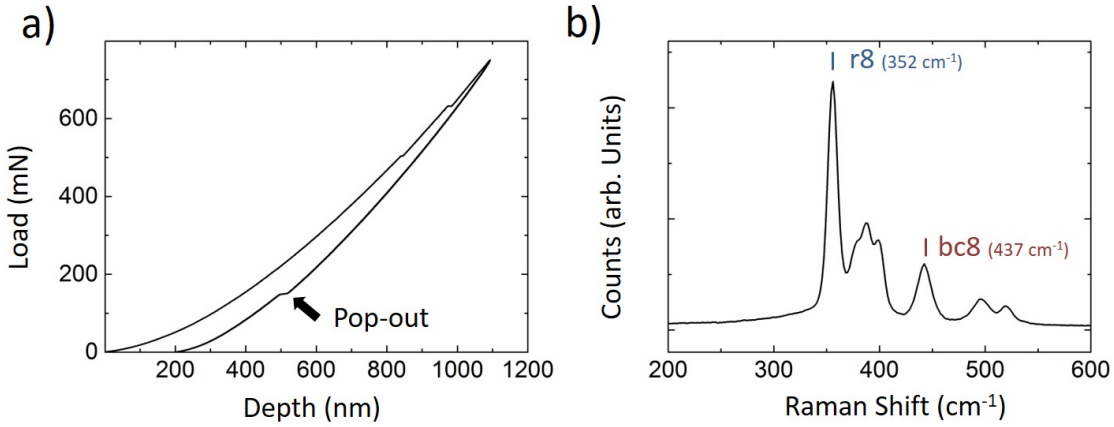

Fig. 4.3: (a) An indentation load/unload curve to 750 mN. The pop-out event that is generally associated with transformation to the bc8/r8 mixed structure is indicated. (b) Raman spectra taken from the transformed region. The main peaks associated with the bc8- (437 cm^{-1}) and r8-Si (352 cm^{-1}) phases are labelled.

XRD measurements on this sample were performed at the 34-ID-E beamline at the Advanced Photon Source (APS). The incident X-ray beam had an energy of 25 keV and a spot size of ~1 μm in diameter. Due to this small spot size, it was possible to graze the sample surface such that XRD data was collected only from the bc8/r8 film and the underlying a-Si.

The resulting XRD images were processed using the software package Dioptas [147]. Firstly, the background was removed by subtracting an a-Si image from the total image. That is, an image collected from purely a-Si can be removed from an image collected from both a-Si and the bc8/r8 structure to emphasise the bc8/r8 structure. Secondly, using the "cake" function, the images were converted from cylindrical coordinates to Cartesian coordinates. The advantage of this is that all reflections from a given lattice d-spacing will form a vertical line. This was used to determine if there was d-spacing variance within a ring of reflections. Finally, images were integrated to produce XRD profiles.

Rietveld refinement of the integrated data was performed using General Structure Analysis

System (GSAS-II) [148]. While many different parameters can be refined using GSAS-II, the parameters used within this work can be roughly divided into five types. First, experimental parameters are those that are unique to the experimental set up (e.g. Caglioti formula parameters U, V, W [192], sample thickness, crystallite size terms LX, GP, etc.) and primarily refine peak broadness. Second, unit cell parameters (e.g. unit cell length, unit cell angle) refine the position of the peaks. The final three all refine peak intensity. They are the atomic location (e.g. x, y, z, U_{iso}), preferred orientation (e.g. March-Dollase), and phase fraction parameters.

4.2.2 Results

Figure 4.4(a) shows an XRD image collected from the bc8/r8 thin film. As expected, three broad a-Si rings can be observed alongside several sharper "spotty" rings due to the bc8/r8 structure. Several features of this image require discussion. Firstly, the image is split vertically with the left hand side being brighter than the right hand side. This is most probably due to the incident beam travelling close to the surface of the sample. The brighter image on the left results from the photons that diffracted into the air while the image on the right results from the photons that diffracted into the sample. Secondly, there are two bright individual reflections, indicated by the white arrows in Fig. 4.4(b). These reflections appear symmetrical which suggests that they do not originate from a powdered source. The most likely explanation is that they are artefacts from a source that lies outside the focal plane, thus they were not included in the following integrations. Finally, the rings associated with the bc8/r8 structure are incomplete (spotty). This may be due to the grain size being too large or there are too few individual crystallites. That is, a statistically insufficient number of crystals are measured, thus classic powder rings are not produced [193, 194]. Another possibility is that the crystals have a preferred orientation. To minimise the effect on the intensity from the former, the brightest reflections are masked before integration. For the latter, the preferred orientation was flagged for refinement during Rietveld analysis.

An XRD image from the background a-Si was also collected. This a-Si image was subtracted from the image in Fig. 4.4(a) using Dioptas' background removal feature in order to emphasise the crystalline rings. The resulting image is shown in Fig. 4.4(b). Care was taken to ensure that no crystalline rings were accidentally removed in this step. A circle (green) drawn on this image has a d-spacing of $\sim$1.75 Å. Interestingly, close inspection of this shows that the rings in the XRD image are not circular and thus do not have a consistent d-spacing across all orientations. This elliptical nature is more clearly observed in Fig. 4.4(c) which shows the image in Fig. 4.4(a) after translation via the cake function mentioned in the experimental method above. The green line indicating a d-spacing of $\sim$1.75 Å has also been included. The curved nature of the sharper rings associated with the bc8/r8 structure confirms that they do not have a consistent d-spacing. In contrast, the broad rings associated with a-Si (dotted line)

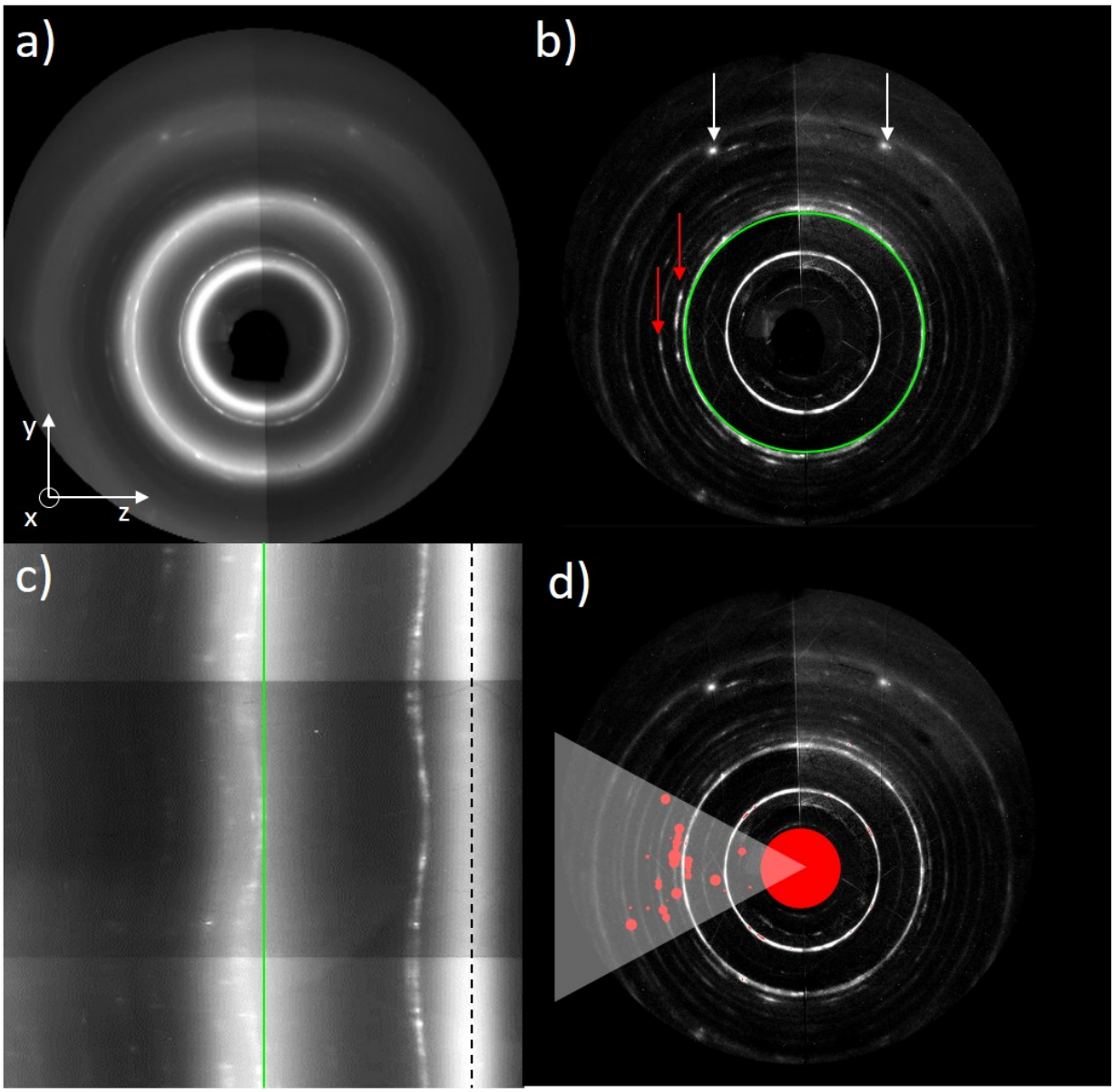

Fig. 4.4: (a) XRD image taken from the bc8/r8 thin film in the a-Si sample. The co-ordinate system from Fig. 4.2 has been included, indicating X-rays that have diffracted along the axis of indentation are diffracted horizontally. (b) The same XRD image with an a-Si background image removed to emphasis the crystalline rings associated with the bc8/r8 structure. A ring (green) to indicate a d-spacing of 1.75 Å and arrows (red) to indicate spots whose intensity is far brighter than the rest of the ring on which they lie. (c) The same image in Cartesian coordinates. The distorted crystalline rings (green line) can be clearly compared to the non-distorted a-Si rings (dotted line). (d) XRD image indicating the conical region (white) over which integration was performed to produce the profile in Fig. 4.5(a). The mask (red) used to remove the brightest spots is also included.

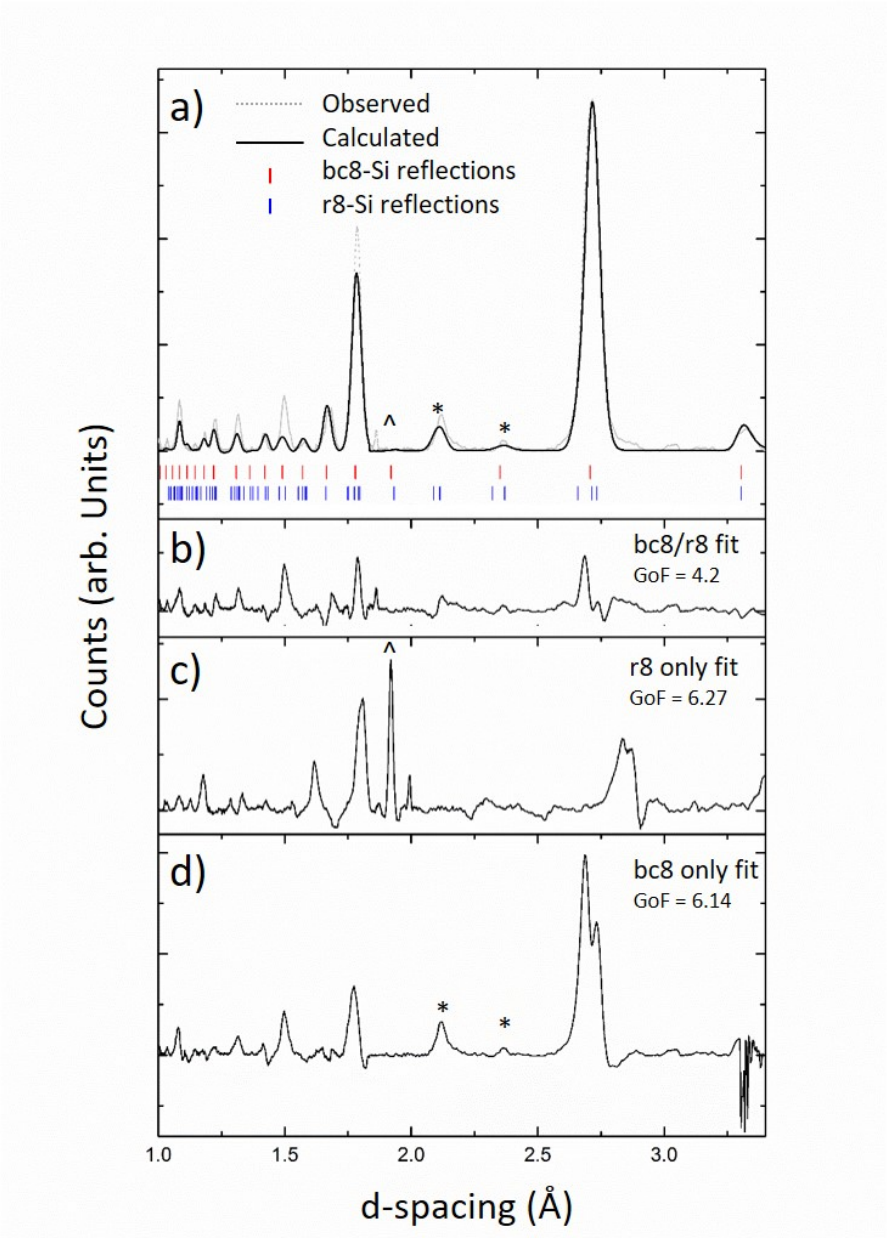

Fig. 4.5: A Rietveld refinement of the profile formed via integration over the conical region indicated in Fig. 4.4(d). The marks show the position of the allowed reflections for bc8-Si (red) and r8-Si (blue). (b) The difference between the observed and calculated profile shown in (a). The difference in profiles when only (c) bc8-Si or (d) r8-Si was used to fit the observed profile are also presented. The peaks which are not well accounted for by the refinements using only bc8-Si (*) or r8-Si (ˆ) are indicated. All plots have the same scale on the y-axis. The shape of the profiles are reversed compared to the ones reported by Ref. [63] shown previously as these are presented in d-spacing.

remain straight. This suggests that the distortion in d-spacing is confined to the indented region. A vertical elongation in the XRD image (i.e. reciprocal space) indicates a smaller d-spacing in the x-y plane of real space for the same [hkl] planes. That is, the unit cell of the bc8 and r8 phases have been distorted so that they are shorter along the plane of indentation and longer in the axis of indentation. This is a somewhat unsurprising result, given indentation is a uniaxial technique. It is possible that, as the β-Sn to bc8/r8 transformation occurs during decompression, uniaxial unloading generates a far greater pressure release in the z-axis. This generates a distorted unit cell that is elongated along the z-axis. Alternatively, the unit cell can be thought of as distorted by a shortening in the x-y plane. To determine which of these more accurately describes the transformation process requires a measurement of the unit cell length and this will be discussed later in Section 4.2.3. It is interesting to note that this unit cell distortion may be the source of the residual stress that allows r8-Si to remain even after complete pressure removal.

While the distortion of the bc8/r8 rings may be a key factor in the unique structures that are observed only in indentation, for the purposes of Rietveld refinement they cause peak broadening which can obscure detail. To compensate for this, sample integration was not performed on the entire XRD image but rather a smaller conical region (ranging from 20° to 60°). This was achieved by masking the entire image except for the chosen conical region. Furthermore, the brightest spots within the conical region were also masked for the reason mentioned above. [Note that, here brightest represents those that are disproportionately brighter than the rest of the ring. See, for example, the indicated spots in Fig. 4.4(b).] Several regions were integrated in this manner. One example of such a conical region is indicated by the white cone in Fig. 4.4(d). The mask used for masking the brightest spots within this region is indicated in red. Due to the spotty nature of the rings, a change in the chosen conical region or the spots masked may lead to a change in peak intensity (and thus calculated phase fraction). Therefore, several combinations of chosen regions and masks were integrated and refined to determine the level of variance introduced by these choices. Two selected profiles are presented in the section below as 'Approach A' and 'Approach B', each one representative of a different masking approach. Several general observations about the refinement that were consistent across all profiles will be addressed beforehand.

Firstly, it appears that the choice of initial unit cell parameters did not affect the final unit cell parameters. Both the unit cell values reported for bc8-Si at ambient and at 2 GPa were tested as the initial parameters (shown in Table 4.1). Similarly, the values reported for r8-Si at 2 GPa and at 8.2 GPa were also tested. Regardless of the initial parameters, the parameters would converge to the same values after refinement. However, these values could differ between approaches. Secondly, the atomic location parameters were not observed to make any significant difference. Piltz *et al.* [30] reported of their own work that, given the limited accuracy for peak intensity and the number of peaks observed, a re-evaluation of

the atomic location parameters reported by Kasper *et al.* [138] was not justified. A similar determination is made for the current data. Finally, the intensity correction for preferred orientation was refined using the March model modified by Dollase (March-Dollase preferred orientation) [195]. The [001] axis was chosen as the unique axis. This refinement was set up for the rod-like crystallite model. Intuitively, phase transformed regions may appear to be better described by a disk-like model, but the distorted unit cells as described above suggests the individual crystallites within the transformed region are better described by a rod-like model.

Approach A

The observed and calculated profiles of the region indicated in Fig. 4.4(d) is shown in Fig. 4.5(a). In this first approach to the refinement, a relatively wide conical region was chosen and only the brightest peaks have been masked. In this approach, refinement of the March-Dollase preferred orientation resulted in a non-trivial improvement to the fit. The position of the allowed reflections for both phases is indicated below the profile. Examination of the fit shows that, while all the observed peaks are present in the calculated profile, the intensity of the calculated profile differs from the observed profile at several key peaks. The difference is presented in Fig. 4.5(b). While a perfect fit has not been achieved with the current data, the difference can be said to be comparable with that of previously reported XRD profiles (for example, the refinements by Crain *et al.* presented in Fig. 4.1). The refined value for the r8-Si cell dimensions are a = 5.80 Å, α = 110.01°, while the bc8-Si dimensions are a = 5.77 Å in the rhombohedral cell. The r8-Si phase fraction for this refinement was ∼65%. These values (alongside select values from the literature) are presented in Table 4.2. Intriguingly, the unit cell length is substantially larger than the previously reported values. This was a reoccuring observation within several approaches and thus will be addressed in Section 4.2.3.

For reference, the GoF for this refinement is 4.2 (as previously mentioned, the acceptable refinements from the GSAS-II tutorials have a final GoF value in the 3.44 to 5.63 range). The difference in intensity between observed and calculated fits suggests that an improved refinement is possible. However, the fit could not be further improved via refinement of the atomic locations, preferred orientation, or phase fractions for this profile. Thus, a new approach (approach B) for profile masking and integration is needed from the initial XRD image. For this profile, the brighter peaks are masked more rigorously. Thus, only the most uniform sections of each ring are integrated into the profile. The results from refinement of this profile are presented in the following section.

Beforehand, as the phase-pure profiles of the bc8 and r8 phases are so similar (both to each other as well as to this integrated profile), it is necessary to first ensure that the data cannot be fitted using only bc8-Si or only r8-Si. The refinement process was repeated using only bc8-Si

or only r8-Si. The unit cell parameters were allowed to vary from the values reported above. The resulting difference profiles between the observed and calculated values are presented in Fig. 4.5(c) and (d). For the bc8-Si only fit, it is clear that several peaks have remained unaccounted for. For example, the peaks at ∼2.2 Å and ∼2.4 Å (indicated in Fig. 4.5 by the asterisks) are near identical in the observed profile and the difference profile. Indeed, the allowed reflections [shown in Fig. 4.5(a)] for bc8-Si do not calculate a peak at ∼2.2 Å. This observation is supported by the fact that no bc8-Si peaks were observed in this region by Crain *et al.* [as shown in Fig. 4.1(a)]. There is also a clear difference in intensity for the two most prominent peaks at ∼1.8 Å and ∼2.7 Å. This is unsurprising for a profile of the bc8/r8 mixed structure as the splitting of these peaks into doublets were reported to be a distinct difference between the, otherwise very similar, r8-Si and bc8-Si profiles [30]. For the r8-Si only fit, the presence of a peak at ∼1.9 Å (indicated in Fig. 4.5 by the caret) in the difference profile but not in the observed profile demonstrates the inability for the observed profile to be accounted for by a purely r8-Si refinement. The GoF values are 6.27 for r8-Si only and 6.14 for bc8-Si only, both considerably worse than the 4.2 value for a bc8/r8 mixed structure.

Approach B

In the second approach, the image was heavily masked before integration. The integrated profile from this approach is shown in Fig. 4.6. The region and mask are indicated in the inset. Previously, only the brightest reflections were masked. In this approach, far more reflections were masked until only the regions with roughly uniform intensity remained. As before, all peaks are present in the calculated profile. However, the difference in intensity is less apparent, suggesting a better refinement is achieved. It should also be noted that refinement of the preferred orientation did not appear to improve the fit, an unsurprising result as the spotty nature associated with preferred orientation has been masked over. Thus, this improved fit can be said to be only achieved via the loss of the information regarding texture within the bc8/r8 mixed structure. The refined value for the r8-Si cell dimensions are a = 5.84 Å, α = 110.08°, while the bc8-Si dimensions are a = 5.80 Å in the rhombohedral cell. The r8-Si phase fraction for this refinement was ∼80%. These values are also presented in Table 4.2. The GoF for this refinement is 3.5, supporting the suggestion that this refinement achieves a better fit than the previous approach.

Other Approaches

There is a significant difference between the refined values extracted from the first refinement compared to the second. This suggests there is a substantial amount of variance, possibly due to the different approaches taken. Therefore, several more refinements were performed (not

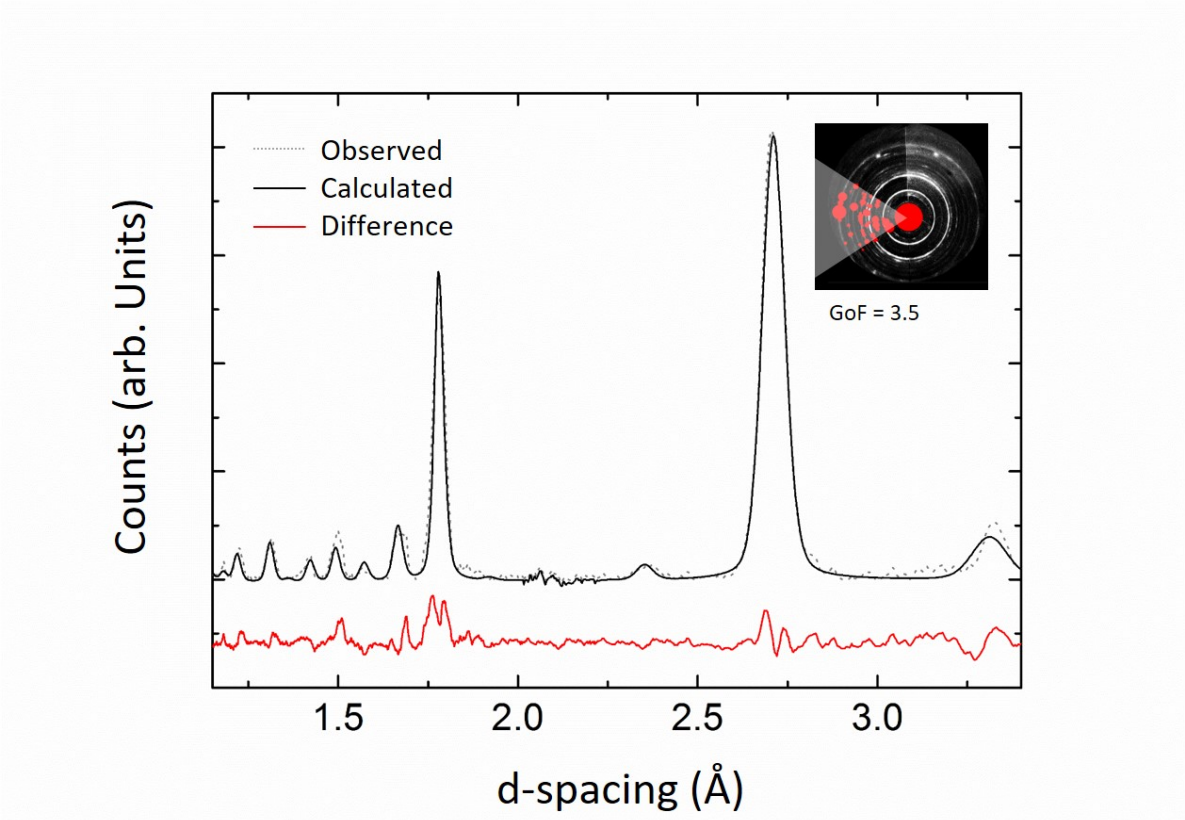

Fig. 4.6: Rietveld refinement of the XRD data produced by integrating over the heavily masked region indicated in the inset (Approach B). The difference between the observed and calculated profiles is also included.

shown) to establish a range within which these values lie. Only refinements with difference profiles similar to the ones already presented above and that had GoF values within 3.4 to 5.6 (the range from the tutorials) were accepted. The unit cell parameters for r8-Si were found to be $\alpha = 109.95 \pm 0.15°$ and a = 5.82±0.03 Å. The unit cell length for bc8-Si is a = 5.79±0.02 Å. The r8-Si phase fraction for this refinement was 70±10%. Apart from the loss of information regarding texture, the choice of mask did not appear to affect the extracted parameters in these additional refinements. In particular, the calculated phase fraction of r8-Si was not erroneously increased due to the more rigorous mask used in the second refinement above. These ranges are also presented in Table 4.2.

Within these additional refinement attempts, several general trends can be observed. Firstly, it can be noted that the two presented profiles were formed via integration of the left side of the XRD image (i.e. the side that diffracted through the air). Use of the right side (i.e. diffracted through the sample) gave refinements to which similar values could be extracted. This suggests that diffracting through the sample does not impact the result in a significant

	r8-Si (%)	GoF	a_{bc8} Cubic (Å)	a_{bc8} (Å)	a_{r8} (Å)	α_{r8} (°)
Refinement 1	65	4.2	6.67	5.77	5.80	110.01
Refinement 2	80	3.5	6.70	5.8	5.84	110.08
Overall	70±10	4.2±0.8	6.69±0.02	5.79±0.02	5.82±0.03	109.95±0.15
x-y plane			6.47	5.60	5.62	
Piltz - 0 GPa			6.64	5.748		
Piltz - 2 GPa			6.60	5.716*	5.712*	109.99*
Piltz - 8.2 GPa					5.620	110.07

Table 4.2: A table containing the r-Si phase fraction, GoF, and the unit cell parameters for r8-Si (a_{r8}, α_{r8}) and bc8-Si (a_{bc8}) found within this chapter and from Ref. [30]. Values for a_{bc8} have also been presented for the cubic lattice to aid discussion. Besides the row labelled x-y plane, all other measurements in this work are from the elongated z-axis. An * indicates values extrapolated by Piltz *et al.* from their experimental data using the Birch-Murnaghan equation of state.

manner. Attempts to refine a profile formed via integration of a vertical conical region did not produce acceptable fits. One proposal is that the combination of using signal from both sides may introduce too much complexity into the refinement. To minimise this effect, very narrow conical regions using only one side were attempted. However, these very narrow regions were found to be too dependent on local intensity variations (especially at higher d-spacings) to be considered reliable. Thus, unfortunately, no acceptable refinements were achieved for the sections of the image that represent the compressed x-y plane (i.e. vertical sections of the image) and no compressed unit cell parameters could be extracted. As the length of the unit cell of bc8-Si is the sole variable, it can be calculated from the d-spacing of a ring of known hkl value. Thus, a unit cell length of a = 5.60 Å in the compressed x-y plane can be estimated. A similar estimation can be performed for r8-Si if it is assumed that $\alpha = \sim 110°$ for all angles despite the unit cell distortion. A unit cell length of a = 5.62 Å is estimated for r8-Si in the compressed x-y plane.

4.2.3 Discussion

Table 4.2 shows the different unit cell parameters measured in this section. It is interesting to note that the unit cell lengths calculated along the z-axis in this chapter are significantly larger than those reported in the literature at 0 GPa. For example, there is a 0.13 Å increase in between the a_{r8} length extracted from the refinement in approach B and the length at 2 GPa reported in Ref. [30]. A similar decrease in length was only reported by Piltz *et al.* after compression was increased by 8 GPa. Further, the unit cell lengths calculated along the

x-y plane are significantly smaller than the reported values. This suggests that the unit cell distortion noted previously has indeed caused elongation of the unit cell along the z-axis but a shortening along the other two axes. Therefore, the residual stress that is present is best determined by considering the change in volume of the unit cell.

The crystallites within the bc8/r8 mixed structure are randomly orientated. Thus, the unit cell distortion (which lies along the sample axis, not a crystallite axis) results in many different distorted unit cell shapes. For ease of calculation, only the unit cell that is oriented parallel with the z-axis is considered. That is, the cubic lattice of bc8-Si in this orientation is effectively elongated into a tetragonal lattice and can be practically treated as such. This tetragonal lattice has a unit length of 6.67 Å along the z-axis and 6.46 Å along the x- and y-axis [1]. This gives an estimated volume of ∼280 $Å^3$ which is smaller than the volume of bc8-Si at ambient, ∼290 $Å^3$. The Birch-Murnaghan equation of state [188] was used to relate this change in volume to the respective change in pressure. For B_0 = 120 GPa, B_0' = 5 (from Ref. [30]), this results in a ∼4.5 GPa pressure difference. This suggests that the reduction in volume due to the residual stress experienced by the bc8-Si crystallites is equivalent compression to ∼4.5 GPa. A similar calculation can be performed for r8-Si, resulting in an volume of ∼140 $Å^3$. For B_0 = 96 GPa, B_0' = 5, and an initial volume of ∼142 $Å^3$ at 2 GPa (from Ref. [30]), a ∼2 GPa difference is calculated. This is equivalent to ∼4 GPa compression, which is similar to the value determined for bc8-Si. This suggests that, despite the elongation along the axis of indentation, the structure is under a residual stress that is roughly equivalent to a compression of ∼4 GPa. This proposal remains in agreement with the previous observation that this cell distortion may be the source of residual stress that allows a dominant fraction of r8-Si (observed in DAC studies from 2 to 9 GPa [63]) to remain on complete pressure unloading. It is suggested that bc8-Si is also present within the bc8/r8 structure with a residual stress of ∼4 GPa (observed in DAC studies at <2 GPa [30]) due to the uniaxial nature of the stress compared to the hydrostatic stress experienced in a DAC.

Interestingly, there is a considerable overlap between the ranges for the r8 and bc8 unit cell lengths. This similarity in length is in agreement with what had previously been suggested by Piltz *et al.* [30] from extrapolated data taken from DAC experiments; namely that, under the same pressure, the difference in volume between bc8-Si and r8-Si is almost entirely due to the difference in cell angle and not cell length.

An r8-Si phase fraction of 70±10% was calculated in this section. This demonstrates that r8-Si is the predominant phase in the bc8/r8 mixed structure. As the predominant phase, and if the optical absorption property of r8-Si is as significant as predicted [143], then this increase in absorption should be measurable via spectrophotometry. Such measurements are presented

[1] Note the conversion from the rhombohedral lattice parameter presented in Table 4.2 to the cubic lattice parameter

in the following section.

4.3 Optical Properties of the bc8/r8 Mixed Structure

4.3.1 Experimental Method

Double-side polished dc-Si wafers were used to produce the bc8/r8 mixed structure for optical measurements. A schematic of the sample is shown in Fig. 4.7 with the arrays (blue) and the spectrophotometer beam spot size (orange) indicated.

Arrays of indents were performed using a TI 950 Triboindenter fitted with a ∼60 μm diameter spherical tip. Each array consisted of 80 x 10 indents, with a 10 μm separation between each indent. The average depth of each indent is ∼500 nm, effectively creating a bc8/r8 "thin film" with a thickness of ∼500 nm. Each indent was made to a maximum load of 750 mN, with a loading/unloading rate of 10 mN/s as these conditions have been previously reported to form the bc8/r8 mixed structure [55]. Two samples were indented with arrays, one with a single array (800 indents) and another with two arrays (1600 indents).

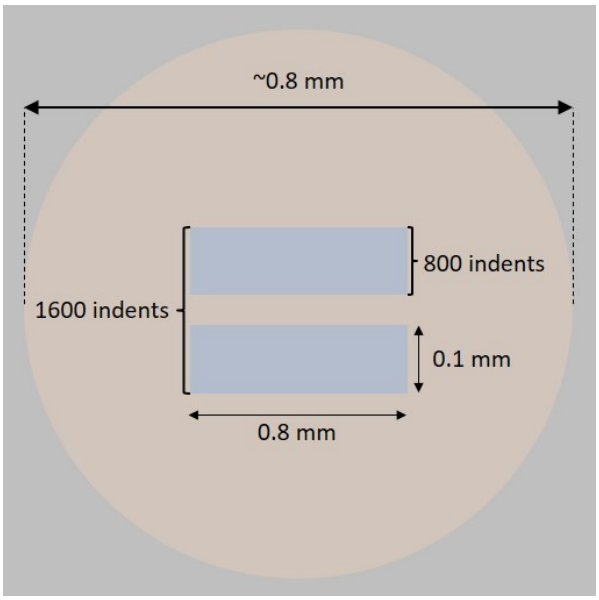

Fig. 4.7: A schematic of the bc8/r8 arrays for spectrophotometer measurements. The orange circle indicates the spectrophotometer spot size while the blue region indicates the array/s of indents that have formed the bc8/r8 mixed structure.

The optical absorption of the material was calculated by measuring the transmittance and reflectance of the indented region for the 900 nm - 1700 nm wavelength range using a spectrophotometer. An InGaAs detector with a gain of 0.15 and a response time of 0.80 s was used.

The presented spectra are the numerical averages of three separate collections. The system has a spot size of ∼2 mm^2. That is, the area of a single array is ∼5% of the total surface area measured by the spectrophotometer. After collecting the optical absorption spectra of the bc8/r8 mixed structure, annealing at 750°C was performed to transform the indented region to nanocrystalline (nc) dc-Si. The specifics of this transformation is presented in Chapter 6.

4.3.2 Results

Figure 4.8 shows the optical (a) transmittance and (b) reflectance of the sample indented with two arrays. This sample contained 1600 indents, covering ∼10% of the measured area. As a significant amount of the measured material is comprised of the surrounding dc-Si, spectra collected from an unindented dc-Si sample is presented alongside for reference. The absorption percentage (A) can be calculated from the percentage reflected (R) and transmitted (T) using $A = 1 - T - R$. The absorption for the samples is presented in Fig. 4.9. The inset presents a closer look at the 1120 nm - 1400 nm region of interest where the most significant difference from the unindented dc-Si is observed. There is a noticeable difference between the indented and unindented samples, with the difference increasing with the number of indents. This suggests that the reduced transmittance is due to the indentation process. There are two external factors that must be accounted for before the absorption from the bc8/r8 mixed structure can be determined.

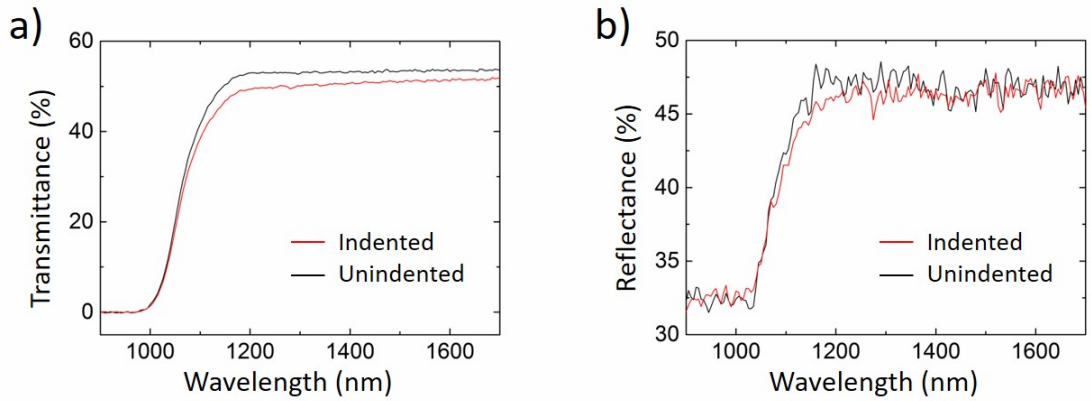

Fig. 4.8: Optical (a) transmittance and (b) reflectance of a sample with an array of 1600 overlapping indents. The spectra taken from an unindented dc-Si sample is also included for reference.

Firstly, the measured area is predominantly dc-Si. Thus, the measured response was normalised with respect to the amount of light that is incident upon the indents (as opposed to the surrounding dc-Si). Further, the underlying material is also dc-Si. Therefore, only sub-band-gap wavelengths (>1110 nm) were used for the determination of the absorption from

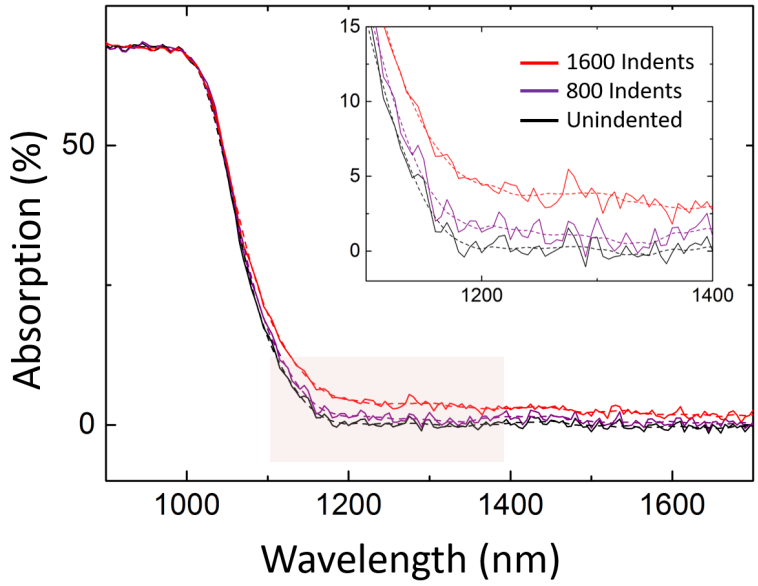

Fig. 4.9: Optical absorption spectra for a sample with an array of 1600 indents (red), 800 indents (dark red), and an unindented sample (black). The inset contains a closer view of the region highlighted in red. The dotted lines are the curves after smoothing and are presented as a guide for the eyes.

the indented region. From the inset in Fig. 4.9 it appears that, even within this sub-band-gap regime, dc-Si has a non-zero contribution to the absorption at wavelengths below 1200 nm. In order to isolate the contribution from the indented region, the spectrum collected from the unindented (purely dc-Si) sample was subtracted. Figure 4.10 presents the optical absorption spectra from the two samples (800 indents and 1600 indents) after normalisation and dc-Si spectra subtraction. It appears that both spectra collected from the two indented samples present a similar optical absorption spectrum. The absorption decreases with increasing wavelength (or decreasing photon energy). Across the measured range of wavelengths, the absorption rose from ~20% to ~60%. The error bars for the absorption spectrum collected from the sample with 800 indents (5±1% of the measured area is the indented material) is presented in the inset of Fig. 4.10. The sample with 1600 indents has similar error bars.

The second external factor to consider is that indentation does not solely transform dc-Si to a bc8/r8 mixed structure. The single crystal structure of the initial dc-Si has also been transformed. That is, the polycrystalline structure of the resulting bc8/r8 structure may also impact the optical properties. In addition, the original flat surface is transformed to a curved residual impression. The contribution to the difference in absorption due to these two changes was considered by comparing indented regions containing the bc8/r8 mixed structure

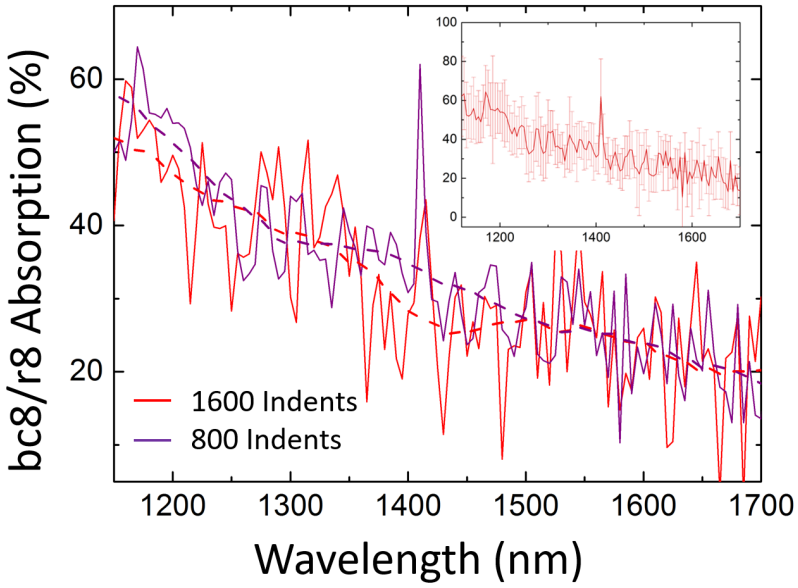

Fig. 4.10: Normalised optical absorption spectra of the bc8/r8 mixed structure. The contribution from the surrounding dc-Si material to the absorption spectra has been subtracted. The spectra are only plotted for wavelengths >1110 nm (i.e. above the band-gap of dc-Si). The dotted lines are the curves after smoothing and are presented as a guide for the eyes. (inset) The absorption spectrum collected from the sample with 800 indents with error bars.

to indented regions containing nc dc-Si. Figure 4.11(a) presents the difference in transmittance (Δ T) between and indented and unindented samples for both indented arrays containing nc dc-Si and the bc8/r8 structure. It should be noted that both samples are polycrystalline and neither surface is flat due to the presence of residual impressions after indentation. Within the region of interest, the transmittance does not appear to change due to the presence of nc dc-Si. That is, the transmittance appears to be the same between single crystal and polycrystalline dc-Si. Less of the incident light is transmitted through the indented region containing the bc8/r8 structure. This suggests that the decrease in transmittance observed is due to the bc8/r8 mixed structure and not the crystal size. The difference in reflectance (Δ T) is presented in Fig. 4.11(b). The reflectance of both samples decreases relative to the unindented sample. This suggests that the decrease is not due to the bc8/r8 mixed structure but due to other factors associated with indentation. One possible explanation is that the residual impressions cause surface texturing which results in a less reflective surface. This further suggests that the factors mentioned above (polycrystalline material and textured surface) that are found within all indented samples, both samples containing the bc8/r8 structure and samples containing nc dc-Si, contribute to the absorption. However, there is a significant increase in absorption that is uniquely due to the presence of the bc8/r8 mixed structure.

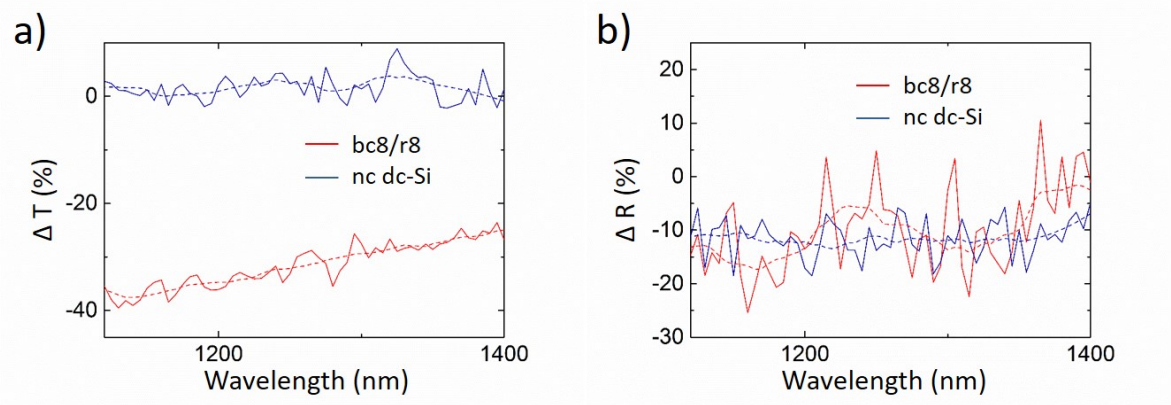

Fig. 4.11: Normalised optical (a) transmittance and (b) reflectance spectra of the bc8/r8 mixed structure compared to nc dc-Si. The contribution from the surrounding dc-Si material to the absorption spectra has been subtracted. The dotted lines are the curves after smoothing and are presented as a guide for the eyes.

4.3.3 Discussion

Absorption spectra collected from ~500 nm thick bc8/r8 thin films are presented (in Fig. 4.10). It was established earlier in this chapter (in Section 4.2.3) that 70±10% of the bc8/r8 mixed structure is r8-Si. Thus, an estimate of the absorption coefficient of r8-Si can be calculated by modelling the two phases using the law of mixtures [196, 197] which states that:

$$A_{bc8/r8} = A_{bc8}.V_{bc8} + A_{r8}.V_{r8} \tag{4.1}$$

where A_x is the absorption from material x and V_x is the volume fraction from material x. Furthermore, the absorption coefficient (α) is related to the absorption (A), reflectance (R), and film thickness (t) by the following equation [190]:

$$A = \frac{(1-R)\alpha t}{1-(1-\alpha t)R}. \tag{4.2}$$

Optical Absorption from bc8-Si

Firstly, the contribution to the absorption from the bc8-Si portion ($A_{bc8}.V_{bc8}$) can be determined from previously reported values. The optical transmittance and Tauc plot (comparing $((\alpha t.h\nu)^2$ against $h\nu$ where $h\nu$ is the photon energy) for bc8-Si in the 6 eV - 70 eV (17 μm - 203 μm wavelength) range is presented in Ref. [137]. From the Tauc plot, αt can be calculated as a function of energy for bc8-Si. As the transmittance is given in this report and $A = 1 - T - R$, R can also be calculated as a function of energy. Thus, an absorption for a sample of the

thickness used in Ref. [137] can be calculated by substituting αt and R values into Equation 4.2.

In a similar manner, the absorption (α) from the bc8-Si in this work can be calculated by reducing the value of αt proportionately to the difference in thickness (t) between these two works. However, insufficient information is presented to calculate a value for t in Ref. [137]. Therefore, an estimated thickness is required. The sample preparation for the sample probed by Zhang *et al.* was detailed separately in Ref. [136]. While the thickness is not reported in Ref. [136], the preparation method is similar to a separate study on Ge by the same group where the thickness was reported to be 2 mm [198]. Further, a sample of this thickness is consistent with the volumes commonly produced via multi-anvil cells [66, 199]. A thickness within the order of 1 - 2 mm is a reasonable estimate of thickness for this previous bc8-Si and the sample thickness in the current work is ∼600 - 1200 times thinner than in Ref. [137]. The resulting absorption due to a ∼150 nm thick bc8-Si film for a range of estimated sample thicknesses in Ref. [137] (1 - 2 mm) is shown in Fig. 4.12. The bc8-Si absorption saturates for photon energy values above 60 meV in all cases, with the worst case scenario saturating slightly above 6%. It should be noted that Zhang *et al.* present results at a far lower energy (higher wavelength) than the results presented in this chapter. Thus, it is reasonable to assume that the bc8-Si absorption has saturated across all photon energy values measured in the current work. This suggests that for the energy range measured in this work the contribution to the measured absorption from the bc8-Si in the bc8/r8 mixed structure can be estimated as ∼7% (at most) across all wavelengths.

Absorption Coefficient of r8-Si

By subtracting the contribution of the bc8-Si from the bc8/r8 absorption spectra, the absorption of the r8-Si portion (A_{r8}) can be calculated using Equation 4.1. The absorption coefficient (α_{r8}) can then be determined from this absorption value using Equation 4.2. Results are presented in Fig. 4.13(a). The error from the subtraction of the bc8-Si contribution to the absorption has not been included in the error bars presented in this figure. This is due to the need to estimate a thickness and based on the factor of 2 uncertainty in the thickness, consequently introduces a very large uncertainty in the absorption coefficient. In the most extreme case (where bc8-Si accounts for 100% of the absorption within the lower energy range), errors could be somewhat greater than the values in Fig. 4.13. This case was deemed unlikely, as it requires the sample measured by Ref. [137] to have a thickness of <1 μm. Figure 4.13(c) presents the calculated absorption coefficient plotted along with the predicted absorption coefficient reported by Malone *et al.* [143]. It is promising that the values reported from this chapter are an order of magnitude higher than the values predicted at the same photon energy given that the predicted values are for single crystal r8-Si. Note that in the diamond cubic

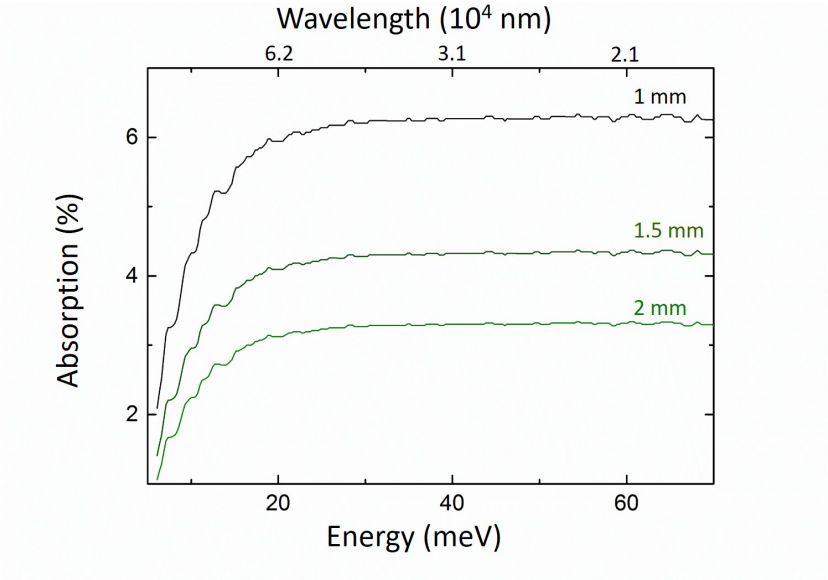

Fig. 4.12: The calculated optical absorption of the bc8-Si within the bc8/r8 mixed structure for different sample thicknesses. Values are based off the optical absorption data presented in Ref. [137] which did not report a sample thickness value. Thus, several possible absorption spectra are presented, each one corresponding to a different estimated thickness of the sample in Ref. [137].

case, polycrystalline dc-Si has a higher coefficient than single crystal dc-Si across a large range of photon energies [200]. Therefore, a similar situation may be true for r8-Si; the difference between the predicted values and the experimentally determined values presented here may be due to the polycrystalline nature of the samples used in this chapter. Interestingly, the slope of the experimentally determined absorption coefficient is similar to that of the predicted coefficient. In particular, it suggests that the absorption from r8-Si is not saturated. This result supports the suggestion by Malone *et al.* that r8-Si has a higher absorption coefficient than dc-Si in the <4 eV photon energy range.

Absorption Coefficient of the bc8/r8 Structure

While the absorption coefficient of r8-Si is of fundamental interest, the absorption coefficient of the bc8/r8 structure that is actually formed using indentation is of practical interest. Figure 4.13(b) presents the absorption coefficient of the mixed structure. This result is also presented alongside the result for r8-Si in Fig. 4.13(c). The absorption coefficient curve for the mixed structure has a more gradual slope compared to the r8-Si curve (i.e. it is higher at lower energies but lower at high energies). This suggests the bc8/r8 mixed structure may saturate at a lower photon energy than pure r8-Si, most certainly due to the presence of bc8-Si which is already saturated across the energies measured. However, the absorption appears to be similar

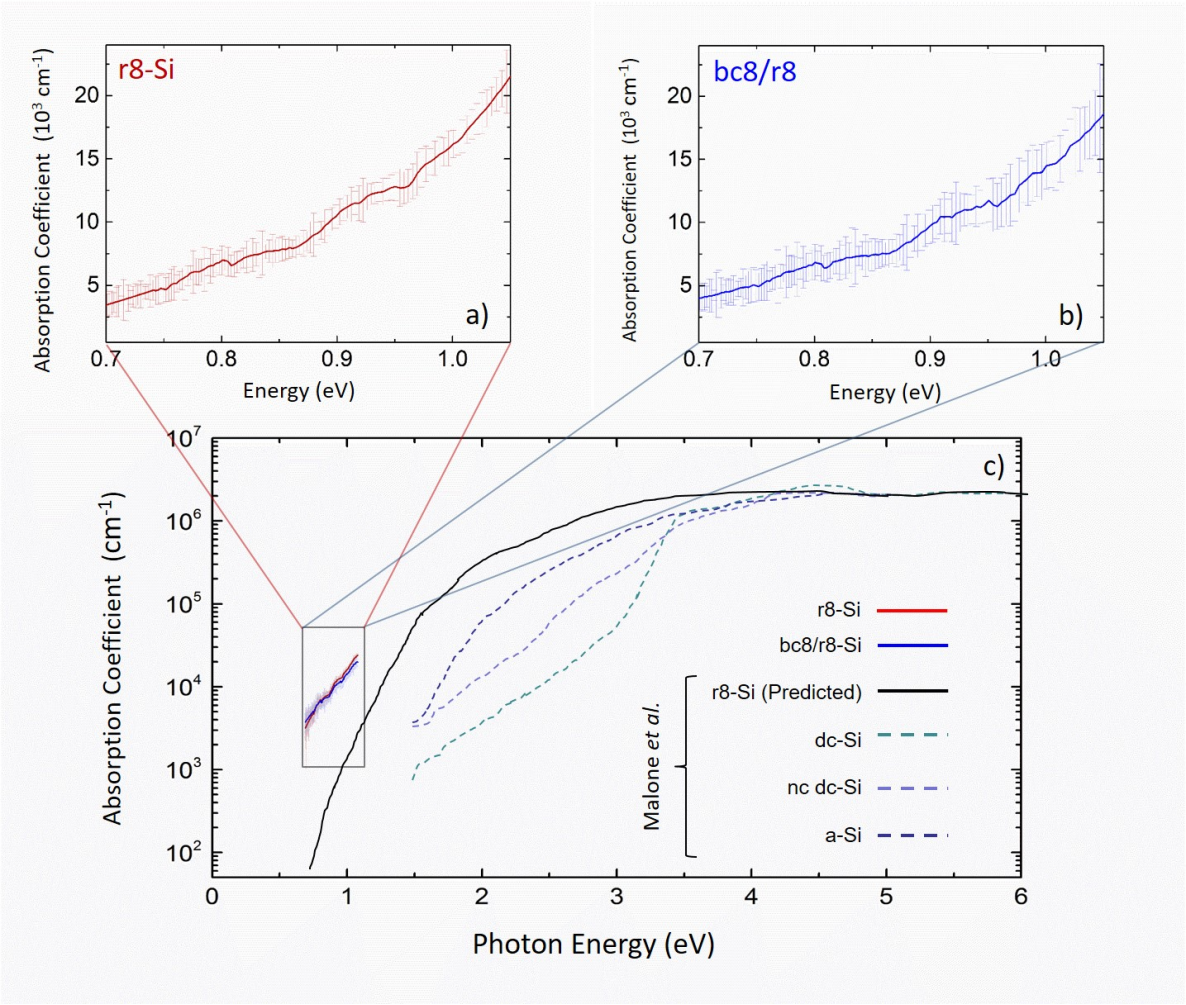

Fig. 4.13: The absorption coefficient for (a) r8-Si and (b) the bc8/r8 mixed structure calculated from the results presented in this chapter. (c) The values from this work have been inserted into a figure adapted from Ref. [143] that shows the values calculated via DFT.

for both within the measured energy range. This suggests that the bc8/r8 mixed structure has potential for PV applications even if the bc8-Si portion is not removed.

4.4 Summary

In this chapter, Rietveld analysis of XRD data taken from the bc8/r8 mixed structure formed via indentation has been performed. This analysis confirms the presence of r8-Si after complete pressure removal. In addition, it suggests that the r8 phase is the majority phase in the bc8/r8 structure, compromising ~60 - 80% of the mixed structure. It has also been shown that the unit cell of both the bc8 and r8 phase are elongated in the axis of indentation and it is suggested

that this is due to the uniaxial pressure release during indentation unloading. It is proposed that this cell distortion may be a source of residual stress that allows r8-Si to remain stable at ambient pressure.

Optical measurements were also performed on this predominantly r8-Si mixed structure. The absorption coefficient of r8-Si is calculated in the 0.7 eV - 1.12 eV range. The value reported in this work is higher than the value calculated using DFT within this range but had a similar slope with respect to varying photon energy. In addition, the absorption coefficient of the bc8/r8 mixed structure is also shown to have a similar absorption to pure r8-Si. This suggests that the increased absorption of r8-Si can be utilised even if it is not isolated from the bc8-Si portion of the bc8/r8 mixed structure.

Chapter 5

Two Pathways of Plastic Deformation

This chapter explores the deformation pathways of dc-Si under indentation pressure. The two dominant modes of plastic deformation are phase transformation and the nucleation and propagation of crystalline defects. The presence of these deformations under different indentation conditions is characterised using Raman microspectroscopy and cross-sectional transmission electron microscopy (XTEM).

5.1 Introduction

In most indentation studies of Si phase transformation, the phase transformed region is accompanied by damage in the surrounding crystalline material [39–41, 92, 93, 96] which is referred to in this chapter as "crystalline defects". A recent study has shown that it is possible to produce phase transformation as the sole form of plastic deformation without defects in the surrounding dc-Si [55]. Intriguingly, it was also shown that this phase transformed region was larger than the transformed region formed using a higher load when both phase transformation and crystalline defects were observed. That is, a higher load produced less phase transformed material under identical loading/unloading rates. This behaviour is shown in Fig. 5.1 adapted from earlier work by the author [55]. In this earlier work, it is suggested that this counter-intuitive result is due to two factors. The first is the nucleation limited nature of the initial dc-Si to (β-Sn)-Si transformation [32, 59–61]. Indeed, Pharr *et al.* suggests that several minutes above 11 GPa (the critical pressure for phase transformation [24]) may be necessary for the transformation to take place completely [61]. Such sluggishness of the phase transformation cannot alone account for the results in Fig. 5.1.

This result is only possible if a second factor is considered; namely, the nucleation and propagation of crystalline defects acts as a competing deformation process under compression. This earlier work proposes that, for the deformation process presented in Fig. 5.1(b), nucleation of crystalline defects occurred first which partially releases the indentation-induced pressure during the loading process. Subsequent loading increases the pressure until sufficient additional pressure is present to nucleate a second mode of deformation, phase transformation. This is in contrast to the case presented in Fig. 5.1(a) where no crystalline defects are present. In

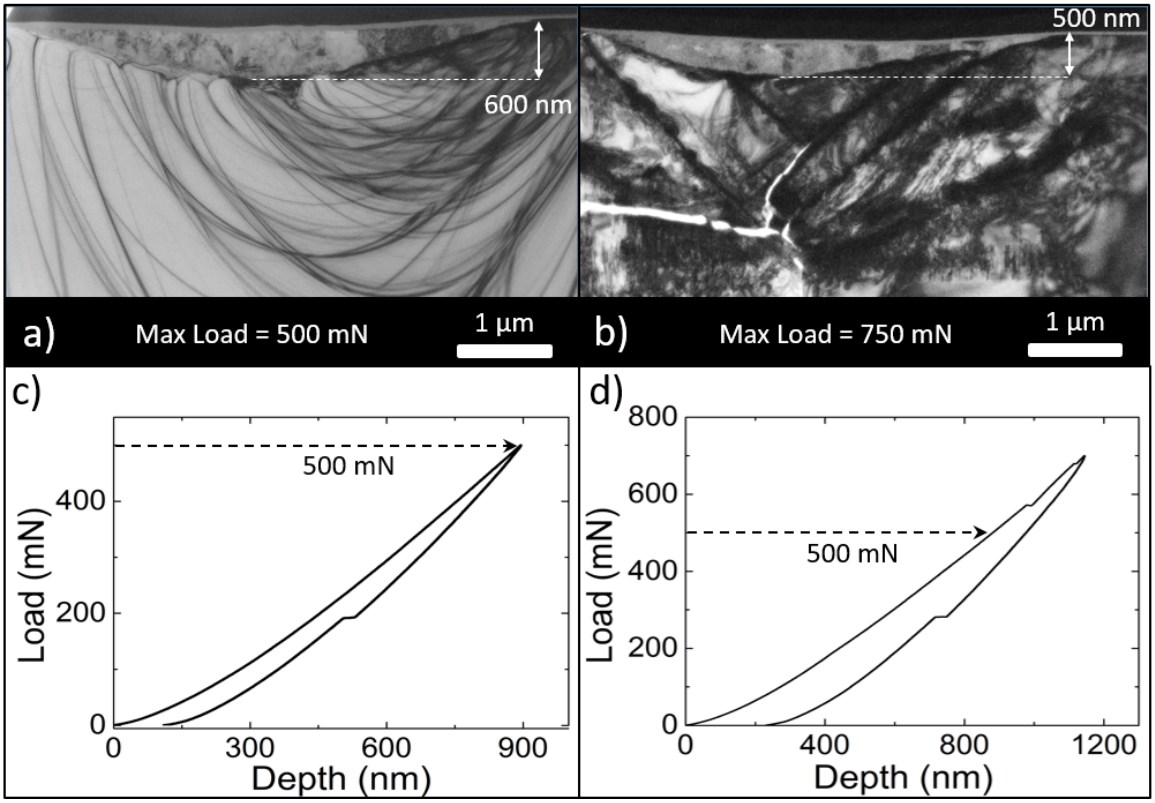

Fig. 5.1: XTEM image of a transformed region after indentation to a maximum load of (a) 500 mN and (b) 750 mN adapted from Ref. [55]. The load/unload curves for the (c) 500 mN and (d) 750 mN indents are also presented. At the point indicated by the dotted arrow, both samples have experienced identical indentation loading to 500 mN at 10 mN/s.

this case, phase transformation is the first and only mode of deformation. The entirety of the indentation-induced pressure (energy) is expended to cause phase transformation in the sample. Thus, a larger phase transformed region is possible even at a lower load.

This above result raises questions regarding incipient plasticity. That is, which deformation mechanism occurs first? There is a lack of consensus within the literature regarding the incipient plasticity of dc-Si under indentation pressure. Some studies report that the nucleation and propagation of crystalline defects occurs first [201,202], while others claim that it is phase transformation that occurs first [101]. This is further complicated by the fact that phase transformation and defect nucleation are primarily driven by different factors: hydrostatic pressure [54,101] and shear stress [39,50], respectively. Thus, incipient plasticity is dependent on the pressure distribution which is determined largely by indenter tip shape.

This chapter presents new results from indentation experiments performed for the current study that include a hold duration at the maximum load and the impact of this hold duration on the elastic/plastic response of dc-Si is investigated. Following this, hold durations are used

to explore indentation of dc-Si near the critical pressures required for plastic deformation (both phase transformation and defect nucleation). Finally, results showing the impact of incipient plasticity at higher loads, particularly on the shape and size of the transformed region, is presented.

5.2 Experimental Details

Indentations were made using a TI 950 Hysitron Triboindenter fitted with a 22 μm diameter spherical tip. This is the same tip as the one used in Ref. [55] where the diameter of the tip and the tip shape were obtained experimentally using SEM imaging. The tip was loaded into the sample at 10 mN.s^{-1}, held at the maximum load for a duration between 0 - 60 minutes and then unloaded at a rate of 10 mN.s^{-1}. Maximum load forces varied from 200 mN - 750 mN [1]. It has been previously suggested that tip asymmetry may lead to the metallic β-Sn phase flowing out from below the tip [39,55], thus it is necessary to note that the tip used was sufficiently symmetrical to prevent such an event from occurring.

Several methods were used to characterise the type of plastic deformation that occurred (if any). Initially, Raman spectroscopy was used as a quick, non-destructive method of determining the presence of phase transformation or crystalline defects. Following this, XTEM was used to image the plastically deformed region. Finally, SADP was used to confirm the presence of the bc8/r8 mixed structure within any transformed regions observed in XTEM.

The analytical program Elastica® [146] was used to simulate the hydrostatic pressure and shear stress experienced by the sample under indentation within the elastic regime. In particular, calculation of the pressure distribution at the point of incipient plasticity was performed.

5.3 Results

5.3.1 Hold Durations

Figure 5.2(a) shows a simulated hydrostatic pressure distribution from indentation using a 22 μm diameter spherical tip to a maximum load of 300 mN. A circular region with a radius of $\sim$2 μm experiences pressure greater than the critical transformation pressure of 11 GPa [24], with a maximum pressure of $\sim$15 GPa at the centre. This suggests that plastic deformation via phase transformation is expected during indentation at these conditions. Figure 5.2(b) presents the measured load/unload curve after indentation to a maximum load of 300 mN

[1] Due to software limitations, the number of depth measurements per second for the longer indents was reduced from 200 (Hysitron standard) to 20 measurements per second. This is not expected to have any affect on the result.

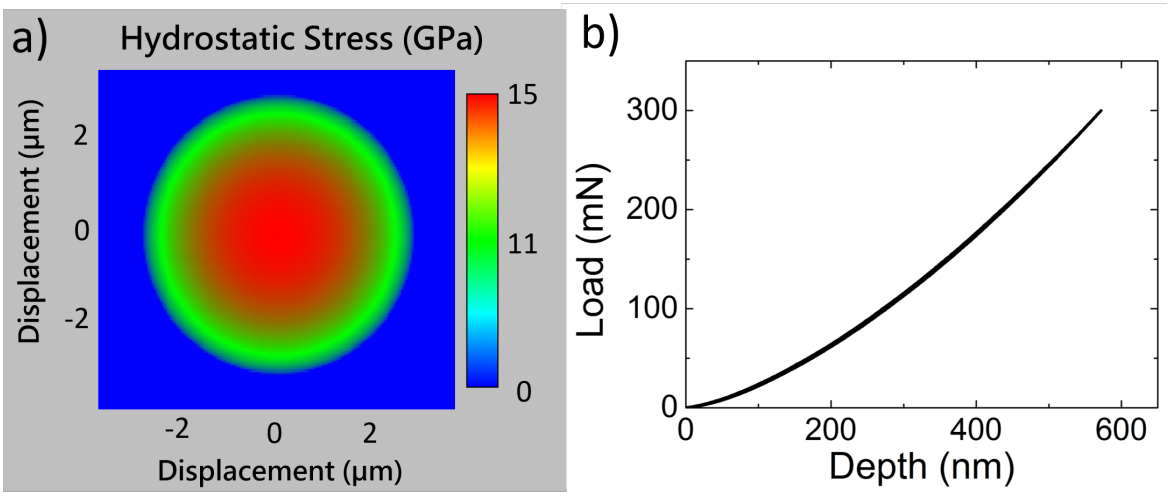

Fig. 5.2: (a) Simulated hydrostatic pressure experienced by dc-Si responding purely elastically under 300 mN nanoindentation load. The maximum experienced pressure is 15 GPa and a 2 μm radius circular region experiences >11 GPa pressure. (b) The measured load/unload curve after indentation to a maximum load of 300 mN. The load and unload curve are completely overlaid due to the elastic nature of the indentation.

using a 22 μm tip. The load and unload sections of the curve are completely overlapped, with a residual depth of 0 nm after complete pressure unloading. This indicates the sample has responded elastically to this indentation process and no residual depression remains after removal of pressure. This elastic response was confirmed using optical microscopy and SEM where no residual impression was found (not shown). This remained true for all 100 indents with a 10 x 10 array. Surprisingly, in contrast to what was expected from the calculated pressure distribution, no plastic deformation is observed.

Figure 5.3 shows optical images of the arrays made via indentation to 300 mN after a hold duration of (a) 1, (b) 2, (c) 3 and (d) 15 minutes was introduced at the maximum load. The 1, 2 and 3 minute arrays are 10 x 10 indents while the 15 minute array is only a 5 x 10 array due to time considerations. This figure shows that some residual impressions are now present after indentation. That is, the addition of a hold duration has generated plastic responses at a maximum load of 300 mN. This is in contrast to indentation to the same maximum load with no hold duration where only elastic responses were observed. This experiment was then performed across a range of maximum loads (200 mN - 300 mN) and hold durations (1 min - 15 min). The indentation conditions for these and their respective percentage of plastic/elastic responses are listed in Table 5.1. Several maximum load/hold duration conditions were repeated to increase statistical accuracy. In general, an increase in maximum load and/or hold duration resulted in an increase in the number of indents that responded plastically to indentation.

The residual impressions left by plastically deformed indents can be categorised into two sets

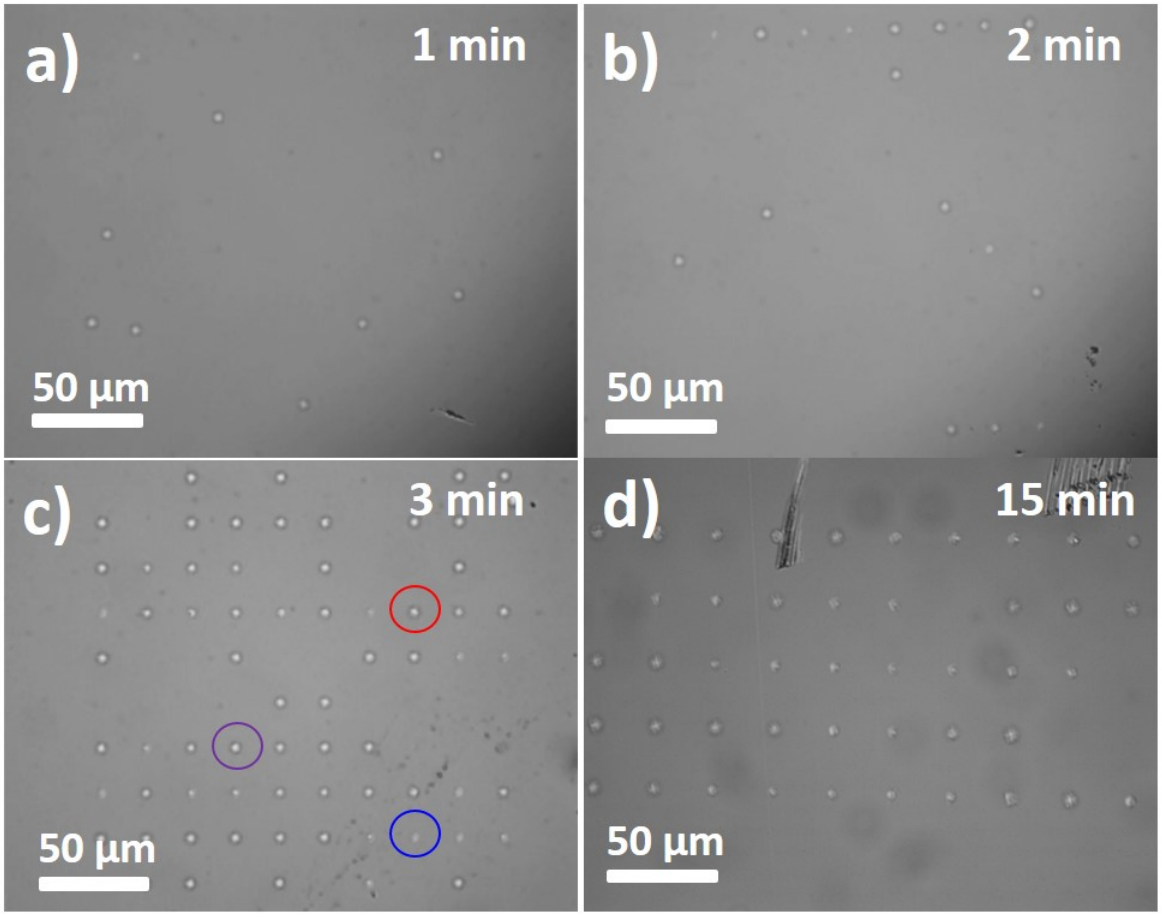

Fig. 5.3: Optical microscope image of arrays of 300 mN maximum load indents held at maximum load for (a) 1 min, (b) 2 min, (c) 3 min and (d) 15 min showing the increase in plastic deformation with increasing hold duration. The arrays in (a) - (c) are 10 x 10 arrays. The array in (d) is a 10 x 5 array. An array held at maximum load for 0 min (no hold duration) is not shown due to all indents responding elastically. Representative indents for the set of optically blurred indents (blue) and optically sharp indents (red and purple) are indicated.

Maximum Load	Hold Duration	Plastic	Elastic
300 mN	1 min	10%	90%
300 mN	2 min	18%	82%
300 mN	3 min	58%	42%
300 mN	15 min	92%	8%
275 mN	15 min	46%	54%
250 mN	15 min	46%	54%
225 mN	15 min	7%	93%
200 mN	15 min	4%	96%
200 mN*	60 min	0%	100%

Table 5.1: The percentage of plastic/elastic responses under different maximum loads and different hold durations at maximum load. *Only five indents were performed at 200 mN with a 60 minute hold duration. Thus, this result may not be statistically representative.

in the optical images shown in Fig. 5.3. A representative of the first set is circled in blue while representatives of the second set are circled in red and purple in Fig. 5.3(c). One set (red and purple) appears to have a "sharp" outline while the other *blue) appears to have a more "blurred" outline within the presented images. This suggests that there may be two distinct plastic deformation mechanisms present within the indents that are observed in Fig. 5.3. It should be noted that a change in optical focus will bring the "blurred" set into focus (i.e. "sharp") and vice versa. To help differentiate them, the two sets will be denoted as the "sharp" set and the "blurred" set despite these properties only being due to the specific choice of optical focus in Fig. 5.3.

Figure 5.4 shows several load/unload curves from indents that fall within the two optically-distinct sets. Several discontinuity events are observed within these curves. These events are associated with different plastic deformation mechanisms, as previously established in Section 3.1. Figure 5.4(a) shows the curve from the indent circled in blue in Fig. 5.3(c) which belongs to the "blurred" set of indents. This load/unload curve contains a distinct pop-out event which is indicative of phase transformation from (β-Sn)-Si to the bc8/r8 mixed structure. There is no discontinuity event in the loading curve, suggesting the initial dc-Si to (β-Sn)-Si transformation is a gradual process. This transformation occurred at such a slow rate that no change in slope or pop-in event is evident during loading or during the hold duration. Figure 5.4(b) shows a load/unload curve from the indent circled in red in Fig. 5.3(c) which belongs to the "sharp" set. A pop-in event is indicated during the loading section of the curve. Such an event is most likely indicative of the nucleation and propagation of crystalline defects, a

fact we confirm later.

Figure 5.4(c) shows a load/unload curve from the indent circled in purple in Fig. 5.3(c). No pop-in/pop-out event is observed during loading/unloading. Instead, a discontinuity event is observed during the hold duration (a pop-hold event). The presence of the event during the hold period, where the pressure is relatively constant, suggests a delay between when critical pressure was reached and when the associated deformation mechanism occurs. That is, the associated mechanism is nucleation limited. The penetration depth increases during this event similar to in a pop-in event. Unlike a pop-in event, there is no subsequent loading after this event. Therefore, it can not be categorically confirmed whether such events are indicative of phase transformation, defect nucleation, or possibly both. Thus, Raman spectra were taken to investigate the presence of phase transformation/crystalline defects within the residual indents.

Figure 5.5 shows Raman spectra taken from the indented regions. Figure 5.5 compares spectra taken from the three indents shown in Fig. 5.4 as well as a spectrum taken from an indentation site that responded elastically. The spectrum taken from the elastic indentation is identical to unindented dc-Si, showing there is no Raman-detectable change that has occurred during indentation. The spectrum from the indented region with a pop-out event in Fig. 5.4(a) shows peaks at ~350 cm^{-1}, ~385 cm^{-1}, ~400 cm^{-1}, and ~430 cm^{-1} which agree with the reported Raman modes of the bc8/r8 structure presented in Section 3.3. There is also no shifting or broadening of the dc-Si peak at 521 cm^{-1}. This suggests minimal crystalline defects have occurred within the measured region. The spectrum from the indent with a pop-in event shown in Fig. 5.4(b) shows no peaks associated with the bc8/r8 mixed structure such as the r8-Si peak at 353 cm^{-1} or the bc8-Si peak at 437 cm^{-1} [42]. Further, the dc-Si peak is shifted from 521 cm^{-1} to ~525 cm^{-1}. Further, the FWHM of this dc-Si peak is ~3 cm^{-1} broader than the same peak in the spectrum collected from the elastic indented region. The peak broadening suggests the presence of crystalline defects within the residual impression [203] while the peak shift is associated with a residual compressive stress of ~1.3 GPa [204]. The spectrum from the indent with a pop-hold event shown in Fig. 5.4(c) also shows no peaks associated with the bc8/r8 mixed structure. Similar to the Raman spectrum collected from the indent with a pop-in event, the dc-Si peak normally at 521 cm^{-1} has been shifted (to ~527 cm^{-1}) and broadened (by ~4 cm^{-1}). This suggests that the pop-in event and pop-hold event are indicative of a similar plastic deformation. Note that the shift in the dc-Si peak is not the same in these two cases. However, the presence of the peak shift is indicative of crystalline defects regardless of the amount shifted. XTEM was used to further investigate the plastic deformations.

Figure 5.6 shows a BF XTEM image taken from an indent that was categorised in the 'pop-out' set based on its load/unload curve and contained peaks associated with the bc8/r8 structure

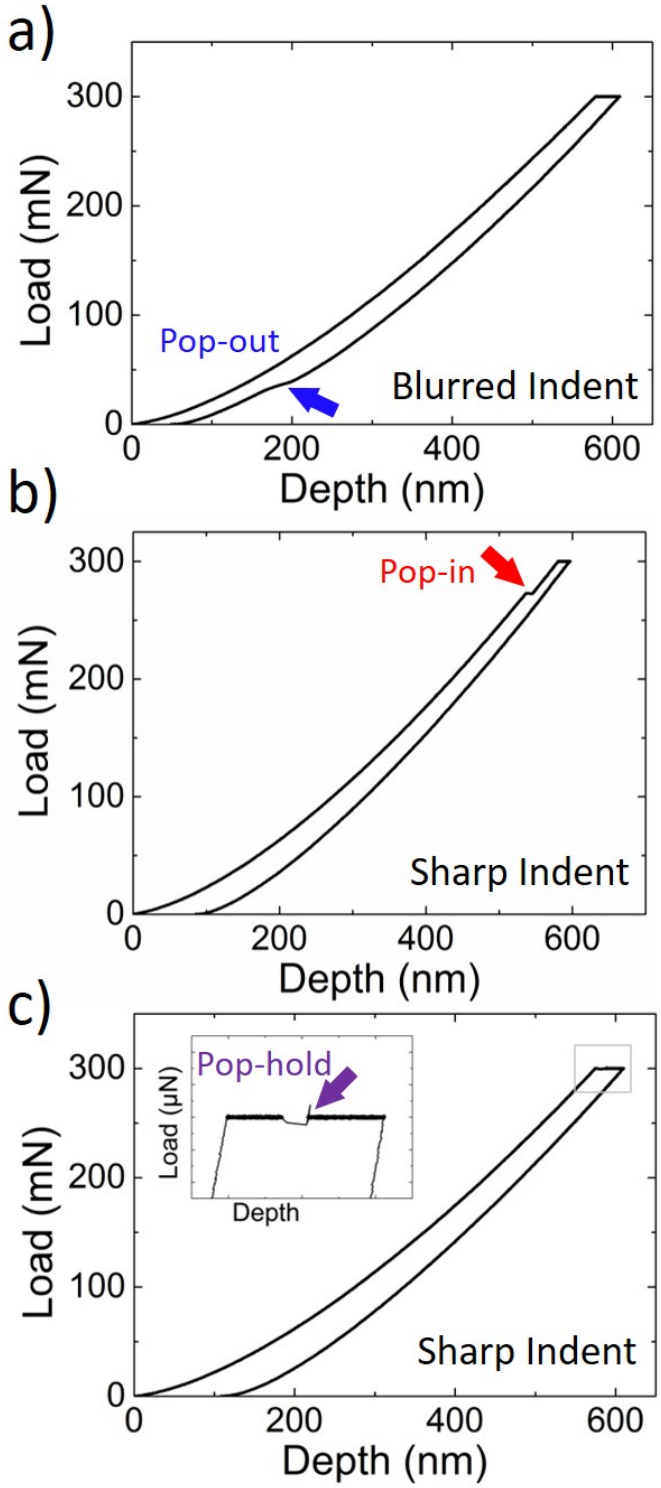

Fig. 5.4: Load unload curve with (a) a pop-out discontinuity during unloading, (b) a pop-in discontinuity during loading, and (c) a discontinuity during the hold duration (pop-hold). The pop-hold is enlarged in the inset for clarity. The optically-distinct set to which each indent belongs is also indicated.

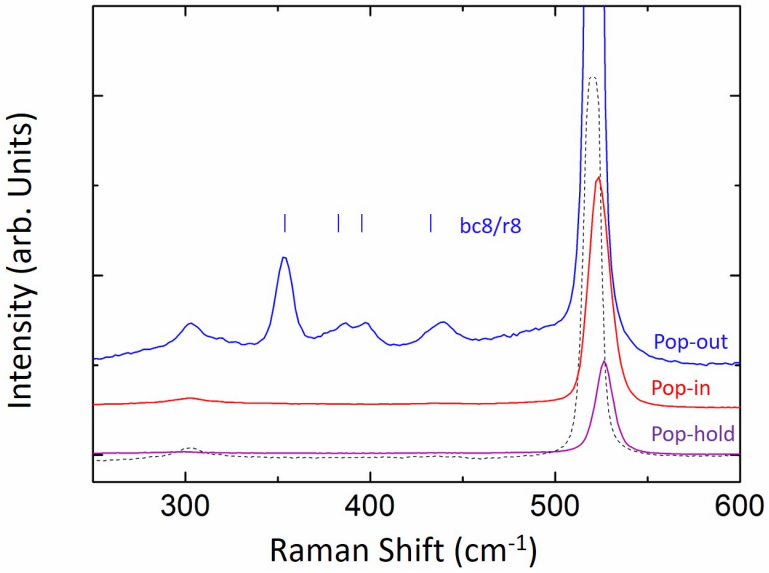

Fig. 5.5: Raman spectra collected from the residual impressions of indents presented in Fig. 5.4. The peak positions associated with the bc8/r8 mixed structure are indicated. A spectrum collected from an indent that responded elastically (dotted) that is indistinguishable from an unindented dc-Si spectrum is also included for reference.

in its Raman spectra. A transformed region ∼4 μm wide and ∼400 nm deep is observed. The region appears to be comprised of two microstructural types, a very fine grained polycrystalline microstructure that exists in the centre and along the edges of the material as well as an amorphous phase that appears in the remaining sections of the transformed region. The SADP in the inset, taken from the circled region, confirms the presence of both the bc8/r8 mixed structure and a-Si. Note that several reflections from bc8-Si and r8-Si are very similar in terms of d-spacing [30, 44]. Thus, it is not possible to definitively identify the presence of both bc8-Si and r8-Si within each SADP presented. As it has been established in the previous chapter that both phases are present, the presence of reflections associated with bc8-Si will be used to indicate the presence of phase transformation into the bc8/r8 mixed structure for the rest of this chapter. The green circle sits at a d-spacing of 2.71 Å, which can be associated with the [211] plane of bc8. The broad ring centred around a d-spacing of 3.14 Å indicates the presence of a-Si in the selected region. As (β-Sn)-Si is thought to transform to a-Si under fast unloading of indentation pressure, a-Si is commonly observed alongside the bc8/r8 mixed structure after indentation [105]. Interestingly, there are no signs of crystalline defects under the transformed region. This is comparable to the XTEM image presented in Fig. 5.1(a) where phase transformation was also the sole deformation mechanism present.

Figure 5.7 shows a BF XTEM image taken from an indent from the other set, categorised

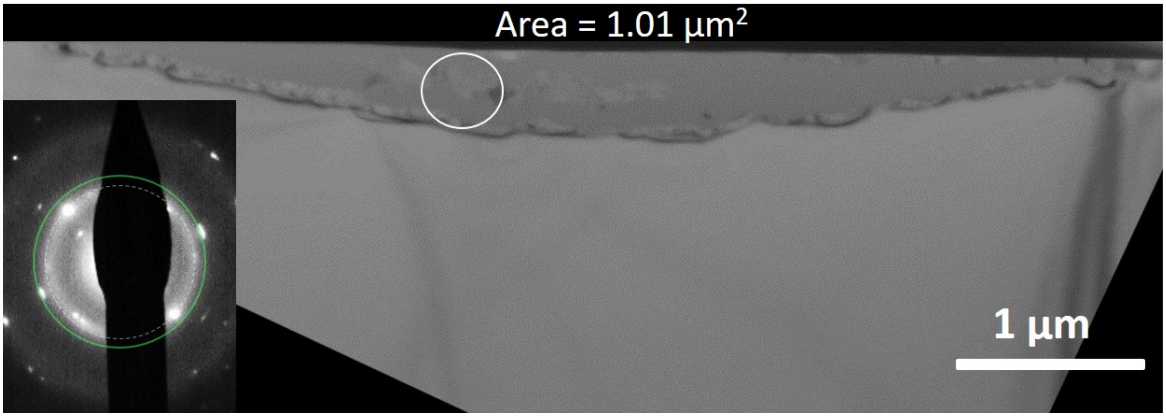

Fig. 5.6: BF XTEM image of a 300 mN indent that has phase transformed. (inset) SADP taken from the circled region. Reflections at a d-spacing of 2.71 Å (green circle) are associated with the [211] plane of bc8, indicating the presence of the bc8/r8 mixed structure. The diffuse rings (white circle) indicates the presence of a-Si. The area of the transformed region has been included.

as 'pop-in' after indentation and containing only a shift and broadening of the dc-Si peak at 521 cm^{-1} in its Raman spectrum. Two major forms of crystalline defects can be observed. Firstly, there is a cluster of extended defects that lie ~1 μm below the surface. Secondly, long slip bands along [111] planes extend from the surface down to ~4 μm deep. Careful SADP analysis confirmed that there is no evidence for phase transformation in this indent.

It has been previously suggested that defects may be required to nucleate phase transformation [104]. Thus, it is possible that the nucleation of crystalline defects may have occurred but not observed as they are covered by subsequent phase transformation. However, the depth of the defects (particularly the slip bands shown in Fig. 5.7) are so large that the phase transformed region shown in Fig. 5.6 could not have nucleated after defect formation and subsequently covered them up. Thus, it has been shown that indentation to a maximum load of 300 mN has produced two different plastic deformation pathways (i.e. phase transformation and crystalline defects). Based on the TEM results, the Raman and load/unload data can now be used to further categorise the plastic indents found in Table 5.1 into those that exhibit phase transformation and those that exhibit the formation and nucleation of crystalline defects. This is shown in Table 5.2. Indents that have nucleated defects as well as indents that have phase transformed are found at all maximum loads except 200 mN where very few indents plastically deformed. Further, increasing the hold time to 60 minutes has not produced a substantial rise in the probability of phase transformation occurring. The implications are discussed in greater detail in section 5.4

In the next section, the maximum load is further varied to gain a more complete picture of the pathways that lead to the two distinct sets of indents and how each set will evolve under

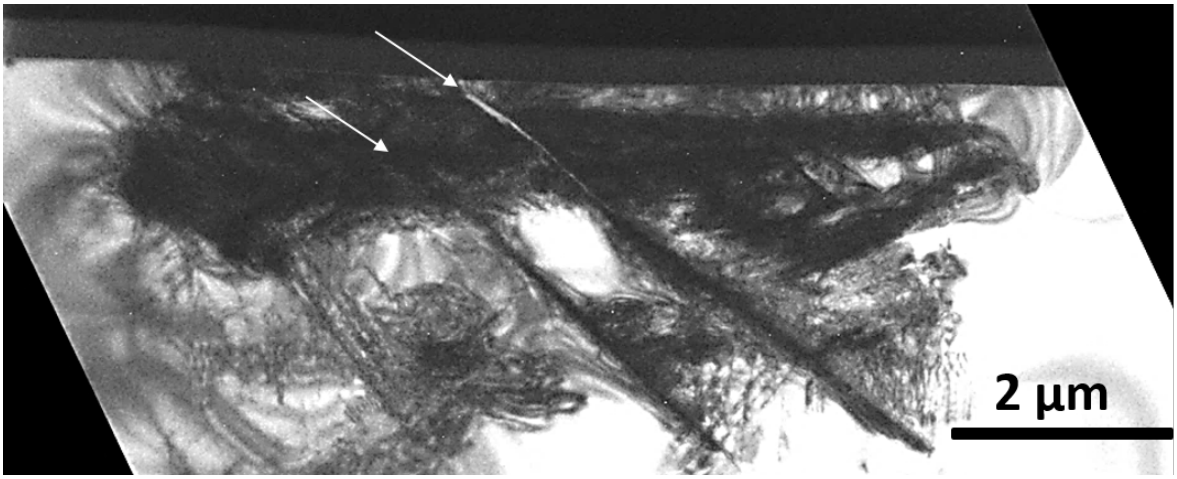

Fig. 5.7: BF XTEM image of a 300 mN indent that has nucleated and propagated crystalline defects. Prominent bands extending from the surface to ∼4 μm deep have been indicated by the arrows.

increasing indentation pressure.

5.3.2 Two Distinct Pathways

All indents in this section have a hold duration of 15 minutes. Further, the presence of the bc8/r8 mixed structure and/or a-Si are confirmed via the SADP inset within each figure. Where more than one type of microstructure appears to be found within the transformed region (e.g. a portion of the region appears to be crystalline, other portions appear to be amorphous), the area from which the SADP is taken is circled on the XTEM image. For each figure containing a phase transformed region within this section, the measured area of the transformed region is presented above the region.

Low Load: 200 mN - 300 mN

The evolution of the shape and size of the phase transformed region is investigated by imaging the plastically deformed region (via XTEM) as the maximum load is increased from 200 mN (lowest maximum load that produced plastic indentation) to 250 mN to 300 mN. Figure 5.8 shows XTEM images of two indents made to a maximum load of 300 mN. The transformed region in Fig. 5.8(a) has the bc8/r8 mixed structure sandwiched between a-Si while the region in Fig. 5.8(b) appears to be comprised entirely of the bc8/r8 mixed structure. The shape of the transformed regions shown in this figure is different to the shape from the region shown previously in Fig. 5.6, which presents an indent made under similar conditions. In the previous indent, the phase transformed region was shaped like a segment of a circle. That is, in Fig.

Maximum Load	Hold Duration	PT	CD	PT/CD ratio
300 mN	1 min	2%	8%	0.25
300 mN	2 min	5%	13%	0.38
300 mN	3 min	15%	43%	0.35
300 mN	15 min	57%	35%	1.63
275 mN	15 min	34%	12%	2.83
250 mN	15 min	35%	11%	3.18
225 mN	15 min	6%	1%	6
200 mN	15 min	4%	0%	
200 mN*	60 min	0%	0%	

Table 5.2: The percentage of phase transformation/crystalline defect responses under different indentation conditions based off the Raman spectra collected from the indented regions. The ratio between the two deformation mechanisms is also given to show the increase in phase transformation with increasing hold time and decreasing load. *Only five indents were performed at 200 mN with a 60 minute hold duration. Thus, this result may not be statistically representative.

5.6, the bc8/r8 to dc interface is a single curve and the transformed region is continuous from this interface to the sample surface. In this section, such transformed regions are described as "segment-shaped regions". However, the shape of the transformed regions presented here in Fig. 5.8 are not circle segments and a region of dc-Si is present above both transformed regions. In this section, these discontinuous transformed regions are described as "buried layers". The observation of both a segment-shaped region and a buried layer after indentation to 300 mN raises the question; are these two distinct pathways of phase transformation or two different points along the same pathway? That is, could this buried layer be a phase transformation that did not have the time to fully transform due to the nucleation limited nature of the transformation? Would holding at maximum load for longer have resulted in a progression to a segment-shaped region?

One useful value that may help answer these questions is the "extrapolated area" of the transformed region. This refers to the projected area covered if the buried layer were segment-shaped, with the deepest point on of the buried layer used as the bottom of the segment (i.e. the outlined region in Fig. 5.8). The measured areas and extrapolated areas of the phase transformed region are indicated in the figure. The average areas for all the XTEM images presented in this chapter and in ref. [55] are in Table 5.3. The segment-shaped regions have the same measured and extrapolated area. It can be noted that the standard error of the measured area is greater than the standard error in the extrapolated area case. This is due

to the greater variance in the measured area. In particular, the buried layers have a smaller transformed area than a segment-shaped region made to the same maximum load. This suggests that the buried layer does not represent a region that has completely phase transformed. That is, the buried layer is in the process of gradually expanding to a segment-shaped region when pressure was removed which results in an "in progress" transformation being observed.

Maximum Load	Area (μm^2)	Error (%)	Extrapolated Area (μm^2)	Error (%)
750 mN	5.36	4		
500 mN	2.32	2		
300 mN	0.763	41	1.12	10
250 mN	0.399	43	0.458	25
200 mN	0.161	12	0.262	4

Table 5.3: The area of the phase transformed region in XTEM for different maximum loads. For maximum loads where buried layers were observed, both actual and projected areas are listed.

Figure 5.9 shows XTEM images of indents made to 250 mN. The region in Fig. 5.9(a) is asymmetric, with the region on the left being deeper and comprised of bc8/r8 while the right is comprised of a-Si. There does not appear to be a dc-Si layer between the transformed region and the surface. The region in Fig. 5.9(b) is segment-shaped except for the rough interface while the region in (c) is almost segment-shaped with only a slight amount of dc-Si above the region on the left. Both regions are comprised of a-Si.

Figure 5.10 shows XTEM images of indents made to 200 mN, with both showing transformed regions that are buried layers. Further, both are entirely comprised of a-Si.

Among these XTEM images, it appears that the bc8/r8 mixed structure is more prevalent within the larger transformed regions. These results did not suggest a correlation between the maximum load and the prominence of a buried layer. For example, two of the three images presented from 300 mN indents had clear dc-Si layers between the transformed region and the surface. However, only one of the three images presented from 250 mN indents had any dc-Si layer above the transformed region. This suggests that, if there is indeed a progression from the buried layer to the segment-shaped regions, this progression is not strongly pressure dependent. The implications of these results are discussed in greater detail in Section 5.4.

High Load: 500 mN - 750 mN

The evolution of the two distinct deformation pathways are now further investigated by increasing the maximum load to 500 mN and 750 mN. Indents were categorised as "phase trans-

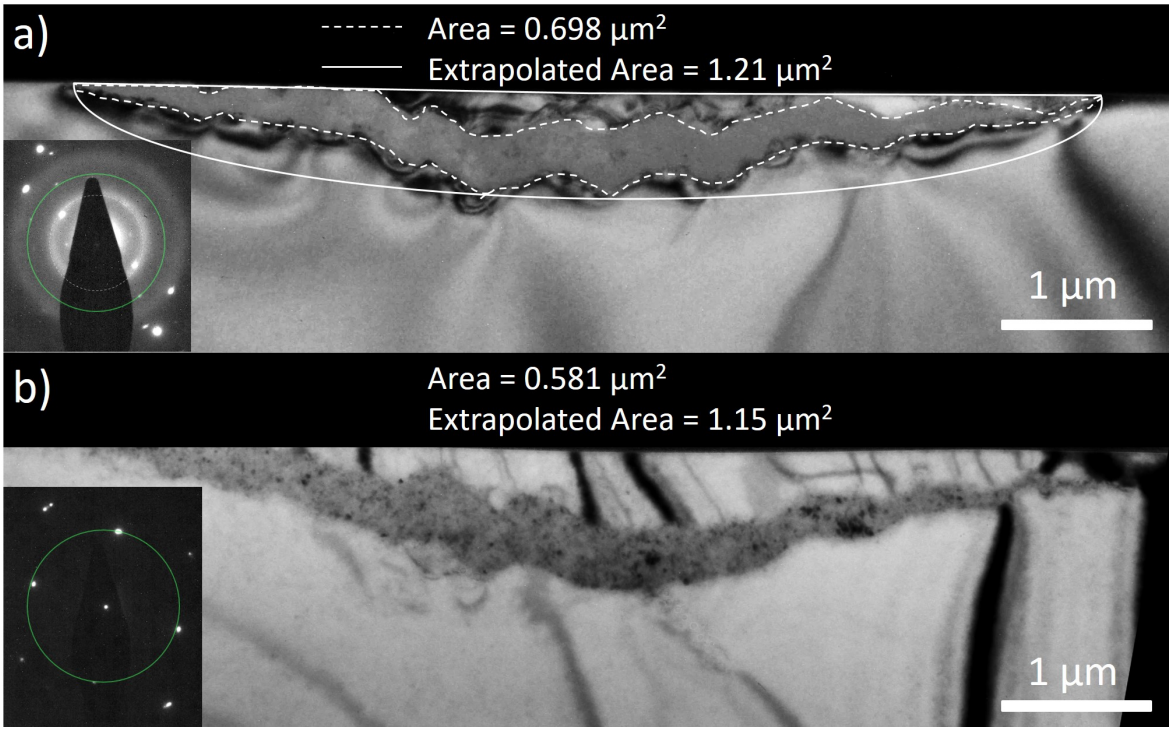

Fig. 5.8: XTEM images of two separate indented regions formed under identical loading conditions with a maximum load of 300 mN and a 15 minute hold duration. Both indents have phase transformed to form a buried layer with a slightly differently shaped transformed area. The observed transformed area (dotted line) and extrapolated area (solid line) are outlined in (a) and the measured areas are presented above each region. (inset) SADP taken from the transformed regions. (a) Reflections at a d-spacing of 1.92 Å (green circle) are associated with the [222] plane of bc8, whereas the diffuse ring (dotted white circle) indicates the presence of a-Si. (b) Reflections at a d-spacing of 2.71 Å (green circle) are associated with the [211] plane of bc8.

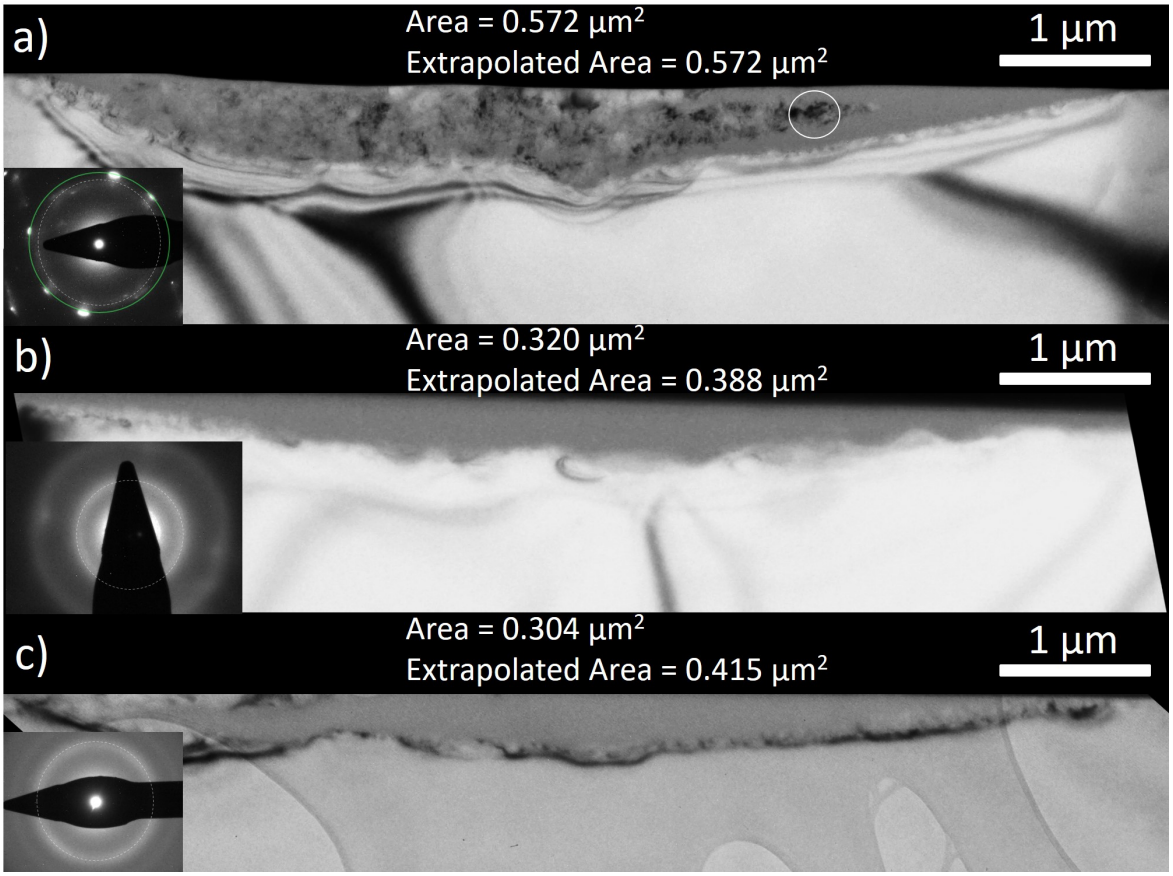

Fig. 5.9: XTEM images of an indented region made to a maximum load of 250 mN that has phase transformed. The size of the observed transformed area and of the area after extrapolating to a segment-shaped region are presented above each region. (inset) SADP taken from the transformed regions. (a) Reflections at a d-spacing of 2.72 Å (green circle) are associated with the [211] plane of bc8, whereas the diffuse ring (dotted white circle) indicates the presence of a-Si. (b)-(c) The diffuse ring (dotted white circle) indicates the presence of a-Si.

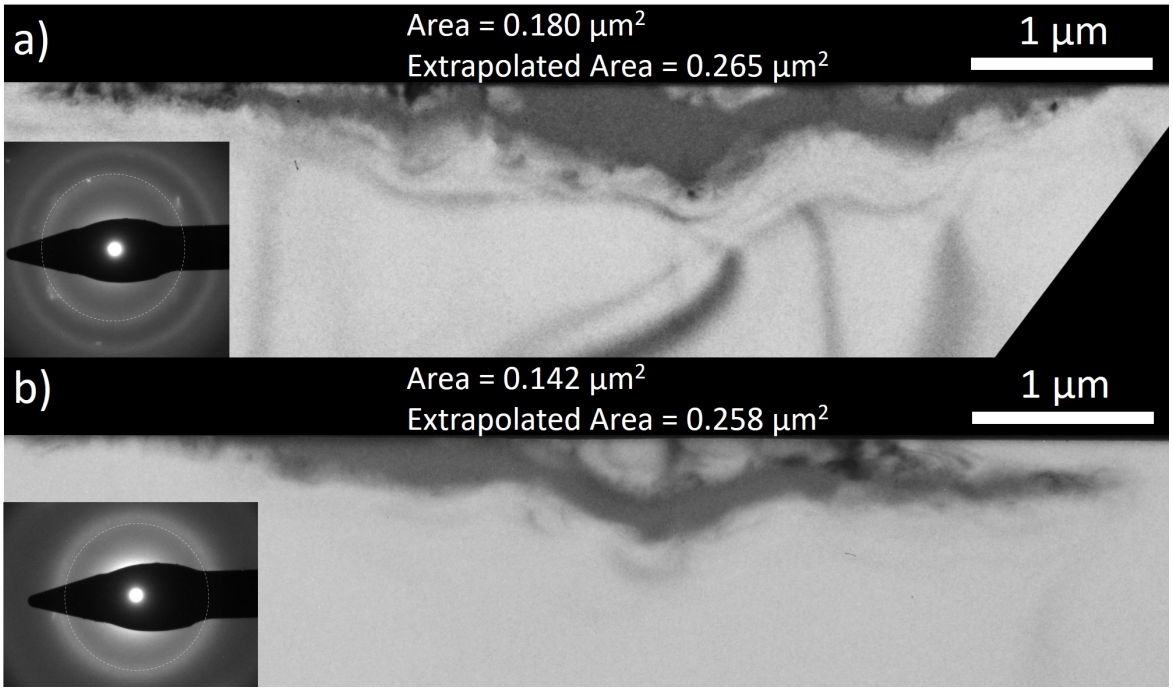

Fig. 5.10: XTEM images of indented regions made to a maximum load of 200 mN that have phase transformed. The size of the observed transformed area and of the area after extrapolating to a segment-shaped region are presented above each region. (inset) SADP taken from the transformed regions. The diffuse ring (dotted white line) in both is indicative of a-Si.

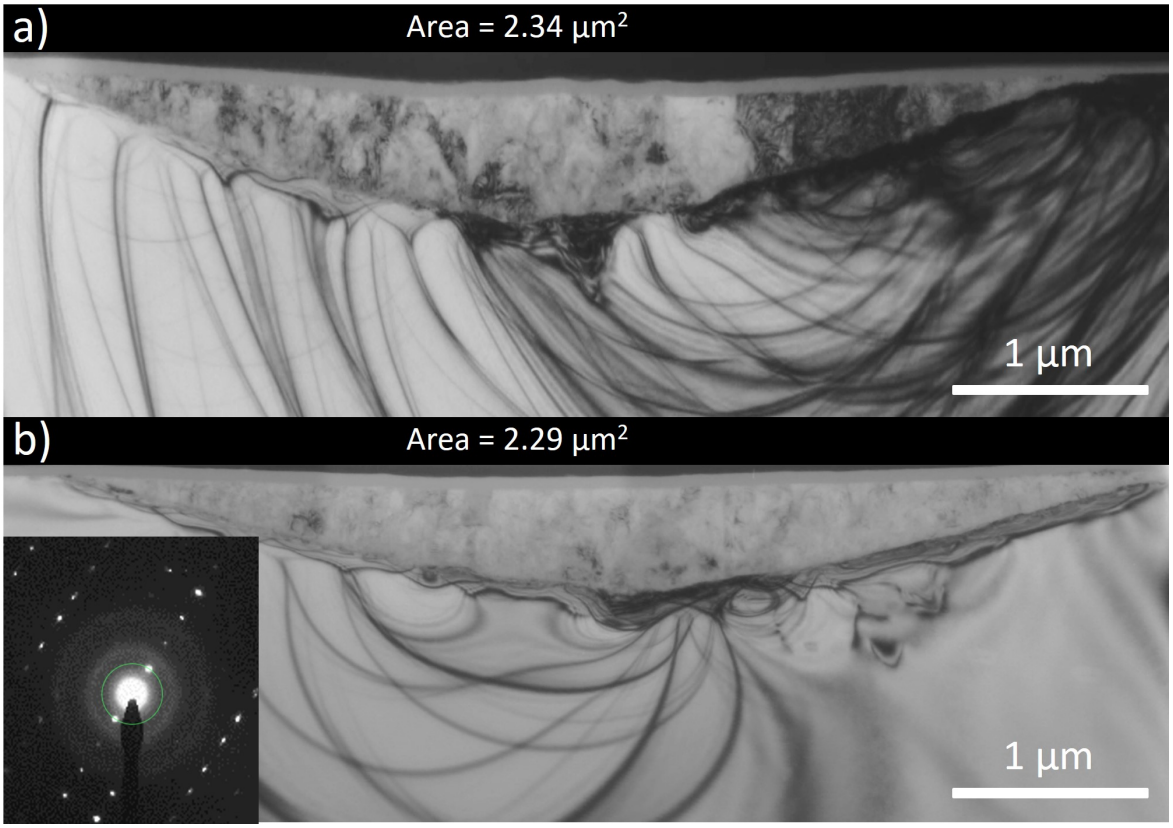

Fig. 5.11: XTEM images adapted from Ref. [55] of indented regions made to a maximum load of 500 mN that have phase transformed. The measured transformed area is presented above each region. (inset) Representative SADP taken from the transformed region in (b). Reflections at a d-spacing of 3.30 Å (green circle) are associated with the [002] plane of bc8

formed" or "crystalline defects" using Raman microspectroscopy as established previously. All inset SADPs in this section are presented to confirm the presence of the bc8/r8 mixed structure in the transformed region. Figure 5.11 shows XTEM images of two separate indents loaded to 500 mN that exhibit phase transformation that have been adapted from Ref. [55]. Importantly, the phase transformed regions in both are segment-shaped and have similar width, depth and shape. The morphology of these indents has two key differences compared to that of the 300 mN phase transformed case shown in Fig. 5.6. Firstly, the region is unsurprisingly larger; it is ∼6 μm wide and ∼650 nm deep (compared to ∼4 μm wide and ∼400 nm deep for the 300 mN load indents). Secondly, unlike in the 300 mN case, there does not appear to be any a-Si within the transformed region. For both the 300 mN and the 500 mN phase transformed indents there is essentially no underlying crystalline defects and hence phase transformation is the sole plastic deformation mechanism. Further, it appears that the only difference in the dc-Si to (β-Sn)-Si transformation between the 300 mN and 500 mN maximum load indents is the increased volume of material transformed.

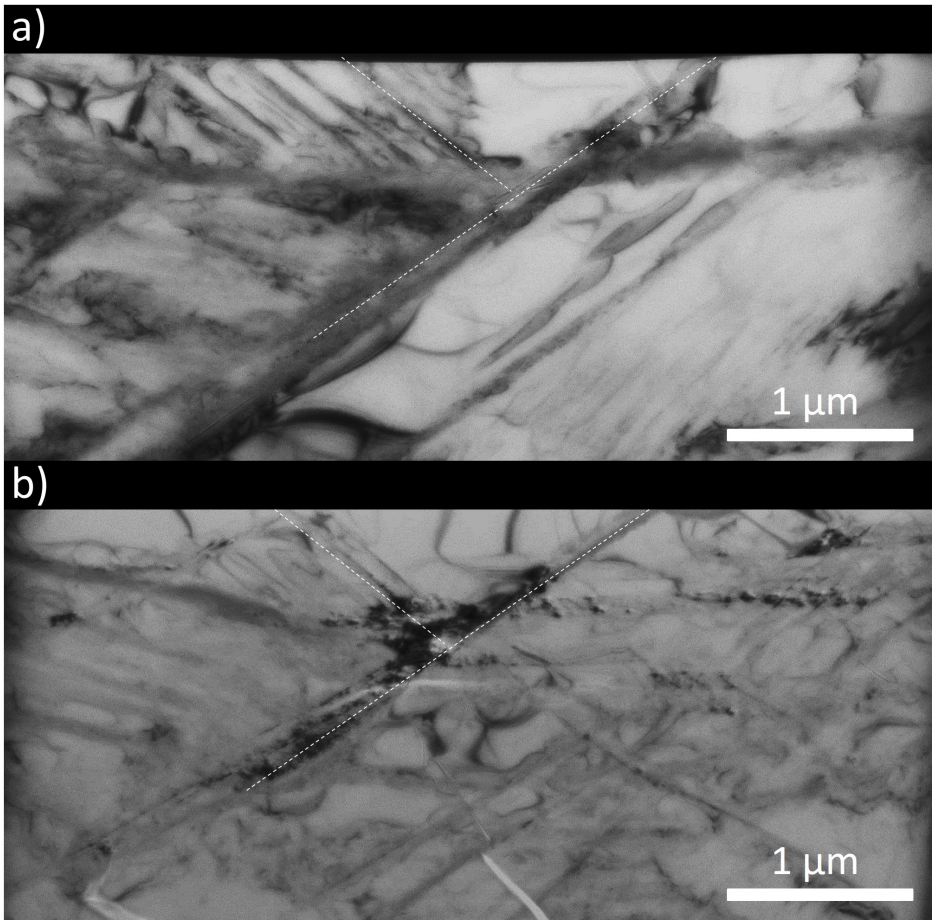

Fig. 5.12: XTEM images of indented regions made to a maximum load of 500 mN that have nucleated crystalline defects. The distribution of the defects do not appear to be related apart from the size of the slip bands and the depth of their intersection (indicated by the dotted lines).

Figure 5.12 shows XTEM images of indents loaded to 500 mN that exhibit crystalline defects. Most prominently, slip bands have formed and appear to intersect roughly below the middle of the indent (as indicated by the dotted lines) in both images. The density and nature of the other crystalline defects appear to have a different distribution between the two indents presented. That is, defect nucleation is less repeatable than phase transformation. Similar to the phase transformed indents, where there is only one deformation made, the nucleation and propagation of crystalline defects is the sole form of plastic deformation within the images shown in Fig. 5.12. Thus, at and below 500 mN maximum load, the two pathways of phase transformation and propagation of crystalline defects are distinct, with no case observed in which both pathways exist simultaneously. In the phase transformed cases at loads at and below 500 mN, the main difference is that the higher loads have a larger volume of phase transformed material.

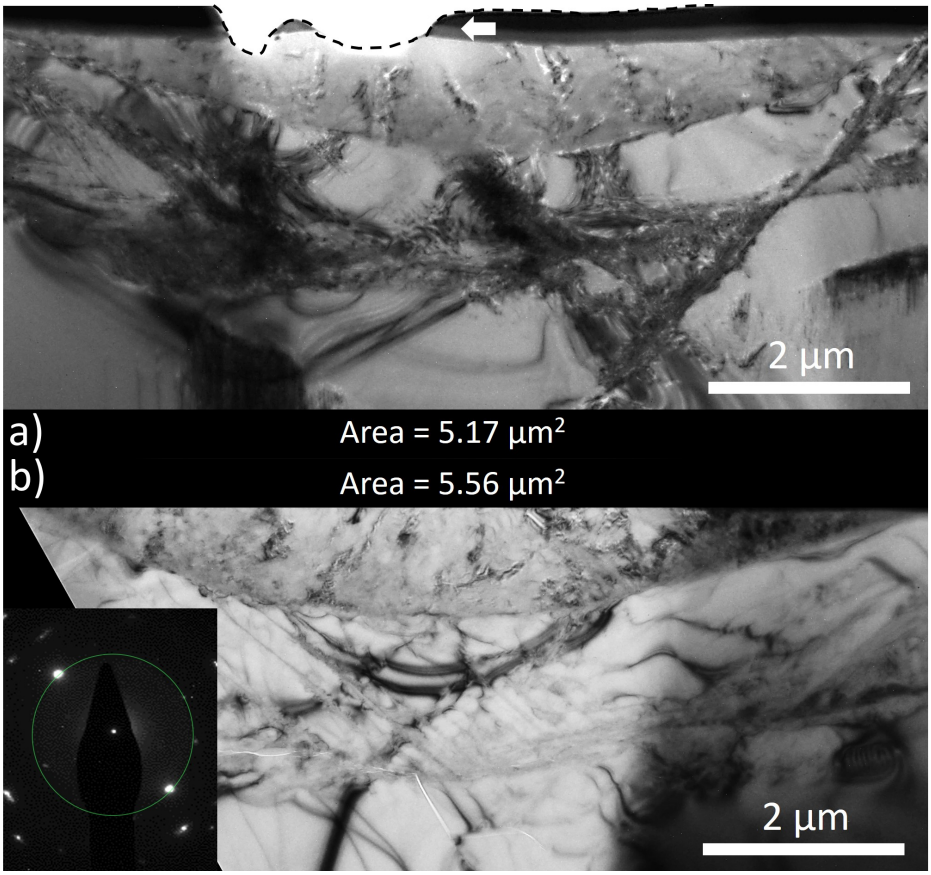

Fig. 5.13: XTEM images of indented regions made to a maximum load of 750 mN that are phase transformation dominant. The measured transformed area is presented above each region. Note that the top left section of the transformed region in (a) has been damaged during the FIB thinning process (as indicated by the arrow). (inset) Representative SADP taken from the transformed region in (b). Reflections at a d-spacing of 2.70 Å (green circle) are associated with the [211] plane of bc8.

After indentation to a maximum load of 750 mN, all the Raman spectra collected from the indented region exhibited peaks associated with the bc8/r8 mixed structure. However, differences were observed in the XTEM images. These were separated into two categories, "phase transformation dominant" or "crystalline defect dominant". Figure 5.13 shows indents from the phase transformation dominant set. These images are similar to the 500 mN phase transformed indents in two ways. Firstly, the entire transformed region consists of the bc8/r8 mixed structure. Secondly, the transformed region is a spherical segment that is larger than the segments observed at lower loads. In this case, unlike its 500 mN counterpart, crystalline defects are now also present in dc-Si beneath the transformed region.

Figure 5.14 shows indents from the crystalline defect dominant set. While crystalline defects are dominant in these indents, phase transformed regions are also present (outlined by the

dotted line). The phase transformed regions observed here are significantly different to those observed in the phase transformation dominant indents. Firstly, the shape of the transformed region is no longer segment-shaped and is very different between the two cases shown in Fig. 5.14. Secondly, the transformed region in Fig. 5.14(b) does not appear at the centre of the indentation area. The centre of the indentation area can be identified using the shape of the residual impression, with the greatest residual depth in the centre of the image (as indicated by the dotted line) which is to the right of the transformed region. Finally, the volume of transformed material is significantly smaller than the volume observed in Fig. 5.13. In fact, the transformed volume is smaller than even the volume transformed at the lower load of 500 mN shown in Fig. 5.11. Comparing the 500 mN phase transformed case with the 750 mN crystalline defect dominant case shown in Fig. 5.14(a), the width of the transformed region is approximately the same ($\sim$6 μm) but the maximum depth of the 750 mN case is only $\sim$400 nm compared to the $\sim$650 nm depth of the 500 mN case. Further, the transformed region shown in Fig. 5.14(b) is smaller than both of the above regions, with a width of $\sim$3 μm and a depth of $\sim$200 nm. Thus, it is impossible for the phase transformed regions similar in size to those presented in Fig. 5.11 to have been present in the indented regions shown here. That is, it is evident that the crystalline defect dominant indents first nucleated crystalline defects before phase transformation occurred during subsequent loading (and vice versa for the phase transformation dominant indents). Thus, even within a maximum load regime where both plastic deformation mechanisms are present, the two pathways remain distinct.

5.4 Discussion

Nucleation Limited Plastic Deformation

The results presented in this chapter have clearly shown that two indents with experimentally-identical loading conditions can result in two significantly different plastic deformations. This appears to resolve the previously reported, seemingly contrasting, models that suggest that crystalline defects occur before phase transformation [104, 201] or alternatively phase transformation occurs before crystalline defects [101]. We suggest that such a result has not previously been reported due to two factors.

Firstly, it has been shown that both phase transformation and the nucleation and propagation of crystalline defects are nucleation limited. That is, there is a delay between when the critical conditions for plastic deformation are reached and when an observable amount of plastic deformation has occurred. This is most evident in the observation of purely elastic responses to indentations even though the induced pressure is far above the critical pressure for phase transformation (as shown in Section 5.3.1). Thus, the utilisation of a hold duration to promote

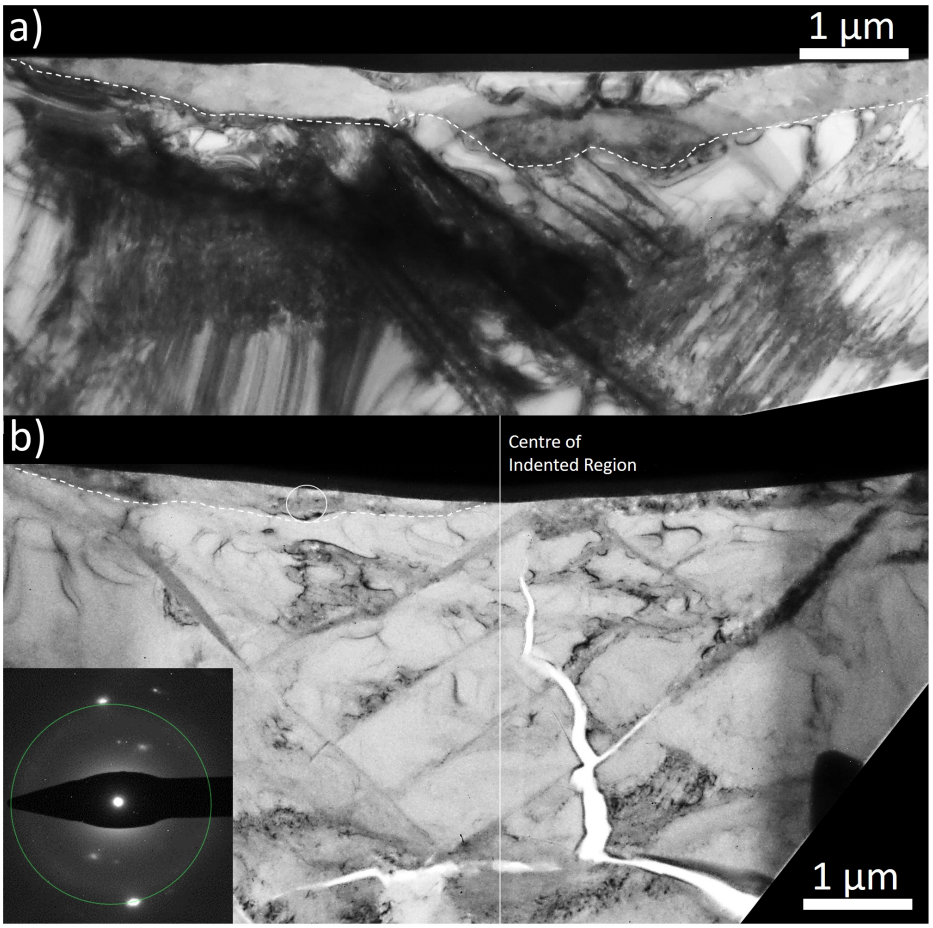

Fig. 5.14: XTEM images of indented regions made to a maximum load of 750 mN that are crystalline defect dominant. The phase transformed regions have been indicated (dotted line). The centre of the indented region, determined by the deepest point of the residual impression, is also indicated (solid line). (inset) Representative SADP taken from the transformed region in (b). Reflections at a d-spacing of 2.70 Å (green circle) are associated with the [211] plane of bc8.

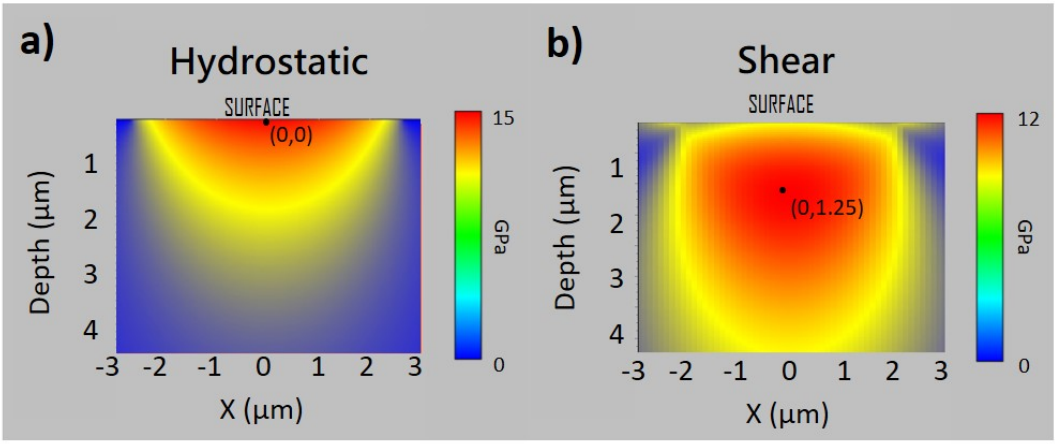

Fig. 5.15: Simulated pressure distributions of the (a) hydrostatic and (b) shear stress distributions under indentation to a maximum load of 300 mN using the Elastica analytical software. The co-ordinates for the points of maximum stress are indicated.

plastic deformation is crucial to the observation of the present results.

Secondly, the large size of the spherical tip compared to previous studies may explain why this result has not been previously observed. In this work, the large tip diameter gives rise to a clear separation between the point of maximum shear stress and maximum hydrostatic pressure within the sample. Figure 5.15 shows simulations of the (a) hydrostatic pressure and (b) shear stress experienced by the sample under indentation with a 21 μm diameter spherical tip to a maximum load of 300 mN. The region of maximum hydrostatic pressure is the point where the tip first touches the surface. The point of maximum shear stress lies at a distance of $\sim$0.25 μm below the point of maximum hydrostatic pressure. This distance varies relative to both tip size as well as maximum load [92,149]. Figure 5.16(a) plots the Elastica simulated separation between maximum hydrostatic pressure and maximum shear stress as a function of spherical tip radius. The separation at a maximum load of 300 mN is plotted in red, whereas the separation when a hydrostatic pressure of 11 GPa is reached is plotted in black. This suggests that, for larger spherical tips, the pressure conditions at the two distinct pressure maxima must be considered when calculating the onset of incipient plasticity.

Chrobak *et al.* proposed a method for calculating the onset of incipient plasticity [101]. This method is based on the generally accepted idea that phase transformation is primarily driven by hydrostatic pressure and nucleation of crystalline defects is primarily driven by shear stress (as mentioned in Section 5.1). This method compared the ratio between critical shear stress for crystalline defects (τ_c = 7.7 GPa) and the critical hydrostatic pressure for phase transformation (σ_{PT} = 11 GPa) to the ratio between the hydrostatic pressure (σ_h) and shear stress (σ_s) at a given point. If the hydrostatic pressure/shear stress ratio (σ_h/σ_s) is higher than σ_{PT}/τ_c = 1.4, then phase transformation is expected to occur first (and vice versa).

Using this method, Chrobak *et al.* noted that the hydrostatic pressure/shear stress ratio at the point directly under the indenter tip was always larger than $\sigma_{PT}/\tau_c = 1.4$ and concluded that phase transformation should occur first. This can not be considered a general solution as they did not take into consideration the point of maximum shear stress. To use the conditions in this work as an example, at the point of maximum hydrostatic pressure indicated in Fig. 5.15(a) phase transformation is predicted to occur first ($\sigma_h/\sigma_s = 2.7 > \sigma_{PT}/\tau_c = 1.4$) which is in agreement with the result reported by Chrobak *et al.*. However, at the point of maximum shear stress indicated in Fig. 5.15(b) the nucleation of crystalline defects is predicted to occur first ($\sigma_h/\sigma_s = 0.71 < \sigma_{PT}/\tau_c = 1.4$) according to the same method. Therefore, a more accurate description of this method would be that it predicts which deformation mechanism has the potential to occur.

Figure 5.16(b) plots the simulated maximum shear stress and maximum hydrostatic pressure as a function of maximum load for a 21 μm diameter spherical tip. The load required for critical shear stress (7.7 GPa) is ~50 mN, while the load required for critical hydrostatic pressure (11 GPa) is ~100 mN. Therefore, at 300 mN the pressure conditions are such that both plastic deformation mechanisms have the potential to occur. As both mechanisms are nucleation limited, incipient plasticity under this set of indentation conditions is dependent on which deformation mechanism nucleates first. Interestingly, it is also possible that neither occurs and the sample responds elastically. It is also possible that the stochastic nature of both plastic deformation has a dependence on the number of defects within the initial, unindented sample. Thus, pretreatment of the substrate to remove (or introduce) defects may further promote phase transformation over defect propagation (or vice versa).

5.4.1 Two Pathways

Based on the above observation that incipient plasticity is dependent on two nucleation limited processes, we proposed a two pathways for plastic deformation of dc-Si under indentation-induced pressure. A schematic showing the alternative deformation pathways is shown in Fig 5.17. As indentation load on dc-Si increases plastic deformation may occur. The nature of this deformation is stochastic, with some indents deforming via phase transformation while others deform via nucleation and propagation of crystalline defects. Plastic deformation of either form causes a resultant pressure release. At lower loads, phase transformation and nucleation of crystalline defects act as competing deformation mechanisms and indents exhibiting solely one form of plastic deformation can be observed. The probability of either mechanism occurring within this low load regime is roughly equal, such that both pathways can be readily observed. For the experimental conditions presented here, this regime ranges from the onset of plasticity at 200 mN (as shown in Fig. 5.10) to at least 500 mN (as shown in Fig. 5.11). At higher loads, there is a sufficient increase in pressure beyond the initial plastic deformation (via either

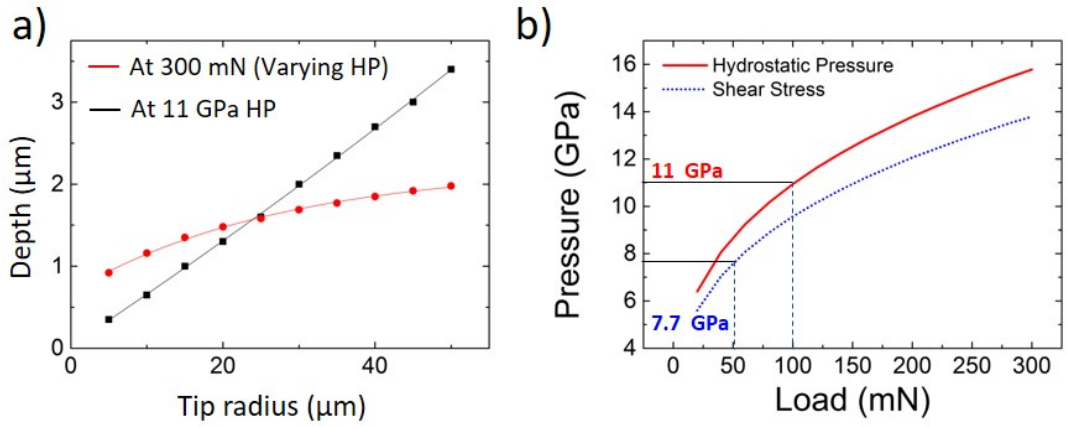

Fig. 5.16: (a) Simulated depth of the point of maximum shear stress as a function of tip radius at a constant load of 300 mN (red) or at a load sufficient to produce a maximum of 11 GPa of hydrostatic pressure (black). (b) Simulated hydrostatic and shear stress as a function of load. The load at which the accepted critical pressures for crystalline defect formation and for phase transformation are reached is indicated.

mechanism) for the pressure to again reach the critical value for further transformation. In such cases, both deformation mechanisms can be observed. Even when both deformation mechanisms occur, it remains clear that one deformation mechanism occurs first; they are never simultaneous.

This can be observed in the difference in shape and volume of the phase transformed region observed after indentation to 750 mN. This is shown experimentally when the transformed region in Fig. 5.14 is compared to the region observed after indentation to 500 mN and 300 mN shown in Fig. 5.11 and Fig. 5.6. Evidence for sequential deformation processes is obtained by comparing the shape and volume of the transformed region of different indents at 750 mN, and also in comparing 750 mN indents (Fig. 5.14) with the lower load 300 and 500 mN indents in Figs. 5.11 and 5.6, respectively. For the 750 mN case shown in Fig. 5.14, the first deformation process was the nucleation and propagation of crystalline defects, which partially released the pressure under the indenter. As the pressure continued to increase, further plastic deformation in the form of phase transformation occured. Thus, despite the higher load, the volume of pressure-induced phase transformation is less than that observed at some lower loads.

This two pathway process also explains the irregular shape of the transformed region. Phase transformation is a hydrostatic pressure driven process, thus it is expected that the transformed region should resemble the hydrostatic pressure distribution which is spherical for a spherical tip indenting a flat surface. Indeed, the transformed regions observed in the phase transformation pathway are segment-shaped (i.e. roughly spherical). However, if crystalline

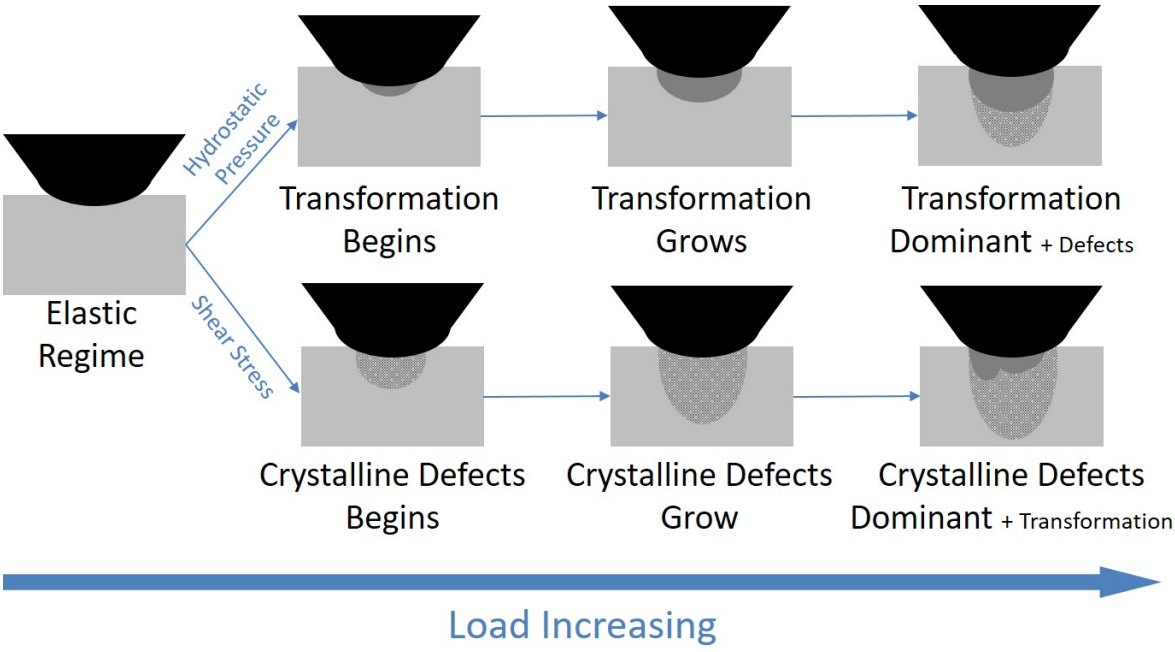

Fig. 5.17: A schematic showing the two pathways that plastic deformation in dc-Si may undergo during indentation loading with a large spherical indenter. The pathway where phase transformation occurs first is predominantly driven by hydrostatic pressure, while the pathway where crystalline defects occur first is predominantly driven by shear stress.

defects nucleate first, their non-uniform distribution and the fact that defects can be pinned at certain points (such as when they intersect [205, 206]) means that, at higher loads, phase transformation can nucleate at vastly different points within the crystalline defect structure. This leads to extremely asymmetric transformation volumes as shown in Figs. 5.12 and 5.14. Thus, the initial deformation mechanism plays an important role in determining the shape and size of the final phase transformed region.

5.4.2 The Phase Transformation Pathway at Low Loads

Spherical tips distribute hydrostatic pressure according to a radial distribution. Phase transformation is expected to form with a similar distribution, in a segment-shaped volume. At higher loads (500 mN and above), this expectation has been validated by the results presented here. However, at lower loads the phase transformed regions have been observed in non-segment-shaped regions (referred to in this work as buried layers). It is suggested that such a buried layer has not previously been observed as phase transformation has not been induced at a pressure so close to the critical pressure with large spherical indenters (as shown in Section 5.3.1). That is, this phenomenon is only present when the maximum hydrostatic pressure is not much greater than the critical pressure for phase transformation. It is further proposed that such a buried transformed zone is only possible due to the time-dependent behaviour of the nucleation of phase transformation on loading and its subsequent growth at higher loads [32, 59–61]. Finally, it is suggested that buried layers arise from the fact that, even though phase transformation is primarily driven by hydrostatic pressure, the observation of a buried transformed layer suggests that shear stress also plays a significant role [54, 201]. It was briefly suggested (in Section 5.3.2) that buried layers occur when pressure is removed before the time-dependent process of phase transformation has progressed to completion. The proposed process for first a buried layer and then full transformation at longer times or at higher loads is shown schematically in Fig. 5.18.

Initially, the tip is loaded to and then held at the maximum load. As the process is nucleation limited, no plastic deformation has occurred in this initial segment and the hydrostatic pressure and shear stress distributions can be found from the elastic behaviour using, for example, Elastica simulations. At some point during the hold duration, the onset of the nucleation limited phase transformation occurs. Observation of buried layers suggests that the initial transformed region does not occur at the maximum of hydrostatic pressure at the surface of the sample. Instead, as shear stress plays an important role in nucleation phase transformation [104], transformation initiates in regions below the surface where there is greater shear stress. The absence of a discontinuity event in the load/unload curve [shown in Fig. 5.4(a)] suggests that the onset of phase transformation does not lead to a substantial amount of material transformation instantaneously. Further, the lack of a change in slope in the loading curve

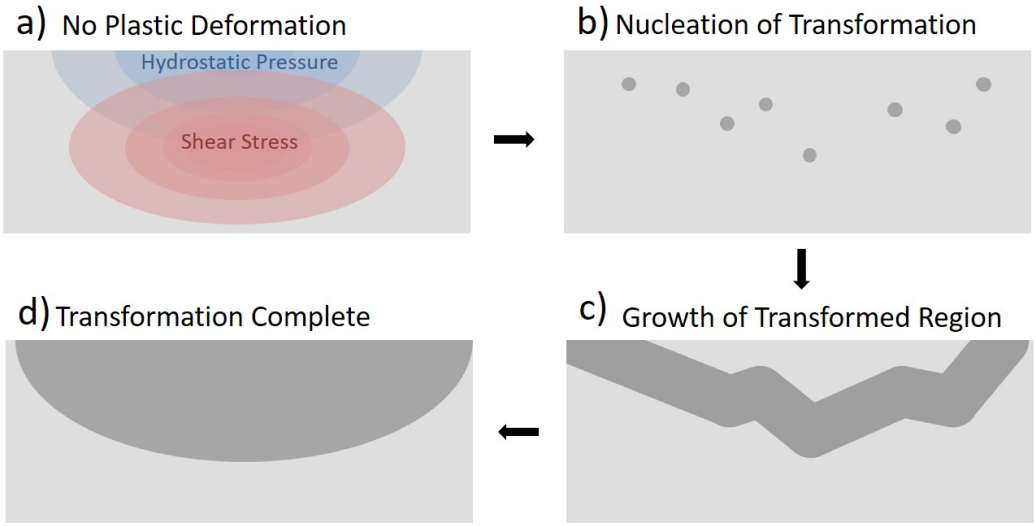

Fig. 5.18: Schematic of the proposed stages of phase transformation under spherical indentation. (a) The calculated distribution of hydrostatic pressure and shear stress before nucleation limited phase transformation occurs. (b) Nucleation of phase transformation occurs below the surface, at points where both hydrostatic pressure and shear stress are high. (c) The transformed region grows around the nucleation sites. (d) The transformation is complete, forming a segment-shaped region.

suggests subsequent growth of phase transformation is also a gradual process. Thus, the initial phase transformed regions are proposed to expand in the following manner. Firstly, they expand into a region similar in appearance to a buried layer. Then, further expansion results in a region that is segment-shaped. Note that the segment-shaped regions were observed to have a larger area (in XTEM) than the buried layer at the same maximum pressure (as can be seen in the XTEM images presented in Section 5.3.2). Extrapolation of the transformed area of a buried layer to the equivalent segment-shaped region gives similar areas to those of segment-shaped regions indented to the same maximum load (as shown in Table 5.3). Therefore, it is suggested that the transformed region is segment-shaped when a state of pressure equilibrium is reached (i.e. when all points that experience sufficient pressure for phase transformation have phase transformed). Due to the time-dependent nature of phase transformation, it is possible that unloading can occur before transformation is complete and equilibrium is reached. Upon unloading, phase transformation ceases and a buried transformed layer results. One possible explanation for why phase transformation that has not reached a state of pressure equilibrium has not previously been observed can be proposed using the Avrami equation. This equation calculates the volume fraction of the transformed state (Y) as:

$$Y = 1 - e^{\frac{-\pi . N . G^3 . t^4}{3}}$$

where t is the time, N is the nucleation rate of the transformation, and G is the growth rate of the transformed material. Under this equation a typical transformation has volume changes which are slow at the beginning and the end of the transformation with a rapid transformation region in between. As the results observed here are from the window of rapid transformation, it can be proposed that they have not been observed previously because the time window for making such observations is very small.

Table 5.2 shows that, when hold duration is kept constant, a higher maximum load results in a greater number of indents exhibiting phase transformation. This suggests that, while phase transformation is a time-dependent process for all these maximum loads, transformation occurs over a longer time frame at lower loads. Therefore, unloading before complete transformation (and observing buried layers) is more likely to occur at lower loads.

It should also be noted that an alternative proposed process is also possible, particularly at high loads, where some indents initiate phase transformation at the surface and the transformed region grows radially outward to form a segment-shaped region. Meanwhile, other indents initiate phase transformation below the surface and grow in a manner similar to the process detailed above. The validity of these two proposed processes warrants further investigation as it may allow for *in situ* snapshots of the dc-Si to (β-Sn)-Si process via properly timed pressure removal to preserve the in-progress transformation.

The observation of a-Si, particularly for low maximum loads, on unloading is also of interest. The β-Sn phase is known to transform to a-Si on fast unloading [75,92] and the bc8/r8 structure on slow unloading [37, 38, 50, 76]. Therefore, the relative distribution of the amorphous and crystalline phases after unloading may provide information on the process of pressure removal during unloading. It may well be that at lower maximum loads, on unloading the lower pressure at the point of unloading makes nucleation of the crystalline bc8/r8 phases (also nucleation limited) less probable than for higher maximum loads. In the 200 mN indents, there is only a-Si. In the 250 mN indents, one is fully a-Si, another has only a small amount of crystalline material in the middle and yet another is fully crystalline on the deeper side. Finally, in the 300 mN indents, one is fully crystalline while the other only has crystalline material in the middle. These results are in agreement with those by Zarudi *et al.* that reported an increase in crystalline phases at higher loads and that the location of the crystalline phases are stress-dependent. However, there is insufficient consistency within the amorphous/crystalline distribution presented in this chapter to expand on what has already been previously reported. It is clear that there are still unknowns surrounding the β-Sn to bc8/r8/a-Si transformation at such low pressure distributions. The desire for consistent production of solely the a-Si or solely the crystalline phases suggests this topic warrants further study.

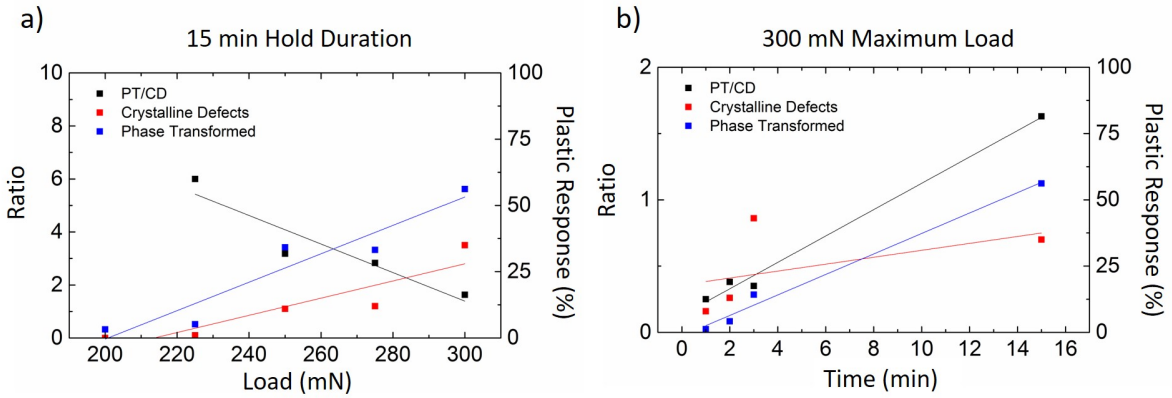

Fig. 5.19: Graph comparing the percentage response of the two plastic deformation mechanisms and the ratio between the two as a function of (a) maximum load with a constant hold duration of 15 minutes and (b) hold duration with a constant maximum load of 300 mN.

5.4.3 Promoting Phase Transformation using Hold Durations

The two pathways of plastic deformation detailed above show that, if phase transformation is the initial mechanism of plastic deformation, subsequent loading will continue to favour this transformation over the nucleation and propagation of crystalline defects. The number of indents that exhibited either form of plastic deformation were also shown to be dependent on maximum load and hold duration. Figure 5.19(a) plots the probability of either deformation mechanism occurring as a function of maximum load at a fixed hold duration of 15 minutes. The ratio between phase transformation and crystalline defects (PT/CD) is also included. Both mechanisms appear to increase with maximum load, most likely due to the increased number of plastic deformations (in contrast to indents that respond elastically). Unfortunately, increasing loads appears to favour defect nucleation over PT as the PT/CD ratio decreases. Figure 5.19(b) plots the same values as a function of hold duration (at a fixed maximum load of 300 mN). An increase in hold duration also leads to an increase in both forms of plastic deformation. More interestingly, increasing hold duration leads to an increase in the PT/CD ratio. This suggests that a lower maximum load held for a longer duration will maximise phase transformation over defect nucleation in the indents that deform plastically.

This decrease in maximum load to promote phase transformation must also be balanced against the increase in indents responding elastically. For example, at 200 mN with a hold duration of 15 min the only plastically deformed indents are phase transformed indents. This would suggest that, given the tip used in this chapter, 200 mN is the ideal maximum load to promote phase transformation. However, indents that exhibit plastic deformation only consists of 4% of the total indents made (shown in Table. 5.2). Further, a significant increase in hold duration to 60 minutes did not show a significant increase in indents responding plastically as none of

the five indents performed under these conditions exhibited plastic deformation.

To better visualise the relative impact of maximum load and hold duration, the mean contact pressure as a function of load can be considered. The mean contact pressure (P_c) can be calculated using the equation [91]:

$$P_c = \frac{F_m}{\pi . a_c^2}$$

where F_m is the maximum load, and a_c is the contact radius. The contact radius is calculated from the contact depth observed in the load/unload curve as detailed in section 3.1. Fig. 5.20 presents the Pressure-Time-Transformation plot of the presented phase transformed indent results. It should be noted that while the mean contact pressure for all indentations presented in this work are below the transformation threshold of 11 GPa, the mean contact pressure is averaged over a wide area that includes many regions where contact is made but no transformation occurs, thus such a low mean pressure is expected. This plot indicates that, within the regimes explored in this work, increasing load has a higher impact on the occurrence of phase transformation than hold duration. However, this greater increase occurs alongside an increase in the nucleation and formation of crystalline defect which may negatively affect the quality of the phase transformed region.

5.5 Summary

In this chapter, results showing that a hold duration promotes plastic deformation have been presented. By using a hold duration, a maximum load regime which had previously only responded elastically to indentation has exhibited plastic deformation. Within this regime, phase transformation and the nucleation of crystalline defects are shown to exist as competing deformation mechanisms. Both processes are nucleation limited and stochastic in nature. For the tip used in this work, it is shown that between 200 mN - 500 mN there exists a pressure regime where, once nucleated, each deformation mechanism is the sole observed deformation. At higher loads (750 mN and above), sufficient pressure is present for both mechanisms to occur. The results suggest that the initial deformation mechanism that occurred remains dominant within the residual indent even at this higher load.

Controlling the initial form of plastic deformation is of great importance, leading to several avenues of further study. Firstly, the pressure distribution within the regime where plastic deformation first occurs leads to buried layers of phase transformed material due to the interplay between hydrostatic and shear stress. There is potential to further understand how the two stresses interact to initiate phase transformation. Secondly, during unloading from

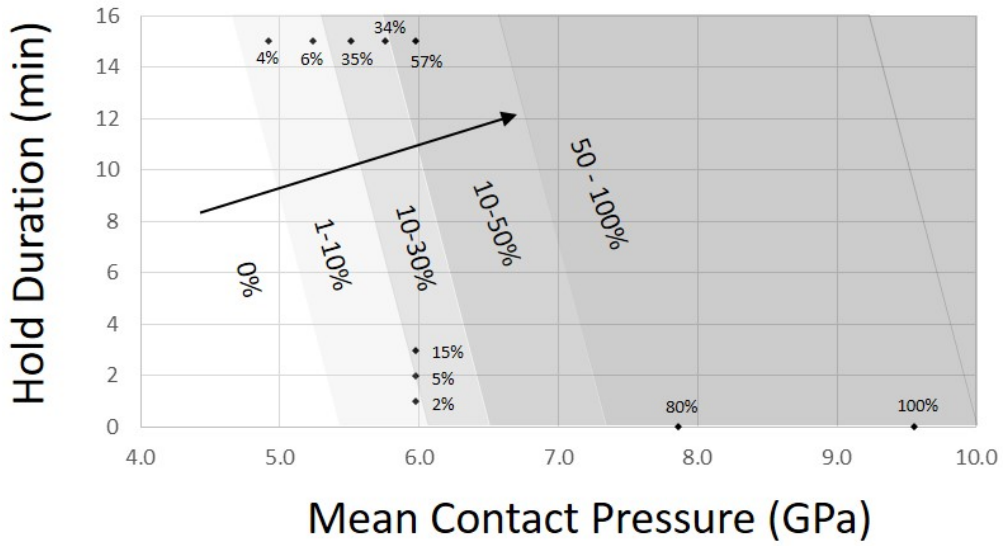

Fig. 5.20: A Pressure-Time-Transformation plot showing the percentage of indents that plastically deformed via phase transformation across a range of mean contact pressure and hold durations. Each data point is labelled with the percentage of indents that phase transformed under those conditions. Each shaded region approximates a range of transformation percentages, with an arrow indicating the direction of increasing phase transformation.

the β-Sn phase, the pressure distribution also appears to affect the transformation to either a-Si or the bc8/r8 mixed structure. Further study into these affects would allow for greater control over the end phases formed. Finally, it has been shown that both increased load and increasing hold duration lead to increased indents exhibiting phase transformation. However, further study is required to discover an ideal condition under which phase transformation is maximised relative to both elastic indents and the nucleation of crystalline indents.

Chapter 6

Annealing of the bc8/r8 Mixed Structure

This chapter investigates the annealing pathway of the bc8/r8 mixed structure that is formed via nanoindentation. The bc8/r8 structure undergoes furnace, heater stage, and laser annealing ranging from 30 to 750°C. The resulting transformed material is then characterised via Raman microspectroscopy and SADP analysis to investigate the transformation temperatures and pathways from the bc8/r8 mixed structure to the equilibrium dc-Si phase.

6.1 Introduction

The effects of annealing on the bc8/r8 mixed structure is of interest due to several reasons. Firstly, the formation of a new structure (Si-XIII) which has only been reported from annealing of this mixed phase, is of fundamental interest. Secondly, there is also a technological drive to understand the stability of both the bc8/r8 mixed structure formed using indentation and hd-Si that is formed via annealing of the mixed structure. Interest in the former is due to the potential optical properties of r8-Si [143, 144] and the recent study of bc8-Si that indicated it is a narrow band-gap semiconductor [137]. The ability to write industrially relevant regions of hd-Si onto existing Si surfaces using indentation is also technologically interesting [141]. Realisation of these goals is hindered by the lack of understanding regarding the transformation pathway of the bc8/r8 mixed structure under annealing.

6.1.1 Different Proposed Transition Pathways

As mentioned in Section 2.5, annealing of the bc8/r8 mixed structure formed via indentation has been the focus of several studies. There is a lack of consensus regarding the exact transformation pathways that occur upon annealing of the bc8/r8 mixed structure. The mixed structure is reported to transform to thermally stable dc-Si, with Si-XIII and hd-Si generally observed as intermediate phases [38, 41, 44, 83, 94]. Different indentation or annealing conditions have produced different annealing behaviour. Under certain conditions [93, 94], the intermediate phases of hd-Si and Si-XIII are not observed to form at all. Different studies that have proposed different transformation pathways are presented below and are summarised in Fig. 6.1.

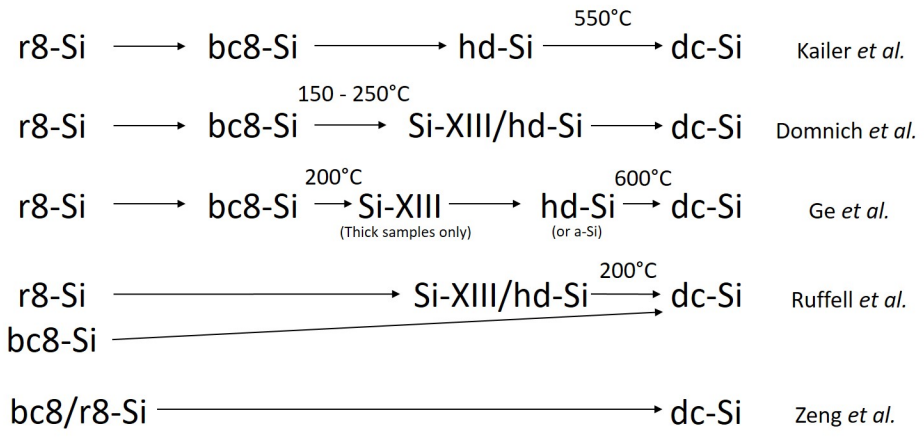

Fig. 6.1: Summary of the transformation pathways upon annealing of the indentation-induced bc8/r8 structure that have been previously reported in the literature. Where provided by the literature, the transition temperatures have also been included. Pathways are from Ref. [38, 41, 44, 83, 94]

A study by Kailer *et al.* reported the presence of hd-Si after laser annealing residual indents at "moderate" temperatures (no further information regarding the temperature was presented within Ref. [38]) and the reformation of dc-Si after furnace annealing at 550°C [38]. From these observations, they suggested a transformation pathway similar to exotic phases formed via DAC; r8-Si → bc8-Si → hd-Si → dc-Si. Domnich *et al.* additionally observed the presence of Raman peaks associated with Si-XIII alongside hd-Si after annealing between 150 - 250°C and proposed a transformation pathway of r8-Si → bc8-Si → hd-Si/Si-XIII → dc-Si [83]. These authors also reported a surprising hd-Si/Si-XIII to a-Si transformation before dc-Si in some cases. Ge *et al.* performed a study via *in situ* TEM imaging of annealed samples [44]. In this study, the indented regions were thinned in plan-view. They observed that sample thickness also impacted the transformation pathway. That is, Si-XIII was less likely to be observed and a-Si became more prevalent as the sample thickness decreased. From this study, they proposed the following transformation pathway: r8-Si → bc8-Si → Si-XIII (thick samples only) → hd-Si (or a-Si) → dc-Si. It should be noted that, within this study, a-Si was only observed in indents that already had a-Si before annealing. Thus, it is possible that the observed a-Si was pre-existing and did not form via transformation from Si-XIII as suggested in Ref. [44]. Ruffell *et al.* annealed "small" indents (made using a ∼4.2 μm radius spherical tip loaded to 80 mN) and measured the times taken for complete transformation of the bc8/r8 structure (i.e. the absence of peaks associated with bc8-Si or r8-Si within measured Raman spectra) after annealing at 100 - 450°C [93]. From this, an activation energy of 0.67 eV was measured. Further, this study reported a direct transformation to dc-Si and did not report the formation of hd-Si or Si-XIII. A more detailed study by the same authors reported the observation of

hd-Si and Si-XIII as intermediate phases within larger indents, and also indents formed in a-Si, with the end phase remaining as dc-Si in both cases [41]. They suggest that this difference may be due to the transformation being dependent on indentation conditions (i.e. phase transformed region size and surrounding material). A benefit of using an a-Si substrate is that the dc-Si observed after annealing can be assumed to arise from a pressure-induced phase transformation [1]. Such dc-Si signals from the transformed region were reported by Ruffell *et al.* to occur almost immediately after annealing to [41]. Further, they report that both hd-Si and Si-XIII transform to dc-Si after annealing at 200°C. Only dc-Si was observed after annealing at this temperature for ∼1 week. From this, the following temperature-induced transformation pathway was proposed; (i) r8-Si → bc8-Si → Si-XIII/hd-Si → dc-Si or (ii) r8-Si → Si-XIII/hd-Si → dc-Si while bc8-Si → dc-Si was suggested to occur directly. Finally, Zeng *et al.* applied high power laser annealing to the bc8/r8 structure and reported a direct transformation to dc-Si without first transforming through hd-Si or Si-XIII [94]. While not explicitly mentioned, the indentation conditions from this study by Zeng *et al.* suggest the resulting bc8/r8 mixed structure was similar to the small indents investigated by Ruffell *et al.* [41, 93]. Thus, probably as a result of differences in indentation and annealing conditions, a number of different transformation pathways can be observed on annealing.

6.1.2 Difficulties in Phase Identification

Another factor that contributes to the lack of consensus between bc8/r8 annealing studies is the similarity of hd-Si, Si-XIII, and nc dc-Si as revealed by the key techniques often used for phase identification, namely Raman microspectrocopy and SADP. The Raman peaks associated with the different exotic phases and the d-spacings that form the characteristic reflections in SADP (among other diffraction-based measuring techniques) are given in detail in Chapter 3. However, the relevant sections are reproduced here in Table 6.1 and Table 6.2 for convenience.

As Raman shift is sensitive to crystal size [208], the Raman peak from nanocrystalline (nc) dc-Si will be shifted relative to bulk dc-Si [207]. In particular, the TO peak of nc dc-Si may be down-shifted from 520 cm^{-1} such that there is considerable overlap with the main hd-Si peak at 514 cm^{-1}, potentially obscuring the presence of hd-Si. The magnitude of this shift is dependent on the crystallite size. Similarly, the primary Si-XIII peak at 497 cm^{-1} will overlap with the hd-Si peak at 496 cm^{-1}. The deconvolution of these overlapping peaks is further complicated by the presence of a-Si which has a broad Raman peak centred at ∼480 cm^{-1}.

SADP is commonly used to support Raman results in providing phase identification. However, apart from a [102] reflection, all hd-Si d-spacings observed in SADP can be attributed to other

[1] as long as the transformations to dc-Si from the crystalline phases occur at different temperatures to the a-Si to dc-Si transformation.

Raman Shift (cm^{-1})	Phase	Phonon Mode	Reference
301.9	dc	2TA	[173]
520.3	**dc**	**TO**	**[173]**
510 - 520	dc (nc)	TO	[207]
480	a-Si	Broad Peak	[45]
496	hd	TO	[174]
514	**hd**	**A_{1g}**	**[174]**
200	Si-XIII		[44]
330	Si-XIII		[44]
475	**Si-XIII**		**[44]**
497	Si-XIII		[44]

Table 6.1: The Raman peaks associated with the dc, hd, a-Si, and Si-XIII phases of Si. The primary peak of each phase is highlighted in bold text. A nanocrystalline material may result in a change in Raman shift. A relevant shift in the dc-Si TO peak is also included.

dc-Si		bc8-Si		hd-Si	
hkl	*d*-spacing (Å)	hkl	*d*-spacing (Å)	hkl	*d*-spacing (Å)
111	3.125	110	4.695	100	3.29
220	1.920	200	3.318	002	3.14
311	1.637	211	2.709	101	2.91
		220	2.346	102	2.27
		321	1.774	110	1.90
		400	1.659	103	1.77
				200	1.65
				112	1.63

Table 6.2: The *d*-spacing for dc-Si, bc8-Si, and hd-Si. The unit cell parameters used for the calculation are taken from Ref. [184] (dc-Si), Ref. [32] (bc8-Si), and Ref. [142] (hd-Si). The difference in significant figures for the values presented for hd-Si are due to the difference in significant figures in the reported unit cell parameters.

phases that may be present alongside hd-Si. That is, if no reflections at 2.27 Å are observed [2], it is possible to incorrectly classify a hd-Si sample as a mixture of dc-Si and bc8-Si instead. In particular, the [100], [002], and [101] reflections from hd-Si can easily be mistaken for the [111] reflections of dc-Si (especially if each individual reflection spot in the SADP is quite large).

It is also possible to miss Si-XIII in samples thinned for TEM. For example, it was reported that the presence of Si-XIII was dependent on sample thickness, which suggests Si-XIII may not be stable in thinned samples [44]. Therefore, the absence of Si-XIII reflections in SADP may not necessarily mean the absence of Si-XIII in the pre-thinned sample.

The results presented in this chapter aim to establish a method for unambiguous identification of hd-Si. After this, measurements from indents annealed using furnace annealing, incremental annealing, and laser annealing are presented to form a more complete picture of the transformation pathways of the bc8/r8 mixed structure. This includes measurements from previously published works that are re-analysed using this new method for identification. Such cases have been indicated in the text. In particular, the stable temperature range of hd-Si, the transformations to and from Si-XIII, and the differences between laser annealing and thermal annealing are explored.

6.2 Experimental Details

Indents were made using an Ultra-Micro-Indentation System (UMIS) 2000 using a ∼40 μm diameter spherical tip. Indentation to a maximum load of 700 mN with a load rate of ∼5 mN/s (50 increments) and an unload rate of ∼1.3 mN/s (200 increments) were undertaken. It should be noted that the UMIS load/unload rate is controlled by the number of incremental steps taken to load/unload rather than an exact load rate. These conditions were chosen as they are known to produce circular regions of the bc8/r8 structure ∼10 μm wide and ∼400 nm deep [39, 41, 93, 112]. The size of these indents is comparable to the "large" indents presented in the work by Ruffell *et al.* [41].

Furnace annealing was performed at temperatures between 50 - 750°C for 2 hours in a N_2 atmosphere unless otherwise stated. A different sample was used for each temperature. Stage annealing was performed in 10°C increments, from 30 - 240 °C, in a N_2 atmosphere. A single sample was used for the entire temperature range. The sample was brought up to temperature and held for 200 s. After each step, the sample was allowed to cool back to RT before Raman spectra were taken to prevent temperature related shifts in the spectra. Laser annealing was performed using a continuous wave (CW) 532 nm laser operating at 400 kW/cm^2 with a spot size of ∼1 μm in diameter. To ensure a relatively homogeneous transformed region, the laser

[2] Not all possible reflections are necessarily observed within every SADP

was raster scanned across the surface at a rate of 1 μm/s. All samples were imaged using XTEM and SADP after annealing.

The peak positions measured using Raman microspectroscopy were compared with those calculated using the *ab initio* framework of the density functional theory (DFT). These calculations were provided by Prof. Andres Mujica from Universidad de La Laguna as a part of a joint project.

6.3 Differentiating hd-Si and nc dc-Si

Figure 6.2 shows SADPs taken from an indent annealed for two hours at several different temperatures. Concentric circles have been used to analyse the reflections in the SADPs. Each circle corresponds to a specific d-spacing, with reflections on separate circles representing different d-spacings. Figure 6.2(a) shows a SADP taken from an indent annealed at 240°C for two hours. Careful inspection of the pattern shows a reflection corresponding to a d-spacing of 3.25 Å and another of 2.95 Å. These values are in agreement with the [100] and [101] reflections of hd-Si. Indeed, of the several exotic phases of Si known to exist in this regime, these d-spacings can only be attributed to hd-Si. Figure 6.2(a) shows that there are several further reflections in this SADP which may be attributed to either dc-Si or hd-Si. The reflections indicated by the circle corresponding to a d-spacing of 1.91 Å may be from the [110] plane of hd-Si or the [220] plane of dc-Si. Nevertheless, from the two inner circles, it is clear that hd-Si is formed in this indented region annealed to 240°C for two hours. A similar pair of inner circles is observed in the SADP taken from an indent annealed to 450°C for two hours as shown in Fig. 6.2(b). Further, the other reflections present in this image can be attributed to either hd-Si or dc-Si. This shows that hd-Si is definitely present after annealing from 240°C - 450°C for two hours but dc-Si may also be present.

A SADP taken from the indented region after annealing at 750°C for two hours is shown in Fig. 6.2(c). This image shows only a single set of reflections located at a d-spacing of ∼3.15 Å. Further, unlike the circles observed at 3.25 Å and 2.95 Å in Figs. 6.2(a) and (b), this circle intersects several more than 2-3 discrete reflections, which is suggestive of several unique crystal orientations (and crystallites) being present. This attribute is also shared by the reflections at a d-spacing of 1.90 Å and 1.60 Å. Note that the 1.60 Å d-spacing is unique to dc-Si, confirming the presence of dc-Si. At this temperature, no reflections with d-spacing unique to hd-Si (i.e. 3.25 Å and 2.95 Å) were observed.

The presence of more individual reflections at each d-spacing may be due to two potential effects. Firstly, it may be due to a decrease in crystal size which allows more crystallites of different orientation to contribute to the SADP. Secondly, it may be due to a reorientation from

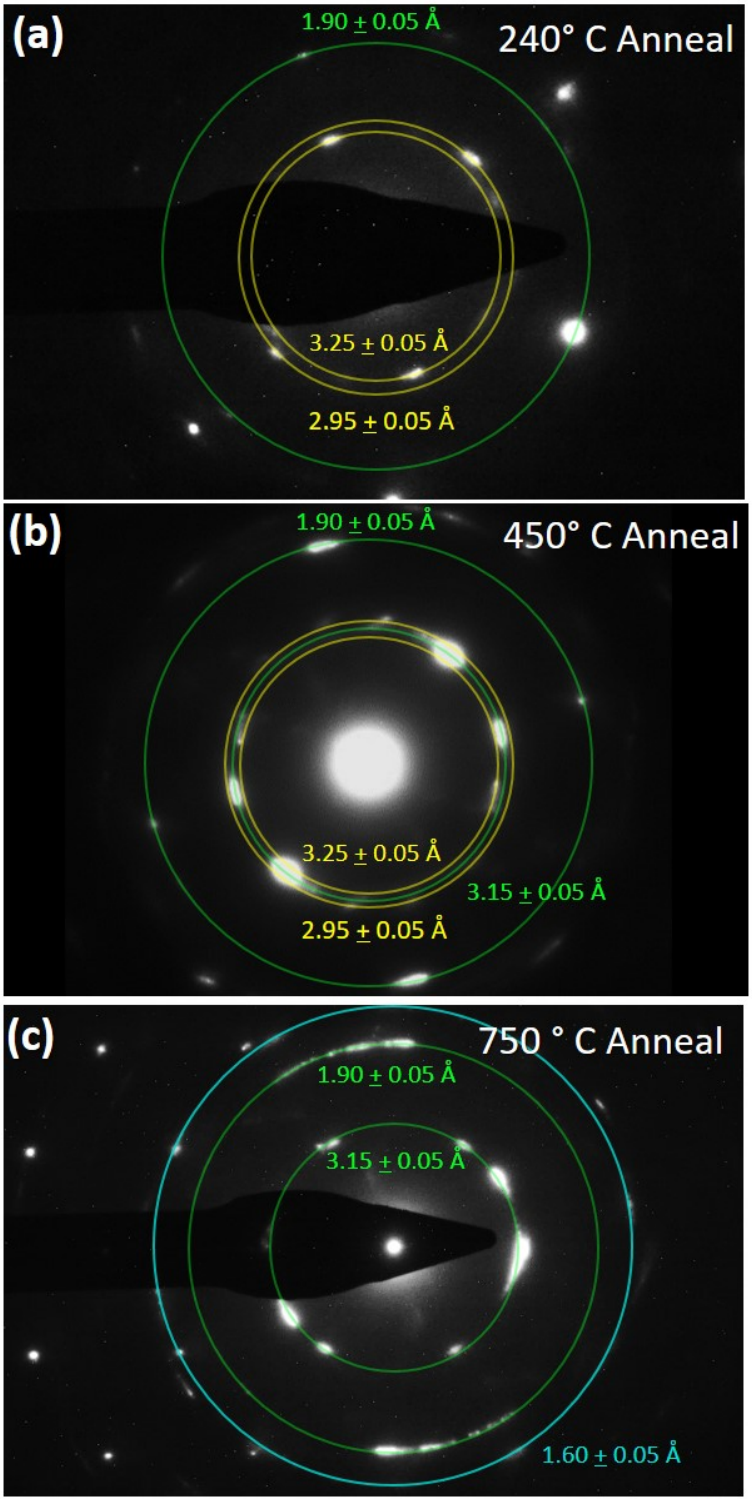

Fig. 6.2: SADPs taken from a dc-Si indent with a maximum load of 700 mN after furnace annealing at (a) 240°C, (b) 450°C, and (c) 750°C for two hours. The concentric circles have been labelled with the d-spacing to aid identification. The colour of the circle represents whether the d-spacing is associated with hd-Si (yellow), dc-Si (blue), or can potentially be associated with both phases (green).

the highly orientated bc8/r8 structure that is formed via indentation (as shown in Chapter 4) to a more randomly orientated structure. Regardless, it appears that the critical temperature for a transformation from hd-Si to dc-Si to occur lies between 450°C and 750°C. The presence of reflections uniquely associated with hd-Si in the former and the lack of these reflections in the latter would suggest that this transformation is from hd-Si to nc dc-Si.

Raman spectra were also taken from samples annealed in this regime. Figure 6.3 shows spectra taken from an indent annealed for two hours at several different temperatures. Before presenting the peaks associated with the phases found within the indent, the detection of a peak at 520 cm^{-1} must be discussed. This peak is associated with the main TO peak of dc-Si and is observed in all three spectra. When a higher numerical aperture objective or a lower wavelength excitation laser was used, this peak reduced in intensity. Thus, at least a portion of this dc-Si peak originates from the surrounding untransformed sample and cannot be used to indicate the presence of dc-Si within the indented region. The region of interest in the Raman spectra is that where nc dc-Si and hd-Si are most commonly observed, namely the 450 - 550 cm^{-1} region.

Figure 6.3(a) shows a spectrum from an indent after annealing at 240°C for two hours. This was best fitted with three peaks within the region of interest, 479 cm^{-1}, 513 cm^{-1} and 522 cm^{-1}. The peak at 479 cm^{-1} may be reasonably attributed to either the Si-XIII peak at 475 cm^{-1} or the broad a-Si peak observed at 480 cm^{-1}. The presence of other peaks associated with a-Si outside the region of interest would suggest that the latter is more likely. The peak at 513 cm^{-1} is indicative of hd-Si within the indent. Figure 6.3(b) shows a spectrum taken from an indent after annealing at 450°C for two hours. Peaks at 490 cm^{-1}, 511 cm^{-1} and 520 cm^{-1} are present within the region of interest. As before, the peak at 490 cm^{-1} is most reasonably attributed to a-Si while the peak at 511 cm^{-1} indicates the presence of hd-Si. Annealing at 750°C for two hours results in a spectrum that can be fitted with three peaks at 512 cm^{-1}, 519 cm^{-1} and 520 cm−1 as shown in Fig. 6.3(c). The peaks at 512 cm^{-1} and 519 cm^{-1} can be attributed to hd-Si and nc dc-Si, respectively. No peak associated with a-Si was observed. The drastically reduced intensity in the hd-Si peak (relative to the dc-Si peak) at this annealing temperature is in agreement with the observation made in SADP that the critical temperature for a hd-Si to nc dc-Si transformation lies between 450°C and 750°C. This is supported by the observation of a peak associated with nc dc-Si at this temperature that was also not present in the other two cases.

Together, the Raman and SADP data forms a coherent picture that suggests that hd-Si is present after annealing (of the bc8/r8 mixed structure formed using indentation) to 240°C and 450°C for two hours. Further, hd-Si is the sole crystalline phase confirmed to be found within the indented region. Signals associated with a-Si are also observed alongside hd-Si in the Raman spectra taken after annealing at these temperatures. Only after annealing to

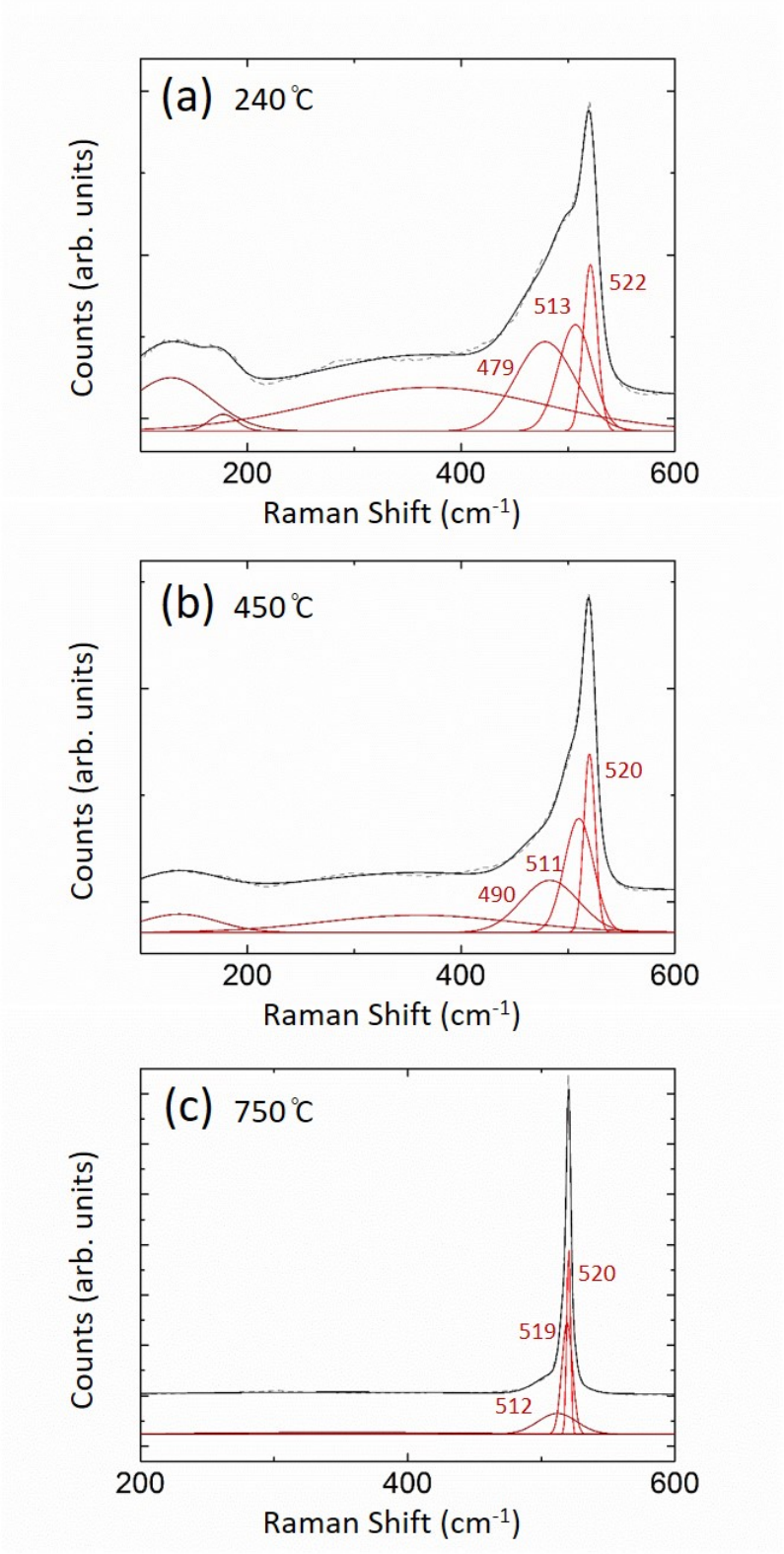

Fig. 6.3: Raman spectra taken from an indented region annealed at (a) 240°C, (b) 450°C and (c) 750°C for two hours (grey - dotted) with the peaks fitted (black). The peaks (red) have been offset for clarity and the peaks in the 450 - 550 cm^{-1} region of interest have been labelled (cm^{-1}).

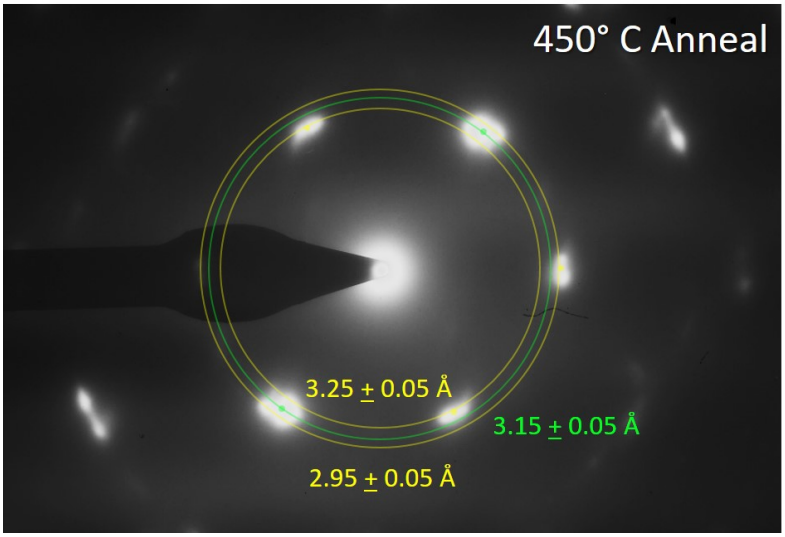

Fig. 6.4: SADP taken from an indented region furnace annealed at 450°C for 30 minutes, taken from Ref. [41]. The concentric circles have been labelled with the d-spacing that they indicate. The colour of the circle represents whether the d-spacing is associated with hd-Si (yellow) or can be associated with hd-Si or dc-Si (green).

750°C does hd-Si transform to nc dc-Si. Despite the SADP result being unable to confirm the presence of hd-Si in the 750°C case, the presence of peaks associated with hd-Si within the Raman spectrum collected from the same sample suggests that 2 hours at this temperature is insufficient time for all the hd-Si to completely transform to nc dc-Si. This suggests the critical temperature to initiate this transformation is close to 750°. A more precise calculation of the activation energy for this transformation is presented shortly in Section 6.4.1.

The above result suggests a far larger temperature regime in which hd-Si is thermally stable compared with previous annealing studies [41, 94]. It is suggested that this difference results from similarities in d-spacing and Raman shift causing hd-Si to be mistaken for dc-Si. Thus, it is possible to apply this understanding to previously published data to re-evaluate the temperature regimes suggested therein. For example, Ruffell *et al.* report that the transformed region has fully reverted to dc-Si after annealing at 450°C for 30 minutes based on SADP measurements [41]. Figure 6.4 shows SADP from Ref. [41] with added concentric circles to aid the careful d-spacing analysis. The number of reflections at each d-spacing is more in agreement with the SADP presented in this work that contains hd-Si reflections [such as Fig. 6.2(a) and (b)] than nc dc-Si [such as Fig. 6.2(c)]. Careful analysis shows that these reflections lie on three unique d-spacings, which is indicative of the presence of hd-Si as well as dc-Si.

Another example is the study by Zeng *et al.* that reports the complete absence of hd-Si within the transformation pathway [94]. In this study, indented regions were laser-annealed over 1s with laser powers up to 24 mW. Figure 6.5 shows a Raman spectrum taken from Ref. [94]

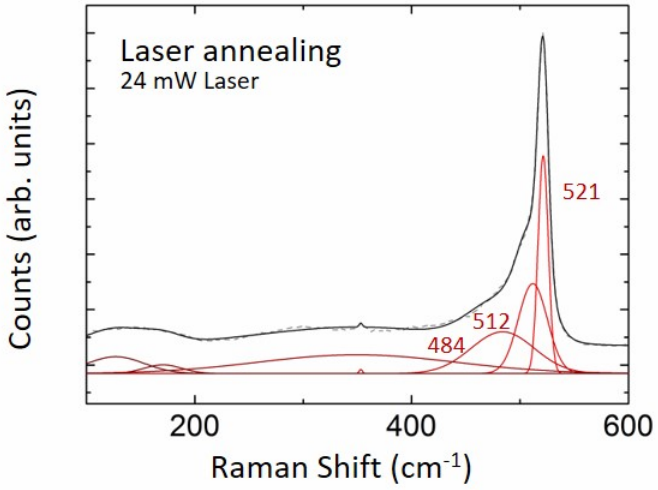

Fig. 6.5: Raman spectra taken from an indented region laser annealed using a 24 mW laser (reported as equivalent to 730°C), taken from Ref. [94]. The collected spectra (grey - dotted) has been peak fitted (black) with the peaks (red) offset for clarity. The peaks in the 450 cm^{-1} - 550 cm^{-1} region of interest have been labelled (cm^{-1}).

with the peaks fitted to aid phase identification. The region of interest can be fitted by three peaks at 521 cm^{-1}, 512 cm^{-1}, and 484 cm^{-1} which can now be attributed to the underlying dc-Si, hd-Si, and a-Si, respectively. That is, unlike the original report, it is clear that actually hd-Si is indeed observed within this indented region. Further, the presence of the r8-Si peak at 350 cm^{-1} suggests the equivalent temperature experienced is actually lower than 730°C. That is, traces of the bc8/r8 mixed structure would not be expected after annealing at such high temperatures.

Thus, this work shows that the larger temperature range at which hd-Si is stable is not in disagreement with previously published data when the older data is carefully re-analysed.

6.4 Detailed Annealing Results

The activation energy of the hd-Si to nc dc-Si transformation via annealing can now be measured. The transformation pathways from the indented bc8/r8 mixed phase during annealing are also investigated.

Temperature	Time (min)						
650°C	10	20	30	60	120	1200	
675°C	10	20	30	60	120	180	1200
700°C	10	20	50	110	230	1200	
725°C	10	20	30	60	120	240	1200
750°C	10	20	30	60	1200		

Table 6.3: The annealing temperatures and times used to calculate the activation energy of hd-Si.

6.4.1 Activation energy

Raman microspectroscopy was used to calculate an activation energy for the hd-Si to nc dc-Si transformation. Indented samples were pre-annealed at 450°C for two hours. As previously established, hd-Si is thought to be the only crystalline phase present in such annealed indents. These samples were used as the baseline for subsequent annealing to establish the activation energy for the hd-Si to nc dc-Si transition. These samples were annealed at a range of temperatures (650°C - 750°C) for up to 20 hours. Table 6.3 shows the different anneal times used for each temperature. Raman spectra were taken after each annealing step and the peaks were fitted. The 514 cm^{-1} hd-Si peak and the 521 cm^{-1} dc-Si peak were present in all spectra. The decrease in intensity of the 514 cm^{-1} hd-Si peak for several temperatures is shown in Fig. 6.6(a)-(c). Note that the maximum Raman intensity may vary between Raman measurements. Thus, the hd-Si peak intensity is measured as a fraction of the 521 cm^{-1} peak that originates from the underlying dc-Si and is relatively constant. The major source of error stems from the uncertainty involved in fitting the two slightly overlapping Raman peaks in the 450 cm^{-1} - 550 cm^{-1} region of interest.

The data points were fitted with an exponentially decaying function. From this, the time required for the hd-Si peak at 514 cm^{-1} to decay to 1/e of the initial value (k) was extracted. The Arrhenius equation characterising the phase transformation can be written as:

$$k = Ce^{\frac{E_a}{k_b T}} \tag{6.1}$$

where C is a constant, T is the temperature (in K), E_a is the activation energy of the hd-Si to nc dc-Si transformation and k_b is Boltzmann's constant. Taking the natural log of both sides gives:

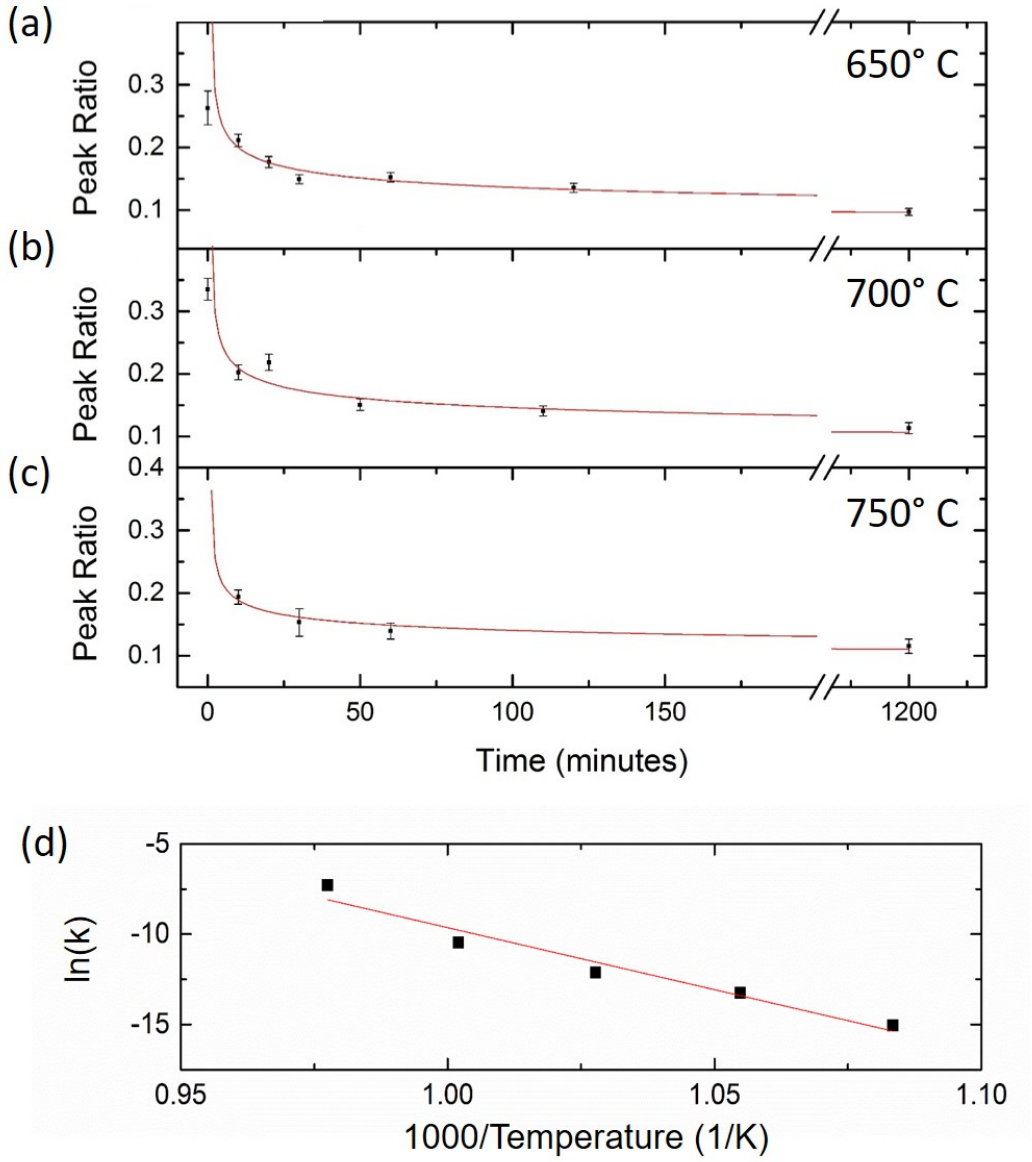

Fig. 6.6: The peak ratio between the hd-Si peak at 515 cm^{-1} compared to the constant dc-Si peak at 521 cm^{-1} from the unindented surrounding material as a function of anneal time at a temperature of (a) 650°C, (b) 700°C, and (c) 750°C. From the logarithmic fits, a k value can be calculated. (d) A plot of the ln(k) values as a function of inverse temperature. The linear fit has a gradient of -86±8 which (using Equation 6.2) gives an activation energy of 5.9±0.7 eV.

$$ln(k) = ln(C) + (\frac{1}{T})(\frac{E_a}{k_b}) \tag{6.2}$$

Figure 6.6(b) plots ln(k) as a function of 1/T. From the linear fit of this data an activation energy of 5.9±0.7 eV is calculated for the hd-Si to nc dc-Si transformation. This transformation begins at 650°C and transforms rapidly at 750°C.

6.4.2 Incremental Anneal

Figure 6.7(a) indicates the Raman peak positions for the dc-, r8-, bc8-, hd-Si, and Si-XIII phases as reported in previous studies (black) [44, 45, 173, 174]. Raman positions calculated for this work using DFT are presented alongside the reported peak positions [44, 45, 173, 174]. The DFT calculations are performed assuming no residual hydrostatic pressure. There is strong agreement between the previously reported peaks for hd-Si and dc-Si when compared to the positions calculated using DFT. There is also moderate agreement between reported and calculated peaks for bc8-Si and for r8-Si below 400 cm^{-1}. Above 400 cm^{-1}, there are three peak positions for r8-Si that are calculated but not experimentally reported. Interestingly, these three positions are similar to those predicted by Piltz *et al.* [30], suggesting that the peaks are present but are difficult to observe experimentally. Figure 6.7(b) presents Raman spectra taken from incremental heater stage annealing. The sample was annealed from 20°C (unannealed) to 240 °C in 10°C increments and a spectrum was taken (at RT) after each step. The spectra taken after the 50°C, 100°C, 150°C, and 200°C anneal are presented in black for ease of reading.

bc8 and r8

Before annealing (top spectrum), the spectrum is predominantly comprised of bc8-Si and r8-Si Raman peaks. The position of these peaks are in agreement with the previously observed experimental data [indicated in Fig. 6.7(a)]. A dc-Si peak at 521 cm^{-1} and a broad a-Si peak at 480 cm^{-1} can also be observed alongside the bc8- and r8-Si peaks. As the temperature increases, the peaks associated with bc8- and r8-Si decrease. The relative intensity between the r8 and bc8 phase can be compared by considering the ratio between the r8-Si peak at 353 cm^{-1} and the bc8-Si peak at 437 cm^{-1}. This 437 cm^{-1}/353 cm^{-1} peak ratio as a function of annealing temperature is presented in Fig. 6.7(c). The ratio remains relatively constant below 100°C. Above 100°C the 353 cm^{-1} peak decreases at a faster rate. This suggests that transformation out of the bc8/r8 mixed structure definitely occurs at 100°C. Further, it suggests that r8-Si transforms at a greater rate than bc8-Si at temperatures above 100°C.

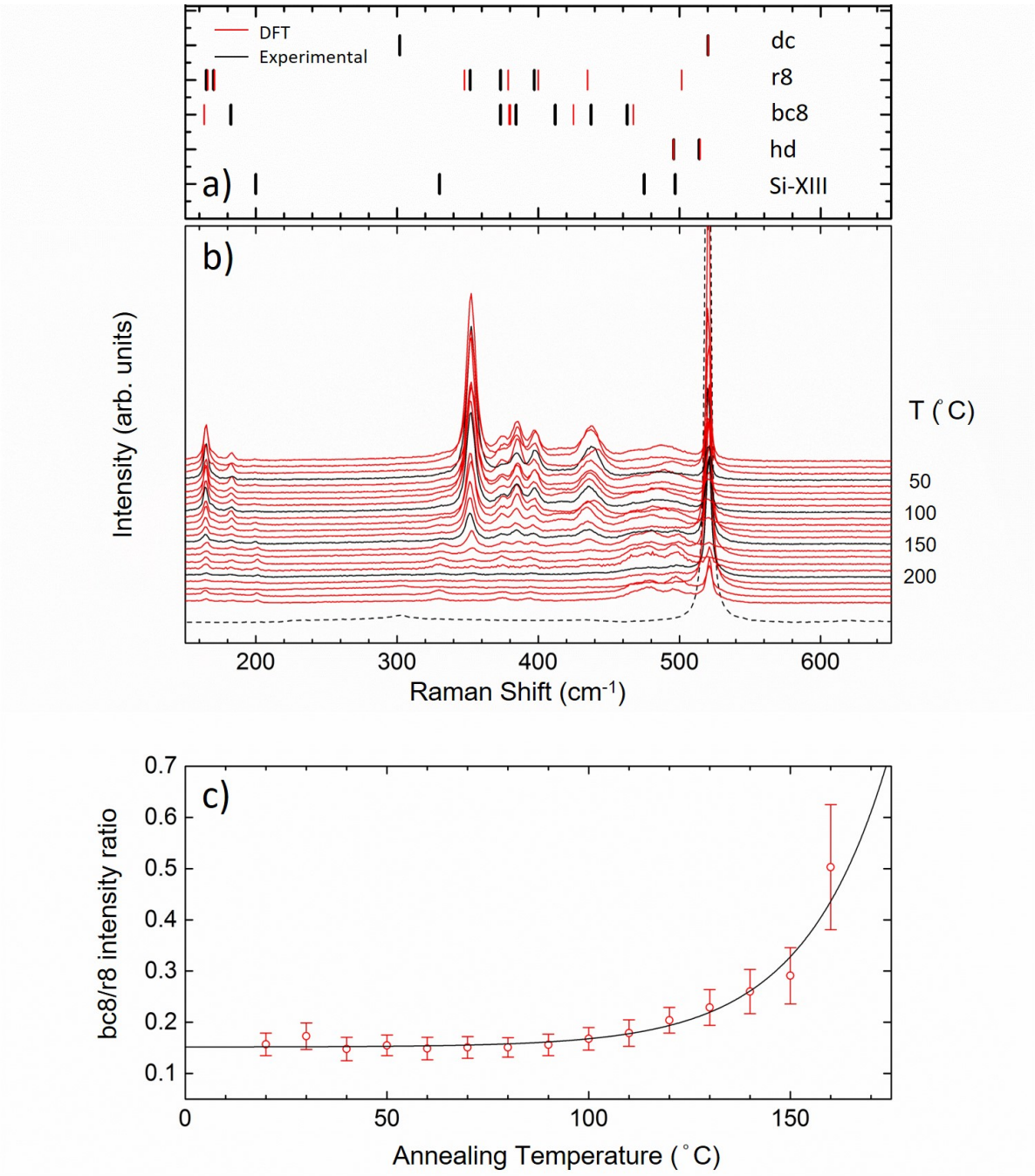

Fig. 6.7: (a) Previously published Raman peak positions from Raman studies [44,45,173,174] of indentation-induced Si phases (from Table 3.2) alongside peak positions calculated using DFT. (b) Raman spectra taken from the indented region after incremental annealing from 20°C (unannealed) to 240 °C in 10°C increments. The spectra have been offset for clarity, with the lowest temperature as the top spectrum. Multiples of 50°C are in black. A spectra of pristine dc-Si (dashed line) is also included for reference. (c) The intensity ratio between the bc8-Si peak at 437 cm^{-1} and the r8-Si peak at 353 cm^{-1} as a function of annealing temperature.

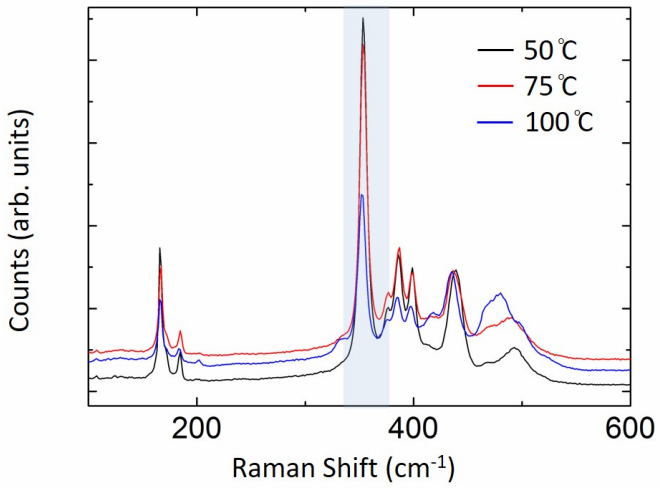

Fig. 6.8: Raman spectra taken from an indented region after furnace annealing at 50°C, 75°C, and 100°C for two hours. The spectra have been offset so that the bc8-Si peak at 437 cm^{-1} have approximately the same intensity. The r8-Si peak at 353 cm^{-1} has been highlighted.

The results do not, however, suggest that transformation of the bc8/r8 mixed structure begins at 100°C. That is, the transformation most likely begins at a lower temperature but the time spent at each temperature (200 s) during incremental annealing may be insufficient for the transformation to be noticeable in a Raman spectrum. Figure 6.8 shows averaged Raman spectra taken from indents furnace annealed at 50°C, 75°C, and 100°C for two hours. The spectra have also been normalised, so that the bc8-Si peaks at 437 cm^{-1} all have roughly the same intensity. There is also a broad peak at ∼490 cm^{-1} alongside the bc8- and r8- peaks. This is most likely due to the presence of a-Si. Although the commonly observed peak for a-Si is observed at 480 cm^{-1}, such spectra have been taken from a-Si formed via ion implantation. Pressure induced a-Si (such as that found in these residual indents) have been reported to have a peak that can be up-shifted to as high as ∼500 cm^{-1} [42]. Even after the extended annealing times, it is evident that the bc8- to r8-Si ratio does not vary much from 0.15 after annealing at 50°C and 75°C. It is only after annealing at 100°C that the r8-Si peak at 353 cm^{-1} decreases. This supports the idea that transformation from the bc8/r8 mixed structure begins at 100°C and no significant transformation is occurring at 75°C. A Si-XIII peak at 475 cm^{-1} is also present in the spectra after annealing at 100°C. This may suggest that the distorted r8-Si that is formed via indentation (with the elongated unit cells reported in Chapter 4) transforms to Si-XIII directly without transforming to bc8-Si as an intermediate step.

Si-XIII and hd-Si

Now that the Raman signal associated with bc8-Si and r8-Si has been discussed, the Raman peaks associated with hd-Si and Si-XIII will be presented. Additional peaks can be observed around 450 - 520 cm^{-1} in Fig. 6.7(b). Before annealing, the dominant peak within this range is a broad peak at ~485 cm^{-1} which is attributed to a-Si. After annealing to 100°C, this peak down-shifts gradually to ~480 cm^{-1} before splitting into two distinct peaks after annealing at 160°C. These peaks remain even after the final step of the incremental anneal at 240°C, with their final positions being 477 cm^{-1} and 498 cm^{-1}. This behaviour is consistent with the suggestion above that, at this temperature, r8-Si begins to transform to Si-XIII with peaks at 475 cm^{-1} and 497 cm^{-1}. As the peak at 475 cm^{-1} is more prominent, it appears first after lower temperature anneals. This causes the a-Si peak to appear to gradually down-shift. As the two Si-XIII peaks continue to grow, both appear as distinct peaks that are separated from both the a-Si broad peak and each other. Their presence after the entire incremental annealing process suggests that Si-XIII remains after annealing at 240°C for 200 s, despite no longer being present after annealing at this temperature for two hours [as shown in Fig. 6.3(a)]. It is not readily apparent whether hd-Si is present within any of the spectra in these anneals. While it is possible that peaks associated with hd-Si are present at 496 cm^{-1} and 514 cm^{-1}, the proximity of the more prominent Si-XIII peak at 497 cm^{-1} makes it impossible to definitively state that hd-Si is present. Peak fitting, similar to that performed on the Raman spectra shown in Fig. 6.3, was attempted but this was ultimately unsuccessful due to the presence of the extra Si-XIII peaks.

A SADP of the indented region after incremental annealing was also taken. This is shown in Fig. 6.9(a). The reflections lie on two distinct d-spacings, at 3.15 Å and 3.25 Å, which indicate the presence of hd-Si (as established in Section 6.1.2). Thus, hd-Si is indeed present after incremental annealing, despite hd-Si peaks not being readily evident in the Raman spectra. There are also reflections at a d-spacing of 4.4 Å and 4.7 Å which indicate the presence of Si-XIII. Figure 6.9(b) shows a SADP taken from the same selected area on the same sample 20 days after the image in (a). Interestingly, the d-spacings that were associated with Si-XIII are no longer present. Instead, the a-Si signal appears stronger. This is in agreement with the observation by Ge *et al.* who reported that Si-XIII is not stable in a thinned sample and may transform to a-Si. More importantly, this suggests that Si-XIII does not decay to hd-Si. Thus, the presence of hd-Si reflections in SADP taken from a thinned sample is indicative of the presence of hd-Si in the sample before thinning. The transformation pathways that are suggested by this incremental annealing are discussed in greater detail in Section 6.5.

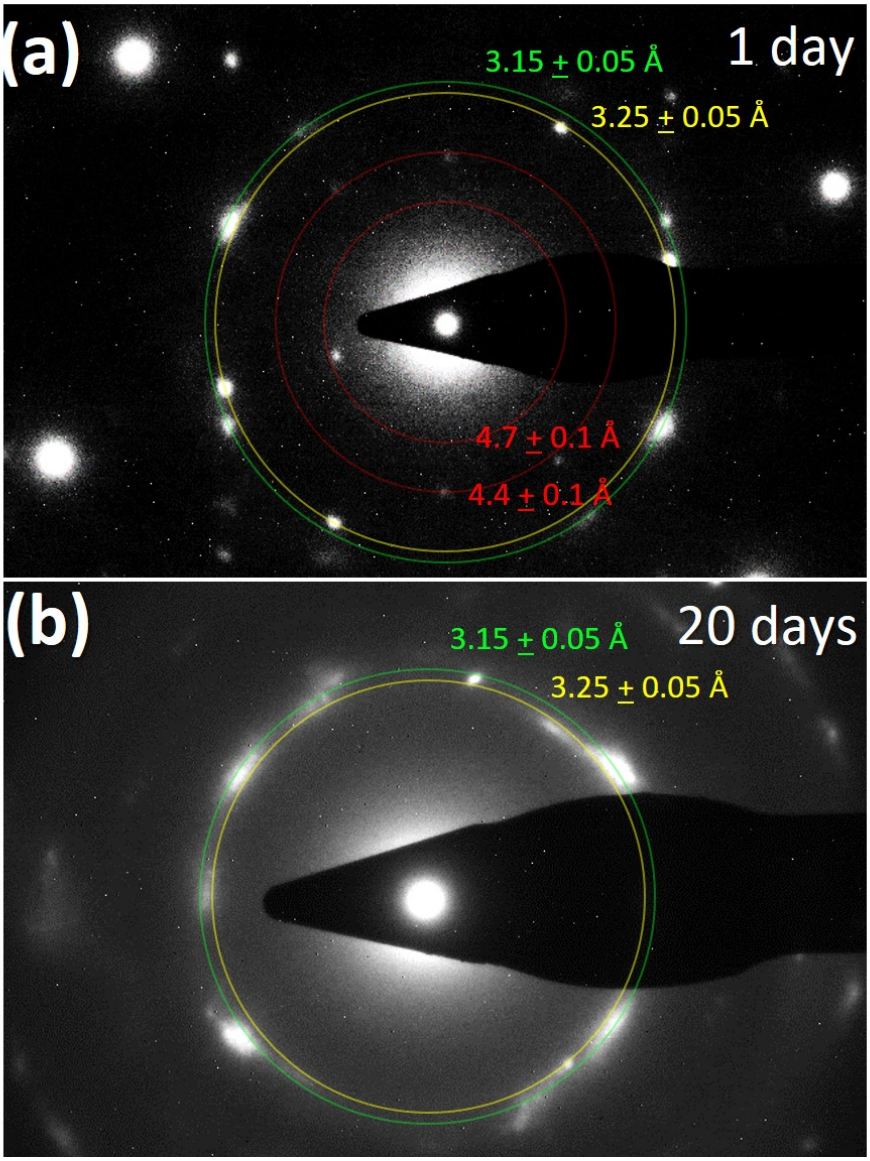

Fig. 6.9: SADP taken from an indented region after incremental annealing up to 240°C (a) 1 day after FIB thinning and (b) 20 days after FIB thinning from approximately the same selected area. The concentric circles have been labelled with the d-spacing that they indicate. The colour of the circle represents whether the d-spacing is associated with hd-Si (yellow), dc-Si or hd-Si (green), or Si-XIII (red).

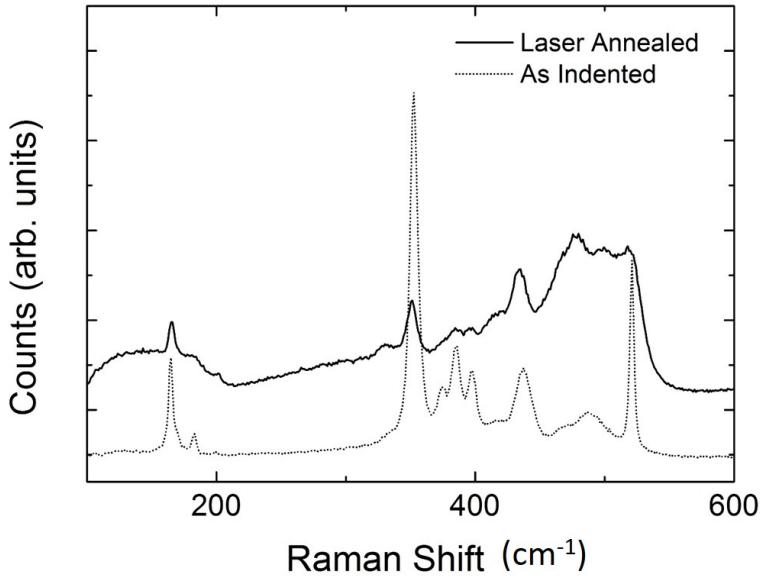

Fig. 6.10: Raman spectrum taken from an indented region after laser raster annealing. A spectrum taken from an as-indented indent has been included for reference.

6.4.3 Laser Annealing

The Raman microspectroscopy study that reported laser annealing may change the transformation pathways of the bc8/r8 mixed structure suggested that the structure may transform directly to dc-Si, completely bypassing the intermediate phases of hd-Si and Si-XIII that are observed in traditional thermal annealing [94]. However, this previous study only presents results from indented regions annealed with high laser powers (12 mW - 24 mW). In this section, data collected from the indented region after laser annealing at lower power is presented.

Figure 6.10 shows a Raman spectrum taken from an indent after laser raster annealing (as described in the experimental section of this chapter). Raman peaks associated with the bc8/r8 mixed structure, such as the 353 cm^{-1} r8-Si peak and the 437 cm^{-1} bc8-Si peak, remain present after one scan of laser annealing. Further, multiple peaks at ~475 cm^{-1}, ~485 cm^{-1}, ~500 cm^{-1}, and ~520 cm^{-1} are also present which indicate the presence of both the Si-XIII and hd-Si phases.

Figure 6.11 shows a SADP that was taken from the same indented region. Reflections at 4.4 Å, 2.95 Å, and 2.70 Å indicate the presence of Si-XIII, hd-Si, and the bc8/r8 mixed structure as these d-spacings are unique to their respective phase. This confirms that, at lower laser power, the intermediate hd-Si and Si-XIII phases can indeed be formed.

An equivalent thermal annealing temperature for the performed laser annealing was calculated

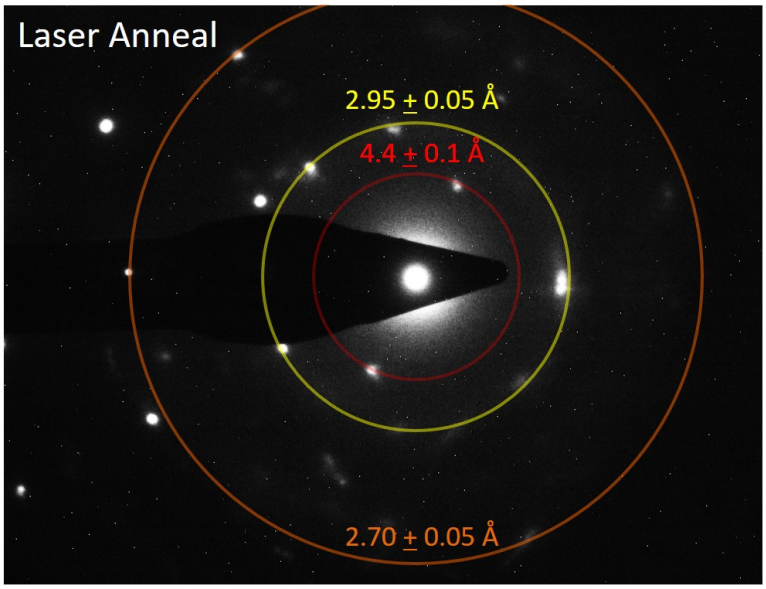

Fig. 6.11: SADP taken from an indented region after laser raster annealing. The concentric circles have been labelled with the d-spacing that they indicate. A reflection unique to Si-XIII (red), hd-Si (yellow), and bc8-Si (orange) has been presented.

using three separate methods. Firstly, the temperature dependent shift of the dc-Si TO peak at 521 cm^{-1} can be used. This shift is governed by the equation $d\omega/dT = -0.022cm^{-1}.K^{-1}$ [209] and suggests an equivalent thermal annealing temperature of 195°C. Secondly, with the presence of the bc8- and r8-Si peaks, the intensity ratio between the bc8 and r8 peaks can be determined. This value can be compared to the ratio presented in Fig. 6.7(c) for the incremental annealing case. Using this method, a temperature of ∼190°C can be calculated. This is in good agreement with the temperature calculated from the dc-Si peak shift. The third method relies on the temperature-dependent peak shift of the r8-Si peak at 353 cm^{-1} [42]. Using this method, the calculated temperature for the laser annealing is ∼60°C. This is in clear disagreement with the other two methods for calculating the temperature. It should be noted that neither Si-XIII or hd-Si was observed from thermal annealing below 100°C but were observed after laser raster annealing. This suggests that there is a degree of unreliability within methods used to calculate equivalent thermal annealing temperature that should be considered when determining phase transformation temperatures/pathways under laser annealing.

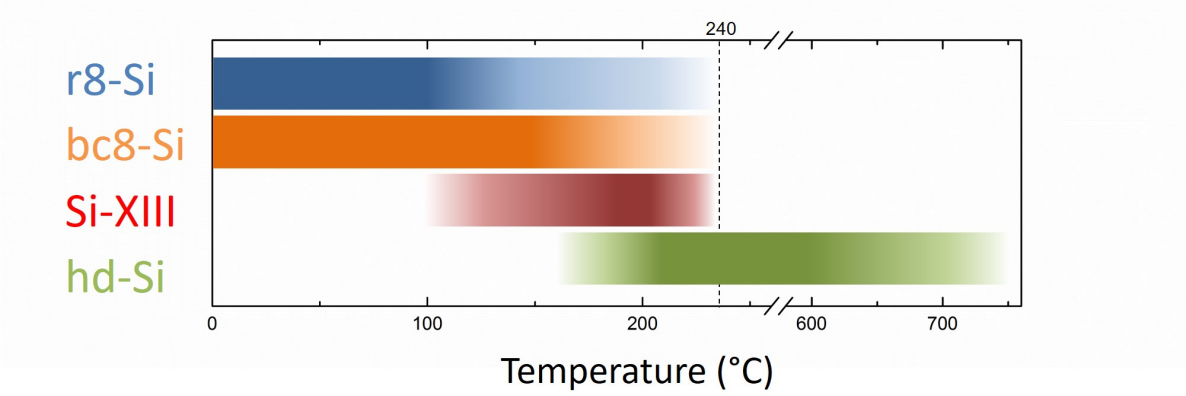

Fig. 6.12: A plot showing the presence of the exotic Si phases after thermal annealing at varying temperatures. Fading colour represents temperatures at which the phase is gradually transforming. The temperature at which the bc8- to hd-Si transformation begins is an estimate only.

6.5 Discussion

6.5.1 Transformation Pathway

With the results presented above, it is now possible to attempt to present the transformation pathways from the bc8/r8 mixed structure to dc-Si via annealing. Figure 6.12 plots the temperatures at which each phase is completely/partially stable while Fig. 6.13 is a schematic showing the most likely transformations that occur. In Fig. 6.12, a phase is considered to transform "rapidly" at a given temperature if annealing at that temperature results in the complete transformation of that phase within two hours. This value is arbitrary but allows comparison between different transformations in the absence of an activation energy for several of the transformations.

Consider first the r8-Si phase in the initial bc8/r8 mixed structure. It was shown that the distorted r8-Si in the bc8/r8 mixed structure started to phase transform to Si-XIII at 100°C but there is insufficient data in this chapter to establish when r8-Si fully transforms to Si-XIII. Ruffell *et al.* observed the presence of r8-Si peaks in Raman spectra after annealing at 200°C for two hours [41] but this work showed that no r8-Si remained after annealing at 240°C for two hours. Thus, r8-Si transforms rapidly at some point in the 200°C - 240°C regime. Si-XIII first appears at 100°C and is also reported to be partially stable at 200°C [41,45], disappearing only after annealing at this temperature for ∼1 week. Furthermore, it was shown that Si-XIII transforms to hd-Si, with complete transformation occurring after annealing at 240°C for two hours. Finally, hd-Si further transforms to nc dc-Si with an activation energy of 5.9±0.7 eV, beginning at 650°C but transforming rapidly at ∼750°C.

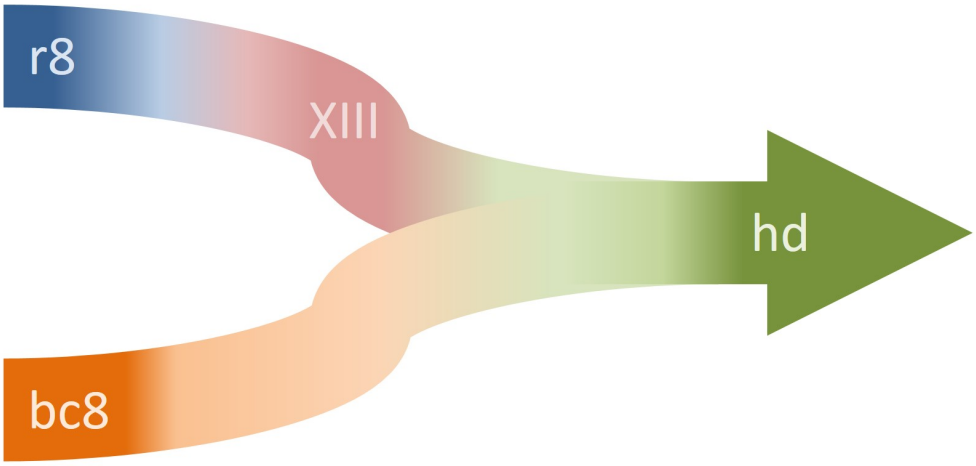

Fig. 6.13: A schematic of the proposed transformation pathways of bc8-Si and r8-Si (in the bc8/r8 mixed structure formed via indentation) under annealing.

The transformation temperatures for bc8-Si are less clear compared to r8-Si. The Raman results suggest that bc8-Si starts transforming at a higher temperature than r8-Si. However, it is not known with complete certainty whether strained bc8-Si transforms directly to hd-Si or if it first transforms to Si-XIII as an intermediate phase. Two factors would suggest that the direct transformation to hd-Si is more likely. Firstly, it is proposed that the transformation to Si-XIII is driven by the unit cell distortion that is present after uniaxial unloading. The r8-Si to Si-XIII transformation is likely to relieve the residual strain, thus the subsequent transformation of bc8-Si may be less likely to transform to Si-XIII if strain is relieved. Secondly, bc8-Si was reported to be the most stable crystalline phase within the indented region after extensive thinning [44]. Therefore, it is unlikely that the more stable bc8-Si would transform into a less stable Si-XIII. Regardless of the transformation pathway, bc8-Si was also found to transform rapidly at some point between 200°C and 240°C, resulting in hd-Si.

Si-XIII

The annealing transformation pathway proposed in this work suggests that the r8-Si component of the bc8/r8 mixed structure formed by indentation almost certainly transforms to Si-XIII after annealing. This is in contrast to many earlier studies that suggest an r8-Si to bc8-Si transformation occurs during annealing. However, most earlier studies assume that a (β-Sn)-Si $\rightarrow$ r8-Si $\rightarrow$ bc8-Si transformation is occurring during unloading in the indentation case analogous to the transformations that have been found to occur during unloading of DAC-pressurised samples. Kailer *et al.* [38] arrived at this assumption based on a study by Piltz *et al.* [30] that reported traces of r8-Si within the material recovered from a DAC which was reduced by annealing to 100°C. More recent *in situ* Raman studies suggest that the bc8-Si

and r8-Si in the mixed structure appear simultaneously in contradiction to this assumption of sequential transformation [43, 91].

It is proposed, then, that the different annealing behaviour of the mixed phase, compared to DAC transformation pathways, is due to the presence of residual stress within the indented region. That is, r8-Si to Si-XIII is a more energetically favourable transformation due to the ability for this transformation to relieve the residual stress within the indented region. This idea of residual stress being relieved during temperature-induced transformations is supported by the DFT calculations. It was shown in this chapter that, by calculating the peak positions at 0 GPa using DFT, there is a good agreement between the observed and calculated values for hd-Si. While the peak positions for bc8- and r8-Si are in moderate agreement, the fit is clearly not as good as that of hd-Si. This is consistent with the proposal that the r8-Si and bc8-Si peaks are experiencing residual stress that is relaxed during the annealing. It is proposed that this relaxation of residual stress may be the reason behind the r8-Si to Si-XIII transformation that is only observed in indentation studies.

The results in this chapter (such as the result shown in Fig. 6.9) also suggest that Si-XIII is not stable when thinned (for TEM examination, for example). Further, it transforms to hd-Si when annealed but appears to transform to a-Si when thinned. This is in agreement with Ge *et al.* who reported that the transformation pathway and the temperatures at which the transformations occur were affected by the thickness of the sample during *in situ* annealing of thinned XTEM samples [44]. Further, the disappearance of Si-XIII in a thinned sample suggests, once again, that the presence of this phase is connected to the presence of residual stress within the indented region. When this stress is removed during thinning, Si-XIII becomes unstable and slowly transforms to a more stable phase at room temperature (in this case a-Si).

hd-Si

From the results presented in this chapter, the hd phase has been shown to be stable across a far larger temperature range than previously reported. It has previously been reported to be partially stable at 200°C [41] and transform rapidly at 550°C [38]. In this work, hd-Si reflections was first observed alongside Si-XIII in SADP after annealing at 240°C for 200 s. After annealing at 240°C for two hours, hd-Si was shown to be the only crystalline phase present within the transformed zone. It only begins transforming at 650°C and did not anneal rapidly until ∼750°C. Interestingly, this indicates that there is a temperature range (240°C - 650°C) where hd-Si is both stable and the only crystalline phase present. This is particularly important when considering the potential for exploitation of hd-Si for technological applications [141]. Many industrial processes of a-Si-based devices and even for some processing

schedules for dc-Si devices involve treatment at between 450°C (the temperature required for relaxation of a-Si [108]) and 700°C. Thus, the observation that hd-Si is thermally stable at this temperature suggests that this phase could be readily integrated into existing industrial processes.

6.5.2 Experimental Variations

The transformation pathways proposed above was determined using results from thermal annealing of large transformed regions formed via indentation. However, several observations presented here are not exclusive to this experimental set-up. In this section, the relevance of these observations in the larger context of annealing exotic phases of Si is considered.

Smaller Indented Regions

The indented regions presented in this work are "large" indents using the terminology of Ref. [41]. Ruffell *et al.* reported that "small" indents did not follow the same transformation pathway, with the bc8/r8 mixed structure transforming directly to dc-Si [93]. Using the method for more accurate identification of hd-Si (presented in Section 6.1.2), the data taken from small indents can be reassessed. This reassessment suggests that the previous reports of transformation to dc-Si were wrong and it was actually a transformation to hd-Si. However, no signs of Si-XIII were reported from within these small indents. It may be possible that Si-XIII is present but the regions are so small that the signal from the non-dominant Si-XIII is not significant. Another possible reason that Si-XIII might not be reported is that small transformed regions of the bc8/r8 structure surrounded by dc-Si are less likely to sustain residual stress than larger regions.

Laser Annealing

It has also been reported previously that laser annealing, in contrast to thermal annealing, of the bc8/r8 mixed structure results in a different transformation pathway [94]. This reported pathway, most notably, does not include either Si-XIII or hd-Si as intermediate phases. The results presented in this work show that these phases are indeed observed after laser annealing. It is suggested that this discrepancy is again due to the difficulty in distinguishing hd-Si from dc-Si and also the difficulty in estimating an equivalent thermal annealing temperature from laser annealing.

Due to the ease with which hd-Si may be mistaken for dc-Si, Raman spectra collected from an indented region that was laser annealed with a 24 mW (3000 kW/cm^2) laser over 1 s (from

Ref. [94]) was reassessed in this work (in Fig. 6.5). The Raman peaks associated with hd-Si were reported (alongside trace peaks associated with r8-Si). It was reported that these hd-Si peaks appeared to be stable over subsequent anneals. This suggests that hd-Si is stable during 1 s duration, 24 mW laser anneals.

Such laser annealing conditions were reported to be equivalent to 730°C (based on the temperature dependent shift of the dc-Si TO peak at 521 cm^{-1}) [94]. Results presented within this work suggest that hd-Si is not stable at this temperature. However, the r8-Si peak at ~353 cm^{-1} was also reported to be persistent over several 1 s duration 24 mW laser anneals, indicating that r8-Si was also stable under such laser annealing. This strongly suggests that the equivalent thermal annealing temperature experienced by the transformed region is much lower that the estimated 730°C in this previous work.

Several different methods for calculating the equivalent temperature were also presented in this chapter. Using the ratio between the 353 cm^{-1} and 437 cm^{-1} Raman peaks or the temperature-dependent shift of the dc-Si peak at 521 cm^{-1} to recalibrate the temperature gave better agreement with the present work.. However, using the temperature-dependent shift of the r8-Si peak at 521 cm^{-1} gave a significantly lower temperature. One possible explanation for this difference is that, in laser annealing, the heat is not distributed homogeneously. That is, the temperature dependent shift of the r8-Si peak is less than the shift of the dc-Si peak because the transformed region may be experiencing lower temperatures than the surrounding dc-Si due to a higher thermal conductivity of the mixed phase, noting bc8-Si is reported to have high thermal conductivity [137]. This suggests that the equivalent thermal annealing temperature determined using the 521 cm^{-1} TO peak of the surrounding dc-Si is not representative of the temperature experienced by the transformed region. Taking these recalibrations relating to previous work and the present results into account, laser annealing results in similar transformation pathways at similar temperatures to thermal annealing. That is, at lower laser power the bc8/r8 transforms to hd-Si and Si-XIII. At higher laser power, the Si-XIII further transforms to hd-Si which remains stable across a large temperature range.

DAC-induced Pressure

The predominantly bc8-Si material formed in a DAC is found to transform to hd-Si after annealing at 200°C [32]. This hd-Si further transforms to dc-Si after annealing at 750°C [67]. The results presented in this chapter suggest that annealing of the bc8/r8 mixed structure formed using indentation does not follow a similar transformation pathway. It is proposed that a key difference between indentation-induced and DAC pressure-induced phase transformation is the residual strain along the axis of indentation that causes unit cell distortion (as shown in Chapter 4). The impact of this residual stress in the bc8/r8 mixed structure's annealing

pathway should be considered.

The observation of the novel phase, Si-XIII, is unique to annealing of indentation-induced bc8/r8 structures. Evidence for an r8-Si to Si-XIII transformation beginning at 100°C is discussed. When produced in a DAC, r8-Si has not been reported to transform to Si-XIII. Instead, r8-Si held at ∼10 GPa is known to transform directly to dc-Si after annealing at 255°C [45]. It was suggested in this work that the r8-Si to Si-XIII transformation is observed only in indentation studies due to the residual strain within the indented region. Further, it is proposed that this transformation occurs in order to relieve the residual strain.

There is good agreement between the experimentally observed and theoretically calculated (via DFT) Raman peak positions for hd-Si. This suggests that there is no significant unit cell distortion of the hd-Si formed by annealing the bc8/r8 mixed structure. It has been shown that this hd-Si further transforms to (nc) dc-Si after annealing at 750°C, the same temperature observed in a DAC [67].

6.6 Summary

In this chapter, a new method for unambiguously identifying the hd-Si to nc dc-Si transformation has been presented. In SADP, the presence of multiple unique d-spacings are found to be indicative of hd-Si. A singular d-spacing of 3.15 Å coupled with a sudden increase in reflections at the d-spacings associated with dc-Si suggests that a transformation to nc dc-Si has occurred. This is supported by Raman spectra, carefully fitted, showing that the often observed asymmetrical dc-Si peak at 521 cm^{-1} can be de-convoluted. Thus, the contributions of hd-Si and nc dc-Si can be determined.

The stability of Si-XIII is also discussed. It is suggested that Si-XIII is unique to indentation induced phase transformation experiments due to a significant amount of residual uniaxial strain being present in the indented region. This is supported by the observation that, after thinning, the Si-XIII became unstable and transformed to a-Si. This dependence on residual stress is also suggested as the reason why Si-XIII was not observed in smaller indents.

Combining the above observations, a new transformation pathway for the bc8/r8 mixed structure under annealing is presented. The results suggest that r8-Si transforms independently of bc8-Si. THe r8 phase transforms first to Si-XIII at 100°C which then transforms to hd-Si at ∼200°C. Similarly, bc8-Si most likely transformed to hd-Si at ∼200°C, consistent with DAC findings. The hd phase is found to be more thermally stable than previously reported, with a high activation energy of 5.9±0.7 eV, and only completely transforming to nc dc-Si at ∼750°C. A similar transformation pathway is observed for the bc8/r8 structure under laser annealing.

The increased thermal stability of hd-Si is encouraging for exploiting this exotic phase for technological applications. However, there is potential for further study of r8-Si and Si-XIII, especially in the 100°C - 200°C temperature regime where many simultaneous transformations are occurring. Such studies may uncover regimes where a sole crystalline phase (r8 or Si-XIII) is present. This work suggests that such a study would also require an improved understanding of the residual stress that appears to be characteristic of indentation-induced phase transformations.

Chapter 7

Concluding Remarks and Future Direction

In this thesis, several aspects of the bc8/r8 structure of Si formed via indentation have been investigated. In this final chapter, the key conclusions from this work are summarised, followed by a broad discussion of the implications of these findings for the field. Finally, possible future directions are presented.

7.1 Key Conclusions

In this work, the processes through which phase transformations can be induced via indentation have been comprehensively investigated. The phase transformation of dc-Si under indentation pressure was shown to be a nucleation limited process. Plastic deformation of dc-Si by phase transformation was found to compete with another nucleation limited plastic deformation mechanism, the nucleation and propagation of crystalline defects. It was discovered that two distinct pathways for plastic deformation were possible. Interestingly, within one of these pathways, phase transformation was the sole form of deformation at lower loads and remained the dominant form of deformation even when other mechanisms began to be observed at higher loads. It was shown that reducing the maximum load or increasing the time held at maximum load promoted phase transformation.

The promotion of phase transformation is desirable due to the formation of a mixed bc8/r8 structure upon pressure unloading. This indentation-induced bc8/r8 structure was found to consist of ∼70% r8-Si, with the remainder being bc8-Si. Interestingly, XRD analysis showed the bc8/r8 structure that is formed via indentation exhibits a significant distortion of the unit cell. The unit cell was elongated along the axis of indentation, resulting in a reduction in volume equivalent to compression to ∼4 GPa. It was proposed that this unit cell distortion is evidence of the residual stress that allows the observation of significant amounts of r8-Si in the indented Si.

Further analysis showed that this predominantly r8-Si structure has an increased optical absorption compared to dc-Si. The absorption coefficient of nanocrystalline r8-Si was shown to be larger than the coefficient predicted by Ref. [143], which may be due to the polycrystalline nature of the measured sample. Interestingly, the bc8/r8 mixed structure was also found to

have a similar absorption coefficient across the photon energy range investigated. This result supports the proposal that r8-Si, even when formed as a portion of a bc8/r8 mixed structure, is a promising material with potential for photovoltaic (PV) applications.

The thermal stability of the bc8/r8 structure was also explored. At 100°C, the r8-Si formed via indentation transforms to Si-XIII, a Si phase with an unknown structure. It was proposed that this novel phase is only present within indentation studies because the distorted r8-Si unit cell transforms more favourably to Si-XIII rather than bc8-Si or dc-Si (as the conventional annealing pathway would suggest). It was further suggested that this transformation releases the residual stress from the bc8/r8 structure. Thus, the bc8-Si portion of the mixed structure was suggested to transform directly to hd-Si, without first transforming to Si-XIII, in a similar manner to that reported in DAC experiments. Si-XIII was also observed to transform to hd-Si, which was found to be the sole crystalline phase present within the indented region after annealing at 240 - 650°C. This is of particular interest as it shows that hd-Si regions formed in indentation experiments are stable at 450°C, a temperature that may be used in industrial processes to relax a-Si-based devices.

7.2 Broader Perspective and Future Directions

In light of the key conclusions, a discussion of the implications of this expanded understanding of exotic Si phases formed via indentation is now presented. It has been known for decades that many different phases of Si can be formed by simply applying high pressure to dc-Si . This current work has focused on the phases that are formed via indentation-induced pressure application. The following section aims to return to the questions posed in the introduction of this thesis in light of the findings within this work. The three key questions can be summarised as follows. 1) How can the results of this thesis add to the overall framework understanding of transformation in Si? 2) How technologically useful are the properties of the r8-Si found within the mixed structure? 3) How can this transformation process be scaled up to be technologically viable? These three questions are addressed in the following three sections.

7.2.1 A Framework for Phase Transformation

Phase transformations between Si phases can be observed during loading, unloading, and during thermal annealing. In this section, a framework for understanding the transformations in Si under indentation is presented and the mechanisms within each stage that determine the sample's response are discussed.

Pressure Loading

A transformation from dc-Si to a denser metallic structure, most likely (β-Sn)-Si, occurs upon loading. This is commonly observed alongside crystalline defects within the surrounding dc-Si material. The question of incipient plasticity (i.e. which plastic deformation occurs first) during indentation of dc-Si has been resolved within this work. Either phase transformation or the nucleation of crystalline defects in the underlying dc-Si can occur first due to the nucleation limited nature of both mechanisms, forming two distinct plastic deformation pathways. In particular, before incipient plasticity, there is a clear separation between the point of maximum hydrostatic pressure (which promotes phase transformation) and the point of maximum shear stress (which promotes defect nucleation). This allows both nucleation-limited mechanisms to have the potential to occur first at different points within the sample. Indents that deform first via phase transformation were shown to form larger, more uniform regions of bc8/r8, even in a maximum load regime where both mechanisms are present.

Furthermore, while phase transformation is predominantly driven by hydrostatic pressure, the observation of "buried layers" (phase transformation that nucleated a little below the sample surface) indicates that phase transformation does not necessarily nucleate first at the point of highest hydrostatic pressure. Instead, it may involve regions where there is interplay between the induced hydrostatic pressure and shear stress. Indeed, this observation is supported by a number of modelling studies [99, 100]. The idea of several nucleation sites for the (β-Sn)-Si crystallites suggests that this phase that is formed during pressure loading is most likely to be polycrystalline, with as many crystallites as there are nucleation sites. Further, the impact of holding the sample at maximum load on elastic/plastic response and the absence of a pop-in during load (which signify a sudden density change) supports the idea that this transformation is sluggish in nature. That is, β-Sn is slow to nucleate at these sites as well as slow to grow once nucleated. It is interesting to consider whether these crystallites further separate into smaller crystallites (due to crystallite reorientation or decreasing density) upon pressure unloading.

The pressure distribution may also play a significant role in both the determination of deformation pathway as well as the shape of the transformed region when phase transformation occurs first. The pressure distribution is dependent on the shape and size of the indenter tip. In this work, a $\sim$22 μm diameter spherical tip was used. However, it was also determined that the separation between the points of maximum shear stress and hydrostatic stress is dependent on the size of the indenter tip. The more commonly used pointed indenter (Berkovich) tip may result in minimal separation between the two maxima, suggesting that the maximum load regime within which buried layers and single mode deformation indents can be observed would be minimal. Conversely, increasing the tip diameter should result in an increased maximum load regime within which these interesting phenomena can be more easily observed.

Pressure Unloading

Slow unloading of indentation-induced pressure from (β-Sn)-Si results in a transformation to a bc8/r8 mixed structure, while fast unloading results in a transformation to a-Si [75]. It is believed that the dense (β-Sn)-Si does not have the time to nucleate a less dense crystalline structure during fast unloading, thus an amorphous structure is formed instead. It was observed in this work that this transformation was dependent on the size of the transformed region, with a-Si observed more often in smaller regions. This may be due to the surface area to volume ratio of the transformed region. In general, smaller transformed regions have a larger surface area which results in greater residual stress from the interface between the transformed region and the underlying dc-Si. One possible explanation is that the residual stress from the transformed material/underlying dc-Si interface (most likely an in-plane strain similar to that caused by lattice mismatch) may combine with the residual stress orientated along the indentation axis that keeps the bc8/r8 structure stable. This may explain why, in transformed regions where both a-Si and the bc8/r8 structure were observed, the a-Si is commonly found along the edges of the region. This is in agreement with studies reporting that the transformation to a crystalline end phase after unloading is preferred in larger indents [41] (lower surface area to volume ratio) and indents made into a-Si [107] (no crystal/crystal interface).

It was further shown that, during uniaxial pressure unloading, a significant amount of residual stress remains within the sample which is characterised by elongation of the unit cell along the axis of unloading. It can further be proposed that such unloading also causes a significant amount of crystallite orientation along the same axis. That is, each individual crystallite may be preferentially aligned along the axis of indentation. The observation of individual reflections for bc8-Si, r8-Si, Si-XIII, and hd-Si in SADPs but the observation of more ring-like reflections for nc dc-Si may be indicative of the crystallites returning to a more random orientation during annealing. Interestingly, directional preference has previously been reported [45] for Si-XIII, the novel phase that was suggested to only be present due to residual stress.

After complete pressure removal, a residual impression remains in the sample. Figure 7.1 shows the plastically deformed region before and after indentation. The volume of dc-Si before indentation is larger than the volume of the denser bc8/r8 mixed structure after indentation. This density difference suggest that there will be significant compressive stress within the transformed volume and the underlying dc-Si after complete indentation unloading. As the region is compressed from both directions in the sample surface plane but only from below along the axis of indentation, a residual stress that is orientated along this axis is expected.

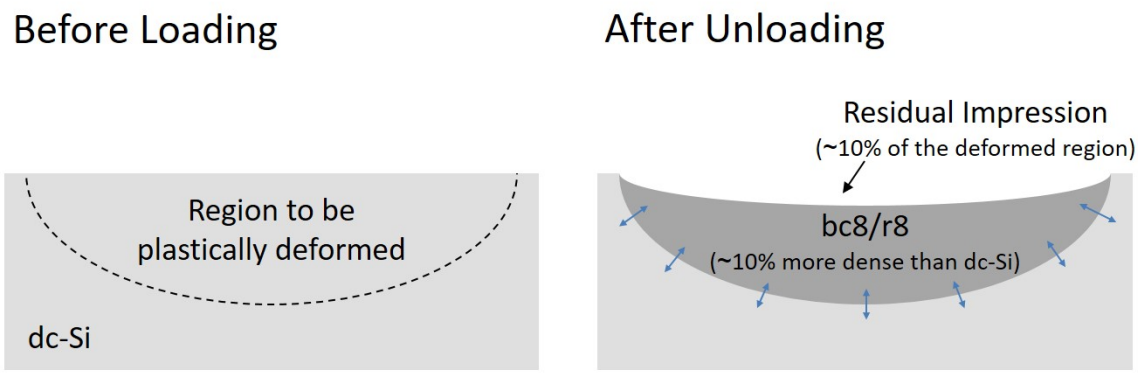

Fig. 7.1: A schematic of a dc-Si sample before and after indentation. The decrease in volume due to indentation suggests that, after unloading, the underlying dc-Si applies a residual compression (indicated by the blue arrows).

Thermal Annealing

Annealing of the bc8/r8 mixed structure formed via indentation results in the metastable phases of Si-XIII and hd-Si. In the absence of uniaxial residual stress, r8-Si is believed to transform to bc8-Si which further transforms to hd-Si. Under this residual stress, r8-Si is believed to transform to Si-XIII, which also further transforms to hd-Si. It is possible that Si-XIII is a more energetically favourable variant of bc8-Si in situations where uniaxial residual stress is present. Thus, it is possible that this residual stress may act as a catalyst to produce novel phases along well reported transformation pathways (such as in DAC experiments).

Broader Framework: Considering Ge and C

The framework for these transformations in Si may also be relevant to other covalently bonded group IV materials (i.e. Ge and C). Ge, like Si, has been reported to phase transform under compression. Similar to Si, Ge transforms to a metallic β-Sn phase under compression in a DAC [24]. Unlike Si, slow decompression results in a simple tetragonal structure (st12-Ge) [138] while rapid decompression results in a body centred cubic structure (bc8-Ge) similar to that observed in Si after decompression [27]. Under indentation-induced pressure, a rhomobohedral structure (r8-Ge) is observed on unloading which is unstable and rapidly transforms to a hexagonal diamond structure (hd-Ge) at ambient conditions [210]. While there are clear similarities in the phase transformations observed in Si and Ge, there are phases that are reported for one element but have not been reported for the other. For example, there is no phase in Ge that is analogous to Si-XIII (i.e. "Ge-XIII"). Interestingly, Ge has been shown to transform along similar pathways under indentation-induced pressure at lowered temperatures [211]. Thus, annealing of exotic phases of Ge formed in such a manner, if they experience

significant orientation-dependent residual stress, may result in a new "Ge-XIII" phase.

C has also been reported to exist in many stable crystal structures. However, while the atoms are tetrahedrally (sp^3) bonded in the phases of Si and Ge, many of the reported structures of C are dominated by trigonally (sp^2) bonded atoms. Thus, many of the crystal structures observed in Si do not have an analogous structure in C. One possible reason for the paucity of analogous C structures is that the pressures required for formation is too high (500 GPa for r8-C [212], 1075 GPa for bc8-C [213]). In this work, the presence of shear stress and the application of a hold duration at maximum load were found to promote phase transformation in Si. Thus, holding a C precursor under indentation-induced pressure at a (relatively) low maximum load for extended periods of time may promote a similar transformation to a novel phase in C.

Conversely, studies in the other group IV materials may also present directions for which the current framework for Si may be improved. For example, studies in Ge show that phase transformation during indentation-induced pressure loading is affected by shear [210] and temperature [211]. Further, hd-C has been formed from an a-C precursor (i.e. glassy carbon) when thermally annealed under pressure [214]. Similar experiments can be performed on Si to promote existing transformation pathways or discover new pathways.

7.2.2 Properties of the Exotic Phases formed via Indentation

This work was originally motivated by the observation of potentially significant volumes of the technologically interesting r8-Si phase within a bc8/r8 mixed structure formed using indentation. Unlike traditional high-pressure experiments using a DAC, significant volumes of r8-Si are observed after indentation due to residual stress in the indented region. Annealing of this stressed region results in Si-XIII. These two major differences observed between indentation-induced phase transformation and DAC experimentation suggest that, if this uniaxial residual stress could be induced via another pressure-application technique, significant volumes of r8-Si and Si-XIII may also be formed.

Under such residual stress, the bc8/r8 mixed structure was found to be comprised of predominantly r8-Si (up to 80%). It is interesting to note that this is close to the phase fraction reported using Raman microspectroscopy, despite the Raman cross-section of the respective phases being unknown. Indeed, in light of this new XRD analysis, r8-Si and bc8-Si may have very similar Raman cross-sections. Thus, calculations of the phase ratios using Raman may be a fast and accurate method for measuring such a ratio. Therefore, it is interesting to look back at the ratios reported in Raman measurements from previously published data [93], which consistently report a ratio of ∼80% r8-Si to ∼20% bc8-Si, including for both large and small maximum loads and for indents made into a-Si as well as dc-Si [41]. Thus, it seems ∼80%

might be a 'golden' ratio for the indentation-induced bc8/r8 mixed structure. In trying to understand why this may be the case, the respective free energies and densities of the r8-Si and bc8-Si were examined. However, modelling work shown in Fig. 7.2 (from Ref. [215]) shows that both bc8-Si and r8-Si have very similar free energies and densities relative to dc-Si. Therefore, this golden ratio may be driven by other external factors. It can be proposed that this phase fraction is instead related to the geometry of the final indented region, which is surrounded by undeformed dc-Si. To understand this further, it is important to recall the details of the entire phase transformation process. The first transformation from dc-Si to (β-Sn)-Si during loading results in a large 22% increase in density. On unloading, the transformed region undergoes a further transformation to a mixture of bc8-Si and r8-Si which are both only $\sim$10% more dense than dc-Si (i.e. an $\sim$10% decrease in density from the β-Sn phase it transformed from). A significant volume of material undergoing this transformation results in a pop-out event being observed during unloading. That is, a pop-out indicates a sudden decrease in tip penetration depth that can be attributed to substantial volume of (β-Sn)-Si transforming to the less dense bc8/r8 structure. As the sample transformed region is surrounded by rigid dc-Si in all other directions, a greater expansion along the unloading axis is expected. In this manner, the size and position of the pop-out may be related to the residual stress that allows r8-Si to remain stable within the bc8/r8 mixed structure. The r8-Si phase fraction may vary between indents relative to the size of the pop-out observed in the load/unload curve.

Knowing the phase fraction of r8-Si in the mixed phase, the absorption due to the r8-Si portion of the mixed structure can be calculated. The absorption coefficient for r8-Si determined in this work was compared to the value predicted via DFT [143]. The absorption was shown to be greater than predicted. As the predicted values were calculated for single crystal r8-Si, the difference is most likely due to the polycrystalline nature of the r8-Si in this work. More importantly for practical application, the absorption coefficient for the bc8/r8 structure was found to be very similar to the absorption of pure r8-Si. This is unsurprising due to the observation that r8-Si is the predominant phase within the mixed structure. Therefore, this result is good news for those interested in integrating r8-Si (in the form of a bc8/r8 mixed structure) into existing Si devices for PV applications. However, the presented value was determined only across the 0.8 eV - 1.12 eV photon energy range from a polycrystalline structure embedded in a dc-Si substrate. A more rigorous confirmation of r8-Si's potential as a PV material requires determination of the absorption from a large, phase pure, single crystal or large grain polycrystalline film of r8-Si. The formation of such a film, if possible, is a promising direction for further study.

Another phase that has promising optical properties is hd-Si. A large window in which hd-Si is the sole crystalline phase present has been reported and a high activation energy has been calculated for the thermal transition to nc dc-Si. Applying strain to hd-Si to experimentally verify the ability to tailor its band-gap [141], particularly from an indirect band-gap to a direct

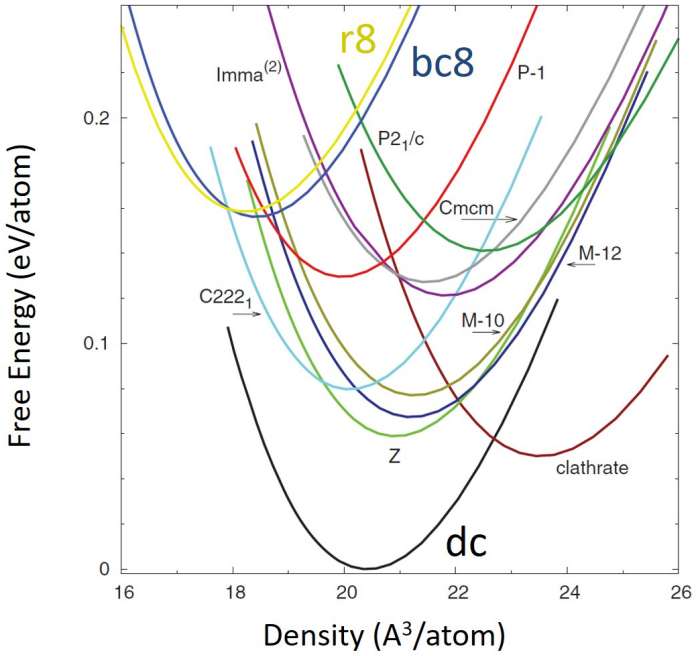

Fig. 7.2: Free energy per atom as a function of density for several exotic Si phases (adapted from Ref. [215]). The free energy per atom at all densities is similar for bc8-Si (blue) and r8-Si (yellow) relative to the free energy per atom for many other phases, such as dc-Si (black).

band-gap, may lead to future device applications.

7.2.3 Scaling and Technological Viability

This work has shown that the properties of the bc8/r8 mixed structure and the stability of hd-Si have technological potential. Thus, the viability of scaling the production of these exotic phases to a technologically feasible level is important and interesting to consider.

During indentation loading, phase transformation was promoted by holding the tip for long periods of time at maximum load. In this work, indentation conditions were presented for which all indents that deformed plastically did so via phase transformation. However, it should be noted that under these conditions, the majority of the indents responded elastically. It is possible for the hold time to be extended to promote a greater number of indents to phase transform. If the hold time becomes prohibitively long, the samples that respond purely elastically may be re-indented with (presumably) no negative impact to the transformation process.

Another method for promoting transformation worth exploring is "seeding" phase transformation in a two-step method. In the first step, smaller phase transformed regions could be

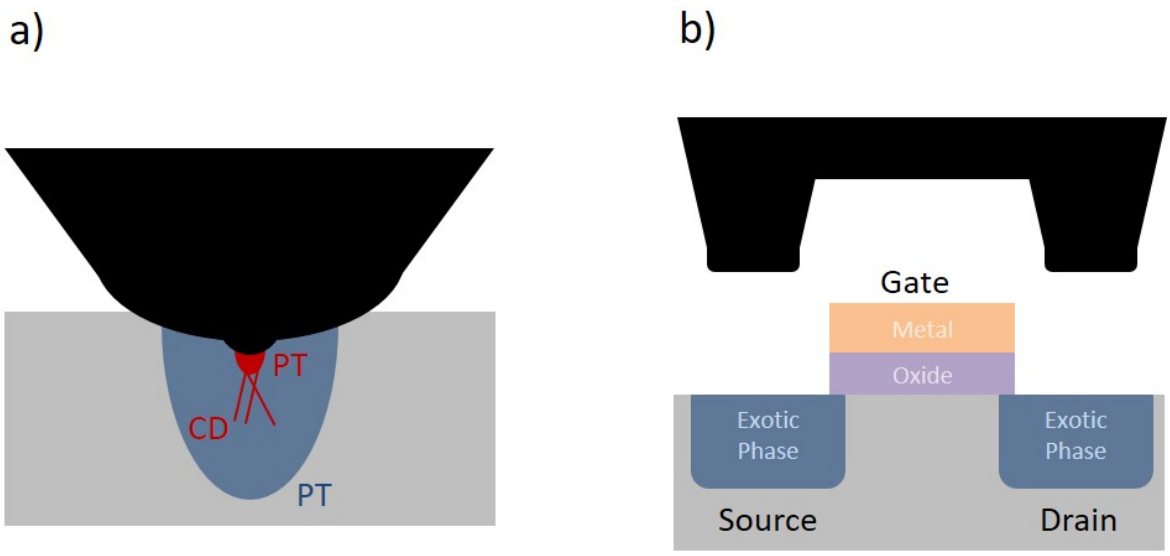

Fig. 7.3: (a) Schematic of the proposed "double tipped" indenter. The phase transformed region (PT) and crystalline defects (CD) induced by the smaller tip is indicated in red. The PT region induced by the larger tip is indicated in blue and is sufficient to remove the CD induced by the smaller tip. (b) Proposed schematic of a "stamp" indenter that could be developed to produce exotic Si phases in a conventional MOSFET as a substitution for n-doped contact pads.

seeded into the sample. This is followed by a second step where a larger pressure is applied to cause the seeded phase transformed region to grow. For example, the two pathways of plastic deformation presented here show that a hold duration (to nucleate phase transformation) followed by further loading (to grow the phase transformed region) would be beneficial for producing greater amounts of the bc8/r8 mixed structure. Alternatively, a similar effect may be produced using a small spherical tip attached to a large spherical tip [such as the one shown in Fig. 7.3(a)]. This "double-tipped" indenter potentially would first nucleate both phase transformation and crystalline defects under the smaller tip. As the point of maximum shear stress is related to tip size, the crystalline defects are not expected to extend far below the surface. Thus, the phase transformed region induced by the larger spherical tip (seeded by the initial transformation) can grow to cover the defective crystalline regions. In fact, phase transformation has been reported to be promoted in regions where slip has occurred [104].

It may even be possible to use indentation pressure to grow transformed regions initially formed via different methods. For example, st12-Si is an exotic phase that has not been reported from indentation-induced phase transformation but has been reported from laser-induced phase transformation. It may be possible to apply indentation-induced pressure to a region of st12-Si formed via laser-induced pressure to promote further expansion of this transformed region. In this scenario, further pressure application may result in expansion of the st12-Si volume rather than transforming st12-Si to the β-Sn phase. Indeed, a transformation to a metastable

exotic phase (r8-Si) without first transforming to (β-Sn)-Si has been reported previously [45]

Further, only conventional indenter tips have been used in this work. If a "stamp" style indenter of a desired shape were manufactured, a single indentation process that successfully nucleates phase transformation may produce large regions of these exotic phases to any desired shape. An example of such a stamp is shown in Fig. 7.3(b). In this example, the contact pads (conventionally n-doped dc-Si) for the source and drain of a MOSFET is replaced by an exotic phase of Si that was produced using an indenter stamp [1]. The shape and size of this stamp may be varied in accordance with the task required. At the present time, it appears that such an approach is limited only in the maximum loads that can be produced and the durability of the indenter tip material. Thus, the formation of these exotic phases could feasibly be scaled up to technologically relevant sizes.

7.3 Closing Remark

In this thesis the formation, stability, and properties of several exotic phases of Si that can be formed via indentation-induced pressure have been presented. The inclusion of a hold duration was shown to promote phase transformation. Upon slow pressure removal the transformed region was found to be predominantly r8-Si. Annealing of this transformed region resulted in the metastable phases Si-XIII and hd-Si. From these results, an expanded framework for the formation of these Si phases via pressure and temperature has been presented and discussed.

Further, it has been shown that the bc8/r8 mixed structure formed via indentation exhibit technologically interesting properties. Thus, it is clear that scaling the formation of these phases to industrially viable levels is an important direction for future study.

[1] the exotic phases are formed before oxide and metal deposition in this particular case

Bibliography

[1] Linda Wilson. International technology roadmap for semiconductors (ITRS). *Semiconductor Industry Association*, 2013. 1

[2] Robert N Noyce. Semiconductor device-and-lead structure, April 25 1961. US Patent 2,981,877. 1

[3] Jack S Kilby. Miniaturized electronic circuits, June 23 1964. US Patent 3,138,743. 1

[4] Sheldon L Matlow and Eugene L Ralph. Ruggedized solar cell and process for making the same or the like, May 16 1961. US Patent 2,984,775. 1

[5] Eugene L Ralph. Flexible solar energy converter panel, March 13 1962. US Patent 3,025,335. 1

[6] Lloyd E Jones. Solar cell, February 19 1963. US Patent 3,078,328. 1

[7] Haisheng Rong, Richard Jones, Ansheng Liu, Oded Cohen, Dani Hak, Alexander Fang, and Mario Paniccia. A continuous-wave raman silicon laser. *Nature*, 433(7027):725–728, 2005. 1

[8] Bahram Jalali and Sasan Fathpour. Silicon photonics. *Journal of lightwave technology*, 24(12):4600–4615, 2006. 1

[9] Simply silicon. *Nature Photonics*, 4(8):491–491, 2010. 1

[10] Martin A Green, Keith Emery, Yoshihiro Hishikawa, Wilhelm Warta, and Ewan D Dunlop. Solar cell efficiency tables (version 45). *Progress in photovoltaics: research and applications*, 23(1):1–9, 2015. 1

[11] Shalini Menezes, Hans-Joachim Lewerenz, and Klaus J Bachmann. Efficient and stable solar cell by interfacial film formation. *Nature*, 305(5935):615–616, 1983. 1

[12] Brian Oâregan and M Grfitzeli. A low-cost, high-efficiency solar cell based on dye-sensitized. *nature*, 353(6346):737–740, 1991. 1

[13] Peng Wang, Shaik M Zakeeruddin, Jacques E Moser, Mohammad K Nazeeruddin, Takashi Sekiguchi, and Michael Grätzel. A stable quasi-solid-state dye-sensitized solar cell with an amphiphilic ruthenium sensitizer and polymer gel electrolyte. *Nature materials*, 2(6):402–407, 2003. 1

[14] Jingbi You, Letian Dou, Ken Yoshimura, Takehito Kato, Kenichiro Ohya, Tom Moriarty, Keith Emery, Chun-Chao Chen, Jing Gao, Gang Li, et al. A polymer tandem solar cell with 10.6% power conversion efficiency. *Nature communications*, 4:1446, 2013. 1

[15] Robert R Schaller. *Technological innovation in the semiconductor industry: a case study of the International Technology Roadmap for Semiconductors (ITRS)*. PhD thesis, George Mason University, 2004. 1

[16] Brian M Krzanich. Intel 2016 annual report, 2016. 1

[17] Matt Beekman. New hopes for allotropes. *Materials Today*, 2015. 1

[18] Bianca Haberl, Timothy A Strobel, and Jodie E Bradby. Pathways to exotic metastable silicon allotropes. *Applied Physics Reviews*, 3(4):040808, 2016. 1, 4, 11, 13

[19] Damien Connétable. First-principles calculations of carbon clathrates: Comparison to silicon and germanium clathrates. *Physical Review B*, 82(7):075209, 2010. 1

[20] Chris J Pickard and RJ Needs. Hypothetical low-energy chiral framework structure of group 14 elements. *Physical Review B*, 81(1):014106, 2010. 1

[21] HJ Xiang, Bing Huang, Erjun Kan, Su-Huai Wei, and XG Gong. Towards direct-gap silicon phases by the inverse band structure design approach. *Physical review letters*, 110(11):118702, 2013. 1

[22] In-Ho Lee, Jooyoung Lee, Young Jun Oh, Sunghyun Kim, and KJ Chang. Computational search for direct band gap silicon crystals. *Physical Review B*, 90(11):115209, 2014. 1

[23] Andrés Mujica, Chris J Pickard, and Richard J Needs. Low-energy tetrahedral polymorphs of carbon, silicon, and germanium. *Physical Review B*, 91(21):214104, 2015. 1, 13, 148, 152

[24] S Minomura and HG Drickamer. Pressure induced phase transitions in silicon, germanium and some iii–v compounds. *Journal of Physics and Chemistry of Solids*, 23(5):451–456, 1962. 1, 6, 10, 61, 63, 124

[25] JZ Hu, LD Merkle, CS Menoni, and IL Spain. Crystal data for high-pressure phases of silicon. *Physical Review B*, 34(7):4679, 1986. 1, 6

[26] MI McMahon and RJ Nelmes. New high-pressure phase of si. *Physical Review B*, 47(13):8337, 1993. 1, 4, 6

[27] RJ Nelmes and MI McMahon. Structural transitions in the group iv, iii-v, and ii-vi semiconductors under pressure. *Semiconductors and semimetals*, 54:145–246, 1998. 1, 4, 124

[28] M Hanfland, U Schwarz, K Syassen, and K Takemura. Crystal structure of the high-pressure phase silicon vi. *Physical review letters*, 82(6):1197, 1999. 1, 6

[29] Aiyasami Jayaraman. Diamond anvil cell and high-pressure physical investigations. *Reviews of Modern Physics*, 55(1):65, 1983. 1

[30] RO Piltz, JR Maclean, SJ Clark, GJ Ackland, PD Hatton, and J Crain. Structure and properties of silicon XII: A complex tetrahedrally bonded phase. *Physical Review B*, 52(6):4072, 1995. 1, 4, 7, 15, 16, 33, 38, 39, 46, 48, 50, 51, 69, 106, 114

[31] GJ Ackland. Theory of high pressure phases of group-iv and iii–v semiconductors. *physica status solidi (b)*, 223(2):361–368, 2001. 1

[32] RH Wentorf and JS Kasper. Two new forms of silicon. *Science*, 139(3552):338–339, 1963. 1, 6, 10, 12, 14, 16, 33, 61, 86, 96, 117

[33] Duck Young Kim, Stevce Stefanoski, Oleksandr O Kurakevych, and Timothy A Strobel. Synthesis of an open-framework allotrope of silicon. *Nature materials*, 14(2):169–173, 2015. 2, 14

[34] Ludovic Rapp, Bianca Haberl, Chris J Pickard, Jodie E Bradby, Eugene G Gamaly, James S Williams, and Andrei V Rode. Experimental evidence of new tetragonal polymorphs of silicon formed through ultrafast laser-induced confined microexplosion. *Nature communications*, 6, 2015. 2, 14

[35] Alvin P Gerk and David Tabor. Indentation hardness and semiconductor–metal transition of germanium and silicon. *Nature*, 271(5647):732–733, 1978. 2

[36] GM Pharr, WC Oliver, and DS Harding. New evidence for a pressure-induced phase transformation during the indentation of silicon. *Journal of Materials Research*, 6(06):1129–1130, 1991. 2, 7

[37] ER Weppelmann, JS Field, and MV Swain. Observation, analysis, and simulation of the hysteresis of silicon using ultra-micro-indentation with spherical indenters. *Journal of Materials Research*, 8(04):830–840, 1993. 2, 7, 8, 88

[38] A Kailer, YG Gogotsi, and KG Nickel. Phase transformations of silicon caused by contact loading. *Journal of applied physics*, 81(7):3057–3063, 1997. 2, 7, 8, 12, 17, 19, 88, 93, 94, 114, 115

[39] JE Bradby, JS Williams, J Wong-Leung, MV Swain, and P Munroe. Mechanical deformation in silicon by micro-indentation. *Journal of Materials Research*, 16(5):1500–1507, 2001. 2, 7, 8, 9, 21, 61, 62, 63, 97

[40] I Zarudi, J Zou, and LC Zhang. Microstructures of phases in indented silicon: A high resolution characterization. *Applied physics letters*, 82(6):874–876, 2003. 2, 9, 21, 61

[41] S Ruffell, B Haberl, S Koenig, JE Bradby, and JS Williams. Annealing of nanoindentation-induced high pressure crystalline phases created in crystalline and amorphous silicon. *Journal of Applied Physics*, 105(9):093513–093513, 2009. 2, 9, 12, 37, 61, 93, 94, 95, 97, 102, 113, 115, 116, 123, 125, 148

[42] BC Johnson, Bianca Haberl, JE Bradby, Jeffrey C McCallum, and JS Williams. Temperature dependence of raman scattering from the high-pressure phases of si induced by indentation. *Physical Review B*, 83(23):235205, 2011. 2, 27, 67, 108, 112

[43] YB Gerbig, CA Michaels, and RF Cook. In situ observation of the spatial distribution of crystalline phases during pressure-induced transformations of indented silicon thin films. *Journal of Materials Research*, 30(03):390–406, 2015. 2, 8, 10, 11, 115

[44] Daibin Ge, Vladislav Domnich, and Yury Gogotsi. Thermal stability of metastable silicon phases produced by nanoindentation. *Journal of Applied Physics*, 95(5):2725–2731, 2004. 2, 9, 12, 17, 27, 69, 93, 94, 96, 97, 106, 107, 114, 115, 148

[45] Bianca Haberl, Malcolm Guthrie, Stanislav V Sinogeikin, Guoyin Shen, James S Williams, and Jodie E Bradby. Thermal evolution of the metastable r8 and bc8 polymorphs of silicon. *High Pressure Research*, 35(2):99–116, 2015. 2, 7, 9, 12, 96, 106, 107, 113, 118, 123, 129, 148, 151, 152

[46] V Domnich, Y Gogotsi, and S Dub. Effect of phase transformations on the shape of the unloading curve in the nanoindentation of silicon. *Applied Physics Letters*, 76(16):2214–2216, 2000. 2, 8, 21

[47] Bianca Haberl, ACY Liu, JE Bradby, Simon Ruffell, JS Williams, and Paul Munroe. Structural characterization of pressure-induced amorphous silicon. *Physical Review B*, 79(15):155209, 2009. 2, 8, 11

[48] E Holmström, Bianca Haberl, Olli H Pakarinen, Kai Nordlund, Flyura Djurabekova, Raul Arenal, James S Williams, Jodie E Bradby, Timothy C Petersen, and ACY Liu. Dependence of short and intermediate-range order on preparation in experimental and modeled pure a-si. *Journal of Non-Crystalline Solids*, 438:26–36, 2016. 2

[49] JS Field and MV Swain. Determining the mechanical properties of small volumes of material from submicrometer spherical indentations. *Journal of Materials Research*, 10(1):101–112, 1995. 2, 10

[50] I Zarudi, LC Zhang, WCD Cheong, and TX Yu. The difference of phase distributions in silicon after indentation with Berkovich and spherical indenters. *Acta Materialia*, 53(18):4795–4800, 2005. 2, 8, 9, 10, 17, 62, 88

[51] Jae-il Jang, MJ Lance, Songqing Wen, Ting Y Tsui, and GM Pharr. Indentation-induced phase transformations in silicon: influences of load, rate and indenter angle on the transformation behavior. *Acta Materialia*, 53(6):1759–1770, 2005. 2, 10, 19, 21

[52] GE Duvall and RA Graham. Phase transitions under shock-wave loading. *Reviews of Modern Physics*, 49(3):523, 1977. 2, 10

[53] Dariusz Chrobak, Natalia Tymiak, Aaron Beaber, Ozan Ugurlu, William W Gerberich, and Roman Nowak. Deconfinement leads to changes in the nanoscale plasticity of silicon. *Nature nanotechnology*, 6(8):480–484, 2011. 2, 10

[54] J Sun, L Fang, J Han, Y Han, H Chen, and K Sun. Phase transformations of mono-crystal silicon induced by two-body and three-body abrasion in nanoscale. *Computational Materials Science*, 82:140–150, 2014. 2, 9, 10, 62, 86

[55] Sherman Wong, Bianca Haberl, James S Williams, and Jodie E Bradby. Phase transformation as the single-mode mechanical deformation of silicon. *Applied Physics Letters*, 106(25):252103, 2015. 2, 9, 10, 11, 24, 41, 52, 61, 62, 63, 72, 77

[56] S Ruffell, K Sears, JE Bradby, and JS Williams. Room temperature writing of electrically conductive and insulating zones in silicon by nanoindentation. *Applied Physics Letters*, 98(5):052105–052105, 2011. 2, 11

[57] Michael OâKeeffe, Maxim A Peskov, Stuart J Ramsden, and Omar M Yaghi. The reticular chemistry structure resource (rcsr) database of, and symbols for, crystal nets. *Accounts of Chemical Research*, 41(12):1782–1789, 2008. 4

[58] JC Jamieson. Phase transitions under pressure of the semiconductor metal types and the earth's interior. *178in Abstracts for*, page 1963b, 1962. 6

[59] MC Gupta and AL Ruoff. Static compression of silicon in the [100] and in the [111] directions. *Journal of Applied Physics*, 51(2):1072–1075, 1980. 6, 10, 61, 86

[60] BA Weinstein and GJ Piermarini. Raman scattering and phonon dispersion in si and gap at very high pressure. *Physical Review B*, 12(4):1172, 1975. 6, 11, 61, 86

[61] GM Pharr and WC Oliver. Nanoindentation of silver-relations between hardness and dislocation structure. *Journal of Materials Research*, 4(01):94–101, 1989. 6, 7, 11, 61, 86

[62] Steven J Duclos, Yogesh K Vohra, and Arthur L Ruoff. Experimental study of the crystal stability and equation of state of si to 248 gpa. *Physical Review B*, 41(17):12021, 1990. 6

[63] J Crain, GJ Ackland, JR Maclean, RO Piltz, PD Hatton, and GS Pawley. Reversible pressure-induced structural transitions between metastable phases of silicon. *Physical Review B*, 50(17):13043, 1994. 6, 7, 16, 38, 39, 45, 51

[64] You-Xiang Zhao, Fred Buehler, James R Sites, and Ian L Spain. New metastable phases of silicon. *Solid state communications*, 59(10):679–682, 1986. 6, 14

[65] Stefan Klotz. *Techniques in high pressure neutron scattering*. CRC press, 2012. 6, 11

[66] Naoto Kawai and Shoichi Endo. The generation of ultrahigh hydrostatic pressures by a split sphere apparatus. *Review of Scientific Instruments*, 41(8):1178–1181, 1970. 6, 11, 57

[67] VV Brazhkin, AG Lyapin, SV Popova, and RN Voloshin. Solid-phase disordering of bulk ge and si samples under pressure. *JETP LETTERS C/C OF PIS'MA V ZHURNAL EKSPERIMENTAL'NOI TEORETICHESKOI FIZIKI*, 56:152–152, 1992. 6, 7, 12, 117, 118

[68] Paul F McMillan, Mark Wilson, Dominik Daisenberger, and Denis Machon. A density-driven phase transition between semiconducting and metallic polyamorphs of silicon. *Nature materials*, 4(9):680–684, 2005. 7

[69] KK Pandey, Nandini Garg, KV Shanavas, Surinder M Sharma, and SK Sikka. Pressure induced crystallization in amorphous silicon. *Journal of Applied Physics*, 109(11):113511, 2011. 7

[70] Bianca Haberl, Malcolm Guthrie, David Sprouster, James Williams, and Jodie Bradby. New insight into pressure-induced phase transitions of amorphous silicon: the role of impurities. *Journal of Applied Crystallography*, 46(3):758–768, 2013. 7

[71] Motoharu Imai, Takeshi Mitamura, Kenichi Yaoita, and Kazuhiko Tsuji. Pressure-induced phase transition of crystalline and amorphous silicon and germanium at low temperatures. *High Pressure Research*, 15(3):167–189, 1996. 7

[72] Warren Carl Oliver and George Mathews Pharr. An improved technique for determining hardness and elastic modulus using load and displacement sensing indentation experiments. *Journal of materials research*, 7(06):1564–1583, 1992. 7, 10, 19, 20, 22

[73] JS Field and MV Swain. A simple predictive model for spherical indentation. *Journal of Materials Research*, 8(02):297–306, 1993. 7, 10, 19

[74] GM Pharr, WC Oliver, and DR Clarke. The mechanical behavior of silicon during small-scale indentation. *Journal of Electronic Materials*, 19(9):881–887, 1990. 7

[75] Andreas Kailer, Klaus G Nickel, and Yury G Gogotsi. Raman microspectroscopy of nanocrystalline and amorphous phases in hardness indentations. *Journal of Raman Spectroscopy*, 30(10):939–946, 1999. 7, 8, 88, 123

[76] JE Bradby, JS Williams, and Michael Vincent Swain. In situ electrical characterization of phase transformations in si during indentation. *Physical Review B*, 67(8):085205, 2003. 7, 8, 88

[77] Simon Ruffell, K Sears, Andrew P Knights, JE Bradby, and JS Williams. Experimental evidence for semiconducting behavior of si-xii. *Physical Review B*, 83(7):075316, 2011. 7, 17, 39

[78] IV Gridneva, Yu V Milman, and VI Trefilov. Phase transition in diamond-structure crystals during hardness measurements. *Physica status solidi (a)*, 14(1):177–182, 1972. 7

[79] Alvin P Gerk and David Tabor. Indentation hardness and semiconductor–metal transition of germanium and silicon. *Nature*, 271(5647):732–733, 1978. 7

[80] Steven Danyluk, Dae Soon Lim, and Juris Kalejs. Microhardness of carbon-doped (111) p-type czochralski silicon. *Journal of materials science letters*, 4(9):1135–1137, 1985. 7

[81] DR Clarke, MC Kroll, PD Kirchner, RF Cook, and BJ Hockey. Amorphization and conductivity of silicon and germanium induced by indentation. *Physical review letters*, 60(21):2156, 1988. 7

[82] John J Gilman. Insulator-metal transitions at microindentations. *Journal of materials research*, 7(03):535–538, 1992. 8

[83] V Domnich and Y Gogotsi. Pressure-induced phase transformations in semiconductors under contact loading. *Frontiers of High Pressure Research II: Application of High Pressure to Low-Dimensional Novel Electronic Materials*, pages 291–302, 2002. 8, 12, 93, 94

[84] Tom Juliano, Vladislav Domnich, and Yury Gogotsi. Examining pressure-induced phase transformations in silicon by spherical indentation and raman spectroscopy: a statistical study. *Journal of Materials research*, 19(10):3099–3108, 2004. 8

[85] D Ge, AM Minor, EA Stach, and JW Morris Jr. Size effects in the nanoindentation of silicon at ambient temperature. *Philosophical Magazine*, 86(25-26):4069–4080, 2006. 8, 11

[86] GS Smith, EB Tadmor, N Bernstein, and E Kaxiras. Multiscale simulations of silicon nanoindentation. *Acta Materialia*, 49(19):4089–4101, 2001. 8

[87] CF Sanz-Navarro, SD Kenny, and R Smith. Atomistic simulations of structural transformations of silicon surfaces under nanoindentation. *Nanotechnology*, 15(5):692, 2004. 8

[88] Yen-Hung Lin, Sheng-Rui Jian, Yi-Shao Lai, and Ping-Feng Yang. Molecular dynamics simulation of nanoindentation-induced mechanical deformation and phase transformation in monocrystalline silicon. *Nanoscale Research Letters*, 3(2):71, 2008. 8

[89] Dong Earn Kim and Soo Ik Oh. Deformation pathway to high-pressure phases of silicon during nanoindentation. *Journal of Applied Physics*, 104(1):013502, 2008. 8

[90] Pierre Eyben, Francesca Clemente, Kris Vanstreels, Geoffrey Pourtois, Trudo Clarysse, Edouard Duriau, Thomas Hantschel, Kiroubanand Sankaran, Jay Mody, Wilfried Vandervorst, et al. Analysis and modeling of the high vacuum scanning spreading resistance microscopy nanocontact on silicon a. *Journal of Vacuum Science & Technology B, Nanotechnology and Microelectronics: Materials, Processing, Measurement, and Phenomena*, 28(2):401–406, 2010. 8

[91] Yvonne B Gerbig, Chris A Michaels, Aaron M Forster, and Robert F Cook. In situ observation of the indentation-induced phase transformation of silicon thin films. *Physical Review B*, 85(10):104102, 2012. 8, 90, 115

[92] JE Bradby, JS Williams, J Wong-Leung, Michael Vincent Swain, and Paul Munroe. Transmission electron microscopy observation of deformation microstructure under spherical indentation in silicon. *Applied Physics Letters*, 77(23):3749–3751, 2000. 8, 9, 21, 61, 82, 88

[93] S Ruffell, JE Bradby, JS Williams, and P Munroe. Formation and growth of nanoindentation-induced high pressure phases in crystalline and amorphous silicon. *Journal of Applied Physics*, 102(6):063521, 2007. 8, 9, 11, 12, 17, 21, 61, 93, 94, 95, 97, 116, 125

[94] Zhidan Zeng, Qiaoshi Zeng, Wendy L Mao, and Shaoxing Qu. Phase transitions in metastable phases of silicon. *Journal of Applied Physics*, 115(10):103514, 2014. 9, 12, 93, 94, 95, 102, 103, 111, 116, 117

[95] Vladislav Domnich, Daibin Ge, and Yury Gogotsi. Indentation-induced phase transformations in semiconductors. *High Pressure Surface Science and Engineering*, pages 381–442, 2004. 9

[96] I Zarudi, LC Zhang, and MV Swain. Behavior of monocrystalline silicon under cyclic microindentations with a spherical indenter. *Applied Physics Letters*, 82(7):1027–1029, 2003. 9, 21, 61

[97] Trevor F Page, Warren C Oliver, and Carl J McHargue. The deformation behavior of ceramic crystals subjected to very low load (nano) indentations. *Journal of Materials Research*, 7(02):450–473, 1992. 9

[98] K Higashida, N Narita, M Tanaka, T Morikawa, Y Miura, and R Onodera. Crack tip dislocations in silicon characterized by high-voltage electron microscopy. *Philosophical Magazine A*, 82(17-18):3263–3273, 2002. 9

[99] T Vodenitcharova and LC Zhang. A mechanics prediction of the behaviour of monocrystalline silicon under nano-indentation. *International journal of solids and structures*, 40(12):2989–2998, 2003. 9, 10, 122

[100] Ju-Young Kim, Kyung-Woo Lee, Jung-Suk Lee, and Dongil Kwon. Determination of tensile properties by instrumented indentation technique: Representative stress and strain approach. *Surface and Coatings Technology*, 201(7):4278–4283, 2006. 9, 10, 122

[101] D Chrobak, Kwang-Ho Kim, KJ Kurzydłowski, and R Nowak. Nanoindentation experiments with different loading rate distinguish the mechanism of incipient plasticity. *Applied Physics Letters*, 103(7):072101, 2013. 9, 62, 80, 82

[102] Yang-Tse Cheng and Che-Min Cheng. What is indentation hardness? *Surface and Coatings Technology*, 133:417–424, 2000. 10

[103] Chang-Fu Han and Jen-Fin Lin. The model developed for stress-induced structural phase transformations of micro-crystalline silicon films. *Nano-Micro Letters*, 2(2):68–73, 2010. 10

[104] Yvonne B Gerbig, Stephan J Stranick, and Robert F Cook. Direct observation of phase transformation anisotropy in indented silicon studied by confocal raman spectroscopy. *Physical Review B*, 83(20):205209, 2011. 10, 70, 80, 86, 128

[105] I Zarudi and LC Zhang. Structure changes in mono-crystalline silicon subjected to indentationâyexperimental findings. *Tribology International*, 32(12):701–712, 1999. 11, 69

[106] R Rao, JE Bradby, and JS Williams. Patterning of silicon by indentation and chemical etching. *Applied Physics Letters*, 91(12):123113, 2007. 11

[107] S Ruffell, JE Bradby, and JS Williams. High pressure crystalline phase formation during nanoindentation: Amorphous versus crystalline silicon. *Applied physics letters*, 89(9):091919, 2006. 11, 12, 123

[108] S Roorda, S Doorn, WC Sinke, PMLO Scholte, and E Van Loenen. Calorimetric evidence for structural relaxation in amorphous silicon. *Physical Review Letters*, 62(16):1880, 1989. 11, 116

[109] S Roorda, WC Sinke, JM Poate, DC Jacobson, S Dierker, BS Dennis, DJ Eaglesham, F Spaepen, and P Fuoss. Structural relaxation and defect annihilation in pure amorphous silicon. *Physical Review B*, 44(8):3702, 1991. 11

[110] JS Williams, HH Tan, RD Goldberg, RA Brown, and C Jagadish. Dynamic annealing and amorphous phase formation in si, gaas and algaas under ion irradiation. In *MRS Proceedings*, volume 316, page 15. Cambridge Univ Press, 1993. 11

[111] Bianca Haberl, JE Bradby, MV Swain, JS Williams, and Paul Munroe. Phase transformations induced in relaxed amorphous silicon by indentation at room temperature. *Applied physics letters*, 85(23):5559–5561, 2004. 11

[112] B Haberl, JE Bradby, S Ruffell, JS Williams, and P Munroe. Phase transformations induced by spherical indentation in ion-implanted amorphous silicon. *Journal of applied physics*, 100(1):013520, 2006. 11, 97

[113] Leonardus B Bayu Aji, S Ruffell, B Haberl, JE Bradby, and JS Williams. Correlation of indentation-induced phase transformations with the degree of relaxation of ion-implanted amorphous silicon. *Journal of Materials Research*, 28(08):1056–1060, 2013. 11, 41

[114] RJ Kobliska and SA Solin. Raman spectrum of wurtzite silicon. *Physical Review B*, 8(8):3799, 1973. 12

[115] JM Besson, EH Mokhtari, J Gonzalez, and G Weill. Electrical properties of semimetallic silicon iii and semiconductive silicon iv at ambient pressure. *Physical Review Letters*, 59(4):473, 1987. 12, 15, 17

[116] Zhisheng Zhao, Fei Tian, Xiao Dong, Quan Li, Qianqian Wang, Hui Wang, Xin Zhong, Bo Xu, Dongli Yu, Julong He, et al. Tetragonal allotrope of group 14 elements. *Journal of the American Chemical Society*, 134(30):12362–12365, 2012. 13

[117] Jimmy Jia, Ming Li, and Carl V Thompson. Amorphization of silicon by femtosecond laser pulses. *Applied physics letters*, 84(16):3205–3207, 2004. 13

[118] THR Crawford, J Yamanaka, GA Botton, and HK Haugen. High-resolution observations of an amorphous layer and subsurface damage formed by femtosecond laser irradiation of silicon. *Journal of Applied Physics*, 103(5):053104, 2008. 13

[119] Martin Schade, Olga Varlamova, Jürgen Reif, H Blumtritt, Wilfried Erfurth, and HS Leipner. High-resolution investigations of ripple structures formed by femtosecond laser irradiation of silicon. *Analytical and bioanalytical chemistry*, 396(5):1905–1911, 2010. 13

[120] Matthew J Smith, Meng-Ju Sher, Benjamin Franta, Yu-Ting Lin, Eric Mazur, and Silvija Gradečak. The origins of pressure-induced phase transformations during the surface texturing of silicon using femtosecond laser irradiation. *Journal of Applied Physics*, 112(8):083518, 2012. 13

[121] Masashi Tsujino, è¾»éëä[1], *TomokazuSano*, ¸, *OsamiSakata*, ´, *NorimasaOzaki*Δ, *ShigeruKimura*Ξ,

[122] Matthew J Smith, Yu-Ting Lin, Meng-Ju Sher, Mark T Winkler, Eric Mazur, and Silvija Gradečak. Pressure-induced phase transformations during femtosecond-laser doping of silicon. *Journal of Applied Physics*, 110(5):053524, 2011. 13

[123] FP Bundy. Melting of graphite at very high pressure. *The Journal of Chemical Physics*, 38(3):618–630, 1963. 14

[124] Hans-Georg Von Schnering, Martin Schwarz, and Reinhard Nesper. The lithium sodium silicide li3nasi6 and the formation of allo-silicon. *Journal of the Less Common Metals*, 137(1-2):297–310, 1988. 14

[125] John S Kasper, Paul Hagenmuller, Michel Pouchard, and Christian Cros. Clathrate structure of silicon na8si46 and naxsi136 (x< 11). *Science*, 150(3704):1713–1714, 1965. 14

[126] Svilen Bobev and Slavi C Sevov. Synthesis and characterization of large single crystals of silicon and germanium clathrate-ii compounds and a new tin compound with clathrate layers. In *MRS Proceedings*, volume 626, pages Z13–5. Cambridge Univ Press, 2000. 14

[127] Alyssa Ker, Evgeny Todorov, Roger Rousseau, Kentaro Uehara, François-Xavier Lannuzel, and John S Tse. Structure and phase stability of binary zintl-phase compounds: Lithium–group 13 intermetallics and metal-doped group 14 clathrate compounds. *Chemistry–A European Journal*, 8(12):2787–2798, 2002. 14

[128] Shoji Yamanaka. Silicon clathrates and carbon analogs: high pressure synthesis, structure, and superconductivity. *Dalton Transactions*, 39(8):1901–1915, 2010. 14

[129] Bodo Böhme, Arnold Guloy, Zhongjia Tang, Walter Schnelle, Ulrich Burkhardt, Michael Baitinger, and Yuri Grin. Oxidation of m4si4 (m= na, k) to clathrates by hcl or h2o. *Journal of the American Chemical Society*, 129(17):5348–5349, 2007. 14

[130] Ganesh K Ramachandran, Paul F McMillan, Sudip K Deb, Maddury Somayazulu, Jan Gryko, Jianjun Dong, and Otto F Sankey. High-pressure phase transformation of the silicon clathrate si136. *Journal of Physics: Condensed Matter*, 12(17):4013, 2000. 14

[131] Stefan Wippermann, Márton Vörös, Dario Rocca, Adam Gali, G Zimanyi, and Giulia Galli. High-pressure core structures of si nanoparticles for solar energy conversion. *Physical review letters*, 110(4):046804, 2013. 14

[132] William Shockley and Hans J Queisser. Detailed balance limit of efficiency of p-n junction solar cells. *Journal of applied physics*, 32(3):510–519, 1961. 14

[133] JD Joannopoulos and Marvin L Cohen. Electronic properties of complex crystalline and amorphous phases of ge and si. i. density of states and band structures. *Physical Review B*, 7(6):2644, 1973. 15

[134] Rana Biswas, Richard M Martin, RJ Needs, and OH Nielsen. Complex tetrahedral structures of silicon and carbon under pressure. *Physical Review B*, 30(6):3210, 1984. 15

[135] R Biswas and DR Hamann. New classical models for silicon structural energies. *Physical Review B*, 36(12):6434, 1987. 15

[136] Oleksandr O Kurakevych, Yann Le Godec, Wilson A Crichton, JeÌreÌmy Guignard, Timothy A Strobel, Haidong Zhang, Hanyu Liu, Cristina Coelho Diogo, Alain Polian, Nicolas Menguy, et al. Synthesis of bulk bc8 silicon allotrope by direct transformation and reduced-pressure chemical pathways. *Inorganic Chemistry*, 55(17):8943–8950, 2016. 15, 57

[137] Haidong Zhang, Hanyu Liu, Kaya Wei, Oleksandr O Kurakevych, Yann Le Godec, Zhenxian Liu, Joshua Martin, Michael Guerrette, George S Nolas, and Timothy A Strobel. Bc8 silicon (si-iii) is a narrow-gap semiconductor. *Physical Review Letters*, 118(14):146601, 2017. 15, 17, 40, 56, 57, 58, 93, 117

[138] JS Kasper and SM Richards. The crystal structures of new forms of silicon and germanium. *Acta Crystallographica*, 17(6):752–755, 1964. 15, 38, 39, 47, 124

[139] M Murayama and T Nakayama. Chemical trend of band offsets at wurtzite/zinc-blende heterocrystalline semiconductor interfaces. *Physical Review B*, 49(7):4710, 1994. 15

[140] C Raffy, J Furthmüller, and F Bechstedt. Properties of hexagonal polytypes of group-iv elements from first-principles calculations. *Physical Review B*, 66(7):075201, 2002. 15

[141] C Rödl, T Sander, F Bechstedt, J Vidal, Pär Olsson, S Laribi, and J-F Guillemoles. Wurtzite silicon as a potential absorber in photovoltaics: Tailoring the optical absorption by applying strain. *Physical Review B*, 92(4):045207, 2015. 15, 93, 115, 126

[142] JS Kasper and RH Wentorf. Hexagonal (wurtzite) silicon. *Science*, 197(4303):599–599, 1977. 15, 33, 96

[143] Brad D Malone, Jay D Sau, and Marvin L Cohen. Ab initio study of the optical properties of si-xii. *Physical Review B*, 78(16):161202, 2008. 16, 37, 39, 51, 57, 59, 93, 120, 126

[144] Brad D Malone, Jay D Sau, and Marvin L Cohen. Ab initio survey of the electronic structure of tetrahedrally bonded phases of silicon. *Physical Review B*, 78(3):035210, 2008. 16, 37, 39, 40, 93

[145] George Turrell and Jacques Corset. *Raman microscopy: developments and applications*. Academic Press, 1996. 17, 26, 37

[146] Radeberg: ASMEC. *Finite Element Software Package Elastica 3.0*, 2006. 18, 24, 63

[147] Clemens Prescher and Vitali B. Prakapenka. Dioptas: a program for reduction of two-dimensional x-ray diffraction data and data exploration. *High Pressure Research*, 35(3):223–230, 2015. 18, 35, 42, 149

[148] *General Structure Analysis System (GSAS*. 18, 35, 43, 149

[149] David Tabor. *The hardness of metals*. Oxford university press, 2000. 18, 19, 82

[150] E Meyer. Investigations of hardness testing and hardness. *Phys. Z*, 9:66, 1908. 18

[151] TY Tsui, Joost Vlassak, and William D Nix. Indentation plastic displacement field: Part i. the case of soft films on hard substrates. *Journal of Materials Research*, 14(06):2196–2203, 1999. 18

[152] JB Pethicai, R Hutchings, and Wi C Oliver. Hardness measurement at penetration depths as small as 20 nm. *Philosophical Magazine A*, 48(4):593–606, 1983. 18

[153] Warren C Oliver and Georges M Pharr. Measurement of hardness and elastic modulus by instrumented indentation: Advances in understanding and refinements to methodology. *Journal of materials research*, 19(01):3–20, 2004. 19, 20

[154] AP Ternovskii, VP Alekhin, M Kh Shorshorov, MM Khrushchev, and VN Skvortsov. The character of the variation of microhardness with indentation size and the deformation behavior of materials under conditions of concentrated surface loading. *Zavodskaya Laboratoriya*, 39:1242, 1973. 20

[155] SI Bulychev, VP Alekhin, MH Shorshorov, AP Ternovskii, and GD Shnyrev. Determining young's modulus from the indentor penetration diagram. *Ind. Lab.*, 41(9):1409–1412, 1975. 20

[156] SI Bulychev, VP Alekhin, M Kh Shorshorov, and AP Ternovskii. Mechanical properties of materials studied from kinetic diagrams of load versus depth of impression during microimpression. *Strength of Materials*, 8(9):1084–1089, 1976. 20

[157] M Kh Shorshorov, LM Ustinov, LA Verkhovskii, and LE Gukasyan. Interrelation between strength and the structural interface of presed boron-aluminum composite. *Fiz.-Khim. Obrab. Mater*, (3):80–84, 1982. 20

[158] SI Bulychev and VP Alekhin. Method of kinetic hardness and microhardness in testing impression by an indentor.(translation). *Ind. Lab.(USSR)*, 53(11):1091–1096, 1987. 20

[159] Ian N Sneddon. The relation between load and penetration in the axisymmetric boussinesq problem for a punch of arbitrary profile. *International journal of engineering science*, 3(1):47–57, 1965. 20

[160] Li Chang and Liangchi Zhang. Mechanical behaviour characterisation of silicon and effect of loading rate on pop-in: a nanoindentation study under ultra-low loads. *Materials Science and Engineering: A*, 506(1):125–129, 2009. 21

[161] ER Weppelmann, JS Field, and MV Swain. Influence of spherical indentor radius on the indentation-induced transformation behaviour of silicon. *Journal of Materials Science*, 30(9):2455–2462, 1995. 21

[162] G Feng and AHW Ngan. Effects of creep and thermal drift on modulus measurement using depth-sensing indentation. *Journal of Materials Research*, 17(03):660–668, 2002. 22

[163] Rodney Hill. Similarity analysis of creep indentation tests. In *Proceedings of the Royal Society of London A: Mathematical, Physical and Engineering Sciences*, volume 436, pages 617–630. The Royal Society, 1992. 22

[164] AF Bower, NA Fleck, A Needleman, and N Ogbonna. Indentation of a power law creeping solid. In *Proceedings of the Royal Society of London A: Mathematical, Physical and Engineering Sciences*, volume 441, pages 97–124. The Royal Society, 1993. 22

[165] Ben D Beake and James F Smith. High-temperature nanoindentation testing of fused silica and other materials. *Philosophical Magazine A*, 82(10):2179–2186, 2002. 22

[166] *3D Omniprobe^{TM}. Indentation and scratch capabilities for nano-to-micro tribomechanical testing.* 23

[167] J Dolbow and M Gosz. Effect of out-of-plane properties of a polyimide film on the stress fields in microelectronic structures. *Mechanics of materials*, 23(4):311–321, 1996. 25

[168] AE Bell. Review and analysis of laser annealing. *RCA Review, vol. 40, Sept. 1979, p. 295-338.*, 40:295–338, 1979. 25

[169] JA Van Vechten, R Tsu, FW Saris, and D Hoonhout. Reasons to believe pulsed laser annealing of si does not involve simple thermal melting. *Physics Letters A*, 74(6):417–421, 1979. 25

[170] G Lucazeau and L Abello. Raman spectroscopy in solid state physics and material science. theory, techniques and applications. *Analusis*, 23(7):301–311, 1995. 26

[171] RJ Kobliska, SA Solin, M Selders, RK Chang, R Alben, MF Thorpe, and D Weaire. Raman scattering from phonons in polymorphs of si and ge. *Physical Review Letters*, 29(11):725, 1972. 26

[172] M Hanfland and K Syassen. Raman modes of metastable phases of si and ge. *High pressure research*, 3(1-6):242–244, 1990. 26

[173] Paul A Temple and CE Hathaway. Multiphonon raman spectrum of silicon. *Physical Review B*, 7(8):3685, 1973. 27, 96, 106, 107

[174] HaÌkon Ikaros T Hauge, Marcel A Verheijen, Sonia Conesa-Boj, Tanja Etzelstorfer, Marc Watzinger, Dominik Kriegner, Ilaria Zardo, Claudia Fasolato, Francesco Capitani, Paolo Postorino, et al. Hexagonal silicon realized. *Nano letters*, 15(9):5855–5860, 2015. 27, 96, 106, 107

[175] DC Joy and GR Booker. Simultaneous display of micrograph and selected-area channelling pattern using the scanning electron microscope. *Journal of Physics E: Scientific Instruments*, 4(11):837, 1971. 26

[176] Joseph Goldstein, Dale E Newbury, Patrick Echlin, David C Joy, Alton D Romig Jr, Charles E Lyman, Charles Fiori, and Eric Lifshin. *Scanning electron microscopy and X-ray microanalysis: a text for biologists, materials scientists, and geologists*. Springer Science & Business Media, 2012. 28

[177] David B Williams and C Barry Carter. The transmission electron microscope. In *Transmission electron microscopy*, pages 3–17. Springer, 1996. 28

[178] MMJ Treacy, JM Gibson, L Fan, DJ Paterson, and I McNulty. Fluctuation microscopy: a probe of medium range order. *Reports on Progress in Physics*, 68(12):2899, 2005. 28

[179] Feng Wang, Ray Egerton, and Marek Malac. Fourier-ratio deconvolution techniques for electron energy-loss spectroscopy (eels). *Ultramicroscopy*, 109(10):1245–1249, 2009. 28

[180] L.A. Giannuzzi and F.A. Stevie. A review of focused ion beam milling techniques for TEM specimen preparation. *Micron*, 30(3):197–204, 1999. 29

[181] Tao Tao, JaeSang Ro, John Melngailis, Ziling Xue, and Herbert D Kaesz. Focused ion beam induced deposition of platinum. *Journal of Vacuum Science & Technology B: Microelectronics Processing and Phenomena*, 8(6):1826–1829, 1990. 29

[182] W Möller, Th Pfeiffer, and M Schluckebier. Carbon buildup by ion-induced polymerization under 100–400 kev h, he and li bombardment. *Nuclear Instruments and Methods*, 182:297–302, 1981. 29

[183] C Barry Carter and David B Williams. *Transmission electron microscopy*. Springer-Verlag US, 2009. 33

[184] Ralph WG Wyckoff. Cubic closest packed, ccp. *Structure, Cryst. Struct*, 1:7–83, 1963. 33, 96

[185] Bertram Eugene Warren. *X-ray Diffraction*. Courier Corporation, 1969. 33

[186] HaM Rietveld. A profile refinement method for nuclear and magnetic structures. *Journal of applied Crystallography*, 2(2):65–71, 1969. 35

[187] David L Bish and Jeffrey Edward Post. *Modern powder diffraction*, volume 20. Mineralogical Society of America Washington, DC, 1989. 37

[188] Francis Birch. Finite elastic strain of cubic crystals. *Physical Review*, 71(11):809, 1947. 39, 51

[189] Bernd G Pfrommer, Michel Côté, Steven G Louie, and Marvin L Cohen. Ab initio study of silicon in the r 8 phase. *Physical Review B*, 56(11):6662, 1997. 39, 40

[190] Jonathan P Mailoa, Austin J Akey, Christie B Simmons, David Hutchinson, Jay Mathews, Joseph T Sullivan, Daniel Recht, Mark T Winkler, James S Williams, Jeffrey M Warrender, et al. Room-temperature sub-band gap optoelectronic response of hyperdoped silicon. *Nature communications*, 5, 2014. 40, 56

[191] Sherman Wong. Optimised indentation conditions for large-area phase transformations in silicon. Master's thesis, 2014. 41

[192] G Caglioti, A t Paoletti, and FP Ricci. Choice of collimators for a crystal spectrometer for neutron diffraction. *Nuclear Instruments*, 3(4):223–228, 1958. 43

[193] AR Phani and James E Krzanowski. Preferential growth of ti and tin films on si (111) deposited by pulsed laser deposition. *Applied surface science*, 174(2):132–137, 2001. 43

[194] MS Bramble, RL Flemming, and PJA McCausland. Grain size,'spotty'xrd rings, and chemin: Two-dimensional x-ray diffraction as a proxy for grain size measurement in planetary materials. In *Lunar and Planetary Science Conference*, volume 45, page 1658, 2014. 43

[195] WA Dollase. Correction of intensities for preferred orientation in powder diffractometry: application of the march model. *Journal of Applied Crystallography*, 19(4):267–272, 1986. 47

[196] K Cho and J Gurland. The law of mixtures applied to the plastic deformation of two-phase alloys of coarse microstructures. *Metallurgical Transactions A*, 19(8):2027–2040, 1988. 56

[197] Jan W Gooch. Law of mixtures. In *Encyclopedic Dictionary of Polymers*, pages 421–421. Springer, 2011. 56

[198] Zhisheng Zhao, Haidong Zhang, Duck Young Kim, Wentao Hu, Emma S Bullock, and Timothy A Strobel. Properties of the exotic metastable st12 germanium allotrope. *Nature Communications*, 8, 2017. 57

[199] Constance M Bertka and Yingwei Fei. Mineralogy of the martian interior up to core-mantle boundary pressures. *Journal of Geophysical Research: Solid Earth*, 102(B3):5251–5264, 1997. 57

[200] Warren B Jackson, NM Johnson, and DK Biegelsen. Density of gap states of silicon grain boundaries determined by optical absorption. *Applied Physics Letters*, 43(2):195–197, 1983. 58

[201] SM-M Dubois, G-M Rignanese, Thomas Pardoen, and J-C Charlier. Ideal strength of silicon: An ab initio study. *Physical Review B*, 74(23):235203, 2006. 62, 80, 86

[202] Yvonne B Gerbig, Stephan J Stranick, and Robert F Cook. Measurement of residual stress field anisotropy at indentations in silicon. *Scripta Materialia*, 63(5):512–515, 2010. 62

[203] Thomas Wermelinger and Ralph Spolenak. Correlating raman peak shifts with phase transformation and defect densities: a comprehensive tem and raman study on silicon. *Journal of Raman Spectroscopy*, 40(6):679–686, 2009. 67

[204] Emiliano Bonera, Marco Fanciulli, and David N Batchelder. Raman spectroscopy for a micrometric and tensorial analysis of stress in silicon. *Applied Physics Letters*, 81(18):3377–3379, 2002. 67

[205] JR Low and AM Turkalo. Slip band structure and dislocation multiplication in silicon-iron crystals. *Acta metallurgica*, 10(3):215–227, 1962. 86

[206] Krystyn J Van Vliet, Ju Li, Ting Zhu, Sidney Yip, and Subra Suresh. Quantifying the early stages of plasticity through nanoscale experiments and simulations. *Physical Review B*, 67(10):104105, 2003. 86

[207] V Paillard, P Puech, MA Laguna, R Carles, B Kohn, and F Huisken. Improved one-phonon confinement model for an accurate size determination of silicon nanocrystals. *Journal of applied physics*, 86(4):1921–1924, 1999. 95, 96

[208] H Richter, ZP Wang, and L Ley. The one phonon raman spectrum in microcrystalline silicon. *Solid State Communications*, 39(5):625–629, 1981. 95

[209] José Menéndez and Manuel Cardona. Temperature dependence of the first-order raman scattering by phonons in si, ge, and α- s n: Anharmonic effects. *Physical Review B*, 29(4):2051, 1984. 112

[210] Brett C Johnson, Bianca Haberl, Sarita Deshmukh, Brad D Malone, Marvin L Cohen, Jeffrey C McCallum, James S Williams, and Jodie E Bradby. Evidence for the r 8 phase of germanium. *Physical review letters*, 110(8):085502, 2013. 124, 125

[211] L Huston, BC Johnson, B Haberl, JS Williams, and JE Bradby. Stability of pressure-induced phases in germanium. 124, 125

[212] SJ Clark, GJ Ackland, and J Crain. Theoretical stability limit of diamond at ultrahigh pressure. *Physical Review B*, 52(21):15035, 1995. 125

[213] Alfredo A Correa, Stanimir A Bonev, and Giulia Galli. Carbon under extreme conditions: Phase boundaries and electronic properties from first-principles theory. *Proceedings of the National Academy of Sciences*, 103(5):1204–1208, 2006. 125

[214] Thomas B Shiell, Dougal G McCulloch, Jodie E Bradby, Bianca Haberl, Reinhard Boehler, and David R McKenzie. Nanocrystalline hexagonal diamond formed from glassy carbon. *Scientific reports*, 6:37232, 2016. 125

[215] Silvana Botti, José A Flores-Livas, Maximilian Amsler, Stefan Goedecker, and Miguel AL Marques. Low-energy silicon allotropes with strong absorption in the visible for photovoltaic applications. *Physical Review B*, 86(12):121204, 2012. 126, 127

Appendix A

XRD Analysis of Si-XIII

In this thesis, a new sample preparation method for measuring indented regions using x-ray diffraction was presented. This method resulted in a significant amount of XRD data being collected from the indented regions, such that structural analysis could be performed. In this appendix, the same method is applied to indented regions containing Si-XIII to investigate the crystal structure of this exotic phase.

A.1 Introduction

Despite being first discovered over a decade ago [44], the crystal structure of Si-XIII is still unknown. However, several *d*-spacing values [45] and Raman shifts [41, 44] have been experimentally confirmed for this phase. These are presented in Table A.1. The energetically plausible tetragonal structure with a $P4_12_12$ space group discovered via a *ab initio* structure searching approach has been suggested as a potential candidate for Si-XIII [23]. The simulated Raman spectrum for this phase contains all the characteristic peaks associated with Si-XIII. However, the simulated XRD profile does not contain any of the *d*-spacing values associated with Si-XIII. The d-spacing associated with the most prominent peaks in the simulated XRD profile are also presented in Table A.1.

d-spacing	Ref	Raman shift	Ref	$P4_12_12$ *d*-spacing	Ref
5.6 Å	[45]	200 cm^{-1}	[44]	3.96 Å	[23]
4.8 Å	[45]	330 cm^{-1}	[44]	3.57 Å	[23]
4.4 Å	[45]	475 cm^{-1}	[44]	3.10 Å	[23]
		497 cm^{-1}	[41]	2.93 Å	[23]

Table A.1: The experimentally reported *d*-spacing and Raman shift values for Si-XIII. The simulated *d*-spacing values for the potential candidate for Si-XIII ($P4_12_12$) is also presented

A.2 Experimental Method

The samples investigated in this section were formed via the method detailed in Section 4.2.1 of Chapter 4. The sample was further annealed at a temperature of 200°C for 2 hours. Raman microspectroscopy was performed to confirm the presence of Si-XIII within the transformed region. Fig. A.1 presents a Raman spectrum collected from the indented region. There are three peaks within the 450 - 550 cm^{-1} range; a hd-Si peak at ~515 cm^{-1}, a peak at ~500 cm^{-1} that may be hd-Si or Si-XIII, and a Si-XIII peak at ~475 cm^{-1}. Further, there are peaks associated with the bc8/r8 mixed structure. The Si-XIII peak is the predominant peak within the Raman spectrum, but it is not the sole phase present.

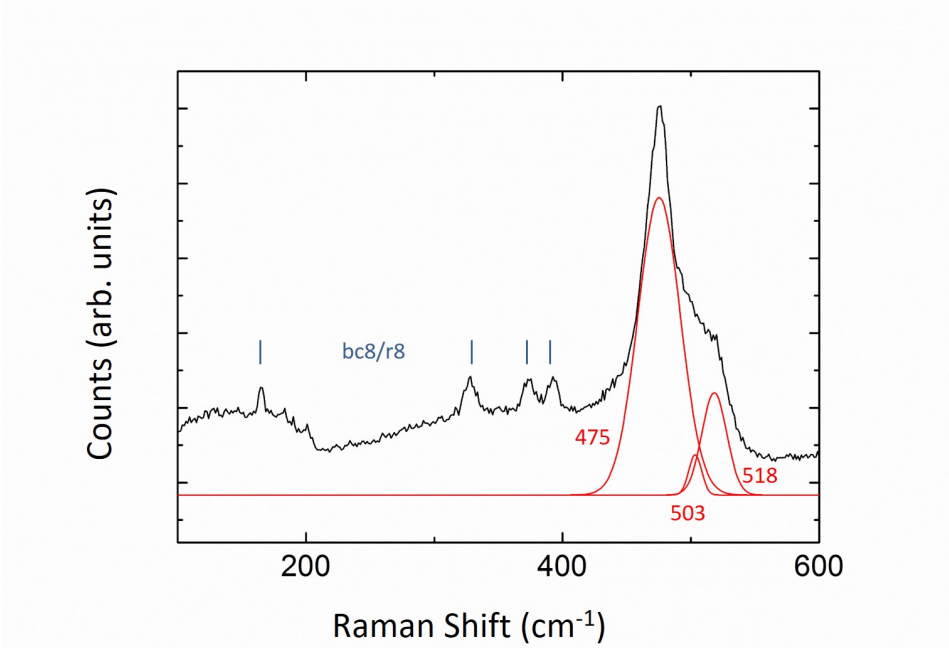

Fig. A.1: Raman spectrum collected from the transformed region after annealing at 200° for 2 hours. The fitted peaks under the large asymmetrical peak at ~475 cm^{-1} have been labelled and indicate the presence of hd-Si and Si-XIII. Peaks associated with the bc8/r8 structure also remain within the spectrum.

XRD measurements on this sample were performed at the 16-ID-B beamline at HP-CAT within the Advanced Photon Source (APS). The incident X-ray beam had an energy of 24.5 keV and a spot size of ~5 μm in diameter. The software package Dioptas [147] was used to integrate the resulting XRD image. The contribution from hd-Si was fitted using the software package GSAS [148].

A.3 Results and Discussion

Fig. A.2(a) shows the XRD data taken from the sample containing Si-XIII. The blurred reflections connected via diagonal lines originate from the underlying dc-Si whereas the rings originate from the poly-crystalline transformed region. It is interesting to note that the rings are circular. This suggests that the stress that resulted in cell elongation in the indentation axis in the bc8/r8 mixed structure is no longer present. It is proposed that this stress is released by the transformation process from r8-Si to Si-XIII. Figure A.2(b) shows the same image after masking. The empty region between detectors and the beam stop have been masked. Further, particularly bright spots which may interfere with the relative intensities between the reflections have also been masked. Finally, reflections associated with the underlying dc-Si that fall within the region of interest (as indicated by the dotted line) are also masked. As the a-Si is less prominent within these images, the a-Si within the image was removed using Dioptas's background subtraction function. Note that this differs from the method used previously where a background image was subtracted.

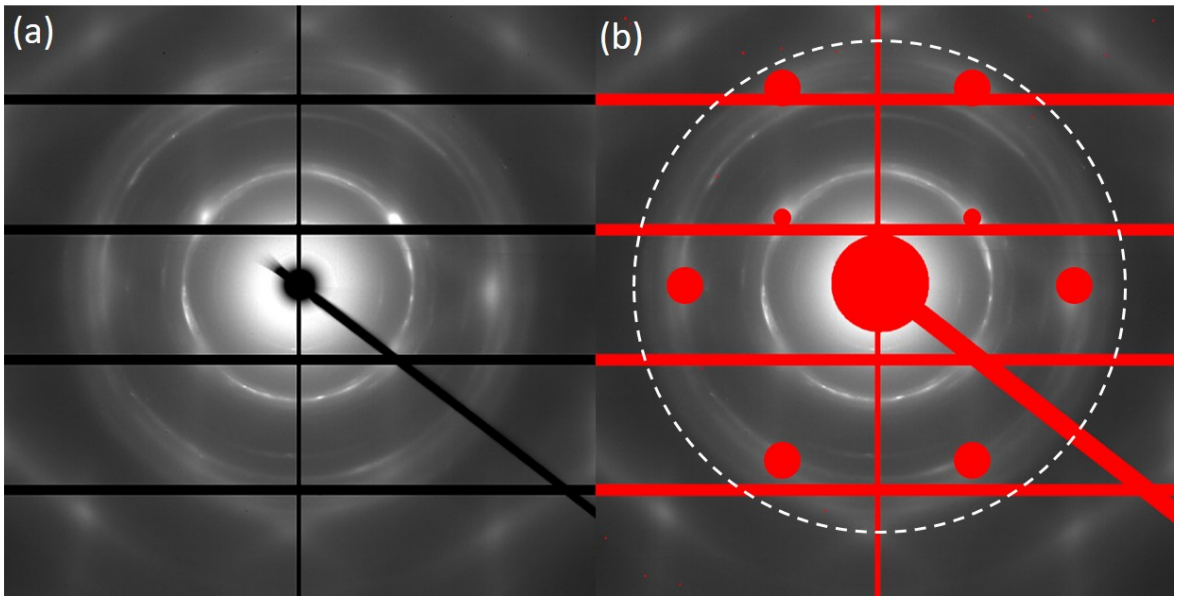

Fig. A.2: (a) XRD image collected from the transformed region and (b) the same image after masking of the region of interest (indicated by the dotted circle).

Fig. A.3 shows the integrated XRD profile. First, to account for the contribution from hd-Si, a Rietveld refinement of the profile using only hd-Si was performed. This refinement and the difference between the calculated and observed profile are also presented in Fig. A.3. It appears that several prominent peaks in the XRD profile can be associated with hd-Si. Firstly, there is a large, asymmetric peak at ~3.1 Å which appears to be a combination of several distinct reflections. The strongest reflection at 3.13 Å belongs to the [002] reflection of

hd-Si. The [100] and [101] hd-Si reflection are also present at 3.28 Å and 2.90 Å. These account for the asymmetry of the large peak at ∼3.1 Å, but the figure clearly shows that hd-Si does not account for all peaks within this d-spacing range. Closer inspection of the XRD image confirms there are 4 distinct lines within this d-spacing range. Thus, there is a reflection at ∼2.95 that is not due to hd-Si. Further inspection of the hd-Si refinement suggests that the three peaks in the 1.5 - 1.9 Å range arise from hd-Si. The observation of only 3 distinct lines within this region in the XRD image suggests that the difference between the calculated and observed profile within this region is not due to peaks from other phases. Finally, a hd-Si peak is calculated but not observed for the [102] plane at 2.27 Å. Previous studies have noted that no significant experimental signal has been observed in XRD for this peak [45]. Thus, the absence of this peak in this data set is not an issue. Interestingly, this result suggests that hd-Si is the predominant phase within the transformed region after annealing at 200°C for 2 hours. This is despite the observation of a far more dominant Si-XIII peak within the Raman spectrum. This suggests that hd-Si has a smaller Raman-active cross-section.

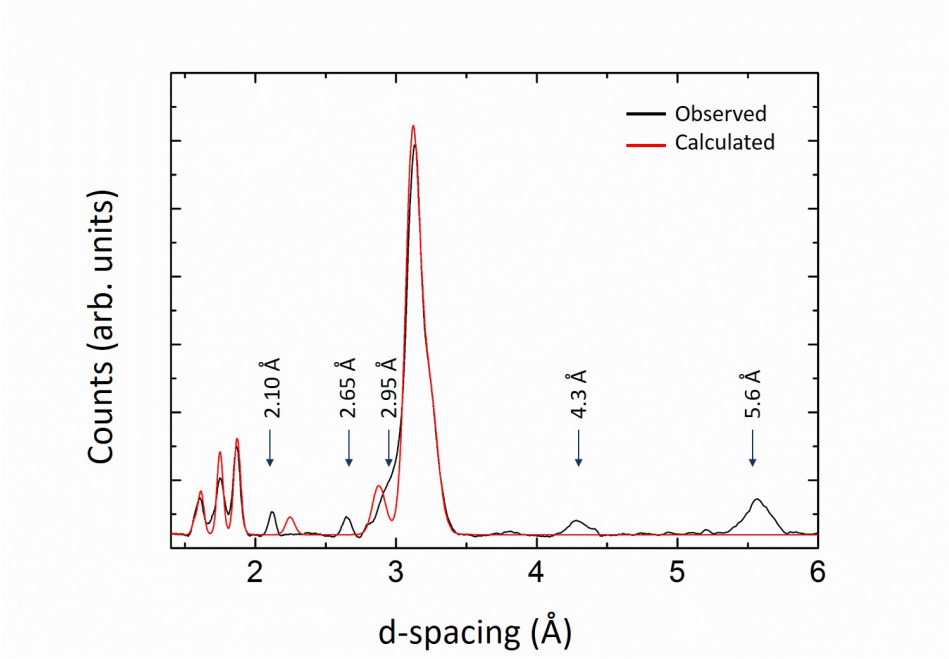

Fig. A.3: Rietveld refinement of hd-Si for the integrated XRD profile. The peaks within the profile that are not associated with hd-Si are indicated.

Within the presented XRD profile, five d-spacing values can be determined that do not originate from hd-Si. These are listed in Table A.2 alongside the Si-XIII reflections observed experimentally using SADP, the most prominent calculated reflections from the predicted $P4_12_12$ phase, and the most prominent reflections of the bc8/r8 mixed structure. The 2.65 Å d-spacing may possibly be attributed to the bc8/r8 structure that was confirmed (via Ra-

This work	SADP	$P4_12_12$	bc8/r8
5.6 Å	5.6 Å		
	4.8 Å		
4.3 Å	4.4 Å		
		3.96 Å	
		3.57 Å	
		3.10 Å	
2.95 Å		2.93 Å	
2.65 Å			2.7 Å
2.10 Å			
			1.8 Å

Table A.2: The d-spacing values determined in this section, reported from an SADP study in Ref. [45], predicted for the $P4_12_12$ phase in Ref. [23], and reported for the bc8/r8 mixed structure in Chapter 4

man) to remain after annealing. Thus, there are four d-spacings that can be attributed to Si-XIII. There is good agreement with two of the three reported d-spacings from experimental SADPs. Previous studies have also reported the absence of expected reflections within XRD images [45]. It is proposed that no reflections are observed at 4.8 Å in the current XRD data in a similar manner. Regarding the predicted $P4_12_12$ phase, many of the prominent reflections were not observed experimentally. This suggests that, while this phase may be energetically plausible, it is unlikely to be Si-XIII.

It should be noted that six reflections are required for peak indexing using structure determination software such as free object for crystallography (FOX). Thus, no further analysis of the crystal structure of Si-XIII could be performed.

A.4 Summary

In this section, a transformed region containing Si-XIII has been probed using XRD. Four d-spacing values were determined for Si-XIII. These values were in agreement with those reported in SADP experimental studies. However, there was minimal agreement with the $P4_12_12$ phase that was predicted to be a plausible candidate for Si-XIII.

Although the Raman spectrum was dominated by a peak associated with Si-XIII, XRD suggested that hd-Si was the predominant phase. It would be of interest in future studies to

explore different annealing conditions that may result in transformed region where Si-XIII is the predominant phase. If such regions could be formed, more peaks associated with Si-XIII may be determined from XRD and structural analysis of this phase may then be forthcoming.